Exploration of Catalysts and Catalysis under Near Working Conditions

Thesis Submitted to

Academy of Scientific and Innovative Research

For the Award of the Degree of

DOCTOR OF PHILOSOPHY

In

CHEMICAL SCIENCES

By

K. Prabhakar Reddy

(AcSIR Registration Number**:** 10CC14J26004)

Under the Guidance of

Dr. Chinnakonda. S. Gopinath

Catalysis and Inorganic Chemistry Division

CSIR-National Chemical Laboratory
Pune, India.

December 2018

CERTIFICATE

This is to certify that the work incorporated in this Ph.D. thesis entitled **"Exploration of Catalysts and Catalysis under Near Working Conditions"** submitted by **Mr. K. Prabhakar Reddy** to the Academy of Scientific and Innovative Research (**AcSIR**) in fulfilment of the requirements for the award of the Degree of **Doctor of Philosophy**, embodies original research work under my supervision. I further certify that this work has not been submitted to any other University or Institution in part or full for the award of any degree or diploma. Research material obtained from other sources has been duly acknowledged in the thesis. Any text, illustration, table etc., used in the thesis from other sources, have been duly cited and acknowledged.

K. Prabhakar Reddy
Date: 26-12-2018

Dr. Chinnakonda S. Gopinath
(Research Supervisor)
Chief Scientist and Chairman
Catalysis and Inorganic Chemistry Division
CSIR-NCL, Pune

Declaration

I hereby declare that the original research work embodied in this thesis entitled, **"Exploration of catalysts and catalysis under near working conditions"** submitted to the Academy of Scientific and Innovative Research (AcSIR) for the award of degree of Doctor of Philosophy (Ph.D.) is the outcome of experimental investigations carried out by me under the supervision of **Dr. Chinnakonda S. Gopinath**, Chief Scientist, Catalysis and Inorganic Chemistry Division, CSIR-National Chemical Laboratory, Pune. I affirm that the work incorporated is original and has not been submitted to any other academy, university or institute for the award of any degree or diploma.

K. Reddy.

Date: 26-12-2018

Place: Pune.

Mr. K. Prabhakar Reddy
Catalysis and inorganic chemistry division
CSIR-National Chemical Laboratory, Pune.

Dedicated to my parents

Acknowledgements

It is my great pleasure to acknowledge my teacher and research supervisor, Dr. C. S. Gopinath for his motivation, guidance, freedom, support and constructive criticism throughout my Ph.D work. I really admired the way he handle the situations with his cool attitude.

My Sincere thanks to my doctoral advisory committee members: Dr. Ashish Lele, Dr. Chetan Gadgil, Dr. T. Raja, Dr. A. T. Biju, Dr. S. P. Mukherjee for their helpful input and thought-provoking discussions.

I express my heartfelt thanks to the present and past heads of the catalysis and Inorganic chemistry division, Dr. C. S. Gopinath and Dr. D. Srinivas, Dr. A. P. Singh for providing me all the divisional facilities required for my research work. I would also like to thank all the scientific, technical and administrative staffs in the division for their direct and indirect help in various occasions.

I am grateful to UGC, for awarding the research fellowship and Prof. A. K. Nangia, Director, and Dr. S. Pal, Former Director, CSIR- National Chemical Laboratory for providing me the infrastructure and advanced research facilities, and to submit this works in the form of a thesis for the PhD degree. I am also thankful to the Academy of Scientific and Innovative Research (AcSIR) for giving me a chance to reach one of the major milestones in my life.

I would like to offer my sincere admiration to Dr. T. Raja, Dr. C. P. Vinod, Dr. Dinesh Jagadisan and Dr. Ekambaram Balaraman for their enthusiastic encouragement and support.

I’m grateful to Dr. C. V. V. Satyanarayana and Dr. Srikanth Dama for allowing and helping me to carry out some of my experiments in their lab. I am thankful to Prevac, Poland for their timely technical help and suggestions.

I wish to thank my all my friendly lab-mates, Drs. Edwin S. Gnanakumar, Sivaranjani, Kanak Roy, Naresh N, Ashwin, Rajaambal, Sanjay Negi, Sadhu Kolekar, Devaraji, Anjani Dubey, Kshirodra Patra, Pradnya Bharad, Ruchi Jain, Mr. Manoj, Kavya, Nitin, Bela, Madhu, Ravi, Himanshu, Indra, Kranti, Sreeyaraj for creating a cheerful and

enjoyable working atmosphere in the lab. They were extremely supportive as well as helpful during my tenure.

I would like to acknowledge my seniors Dr. Anjani Dubey and Dr. Ruchi, who taught me the MBI and NAPPES system handling and operation.

I would like to express thanks to Ashok, Sunil, Sridhala, Vyshakh, Aswathy, Periz, Manikandan, Prabhu. K, Prabhu. M, Sharad, Yogita, Pranjal, Preeti, Shiva, Govind, Mahesh, Samanta for the association in an extended group.

Seniors are always great and roll model in my life. I had wonderful seniors during my college days as well as in research life. My deepest thanks to my seniors Nookaraju M, Santhosh Biradar, Surender Tonda, Janani Kumar Reddy, Madanachary, Sadhu Kolekar, Naresh Nalajala, Sreekuttan, Venkat Reddy, Ramu Vadde, Narendra Prasad, Upender Reddy, Narasimha Kanna, Laxmi Prasad, Srikanth Dama, Rami Reddy, Chaithanya, Devadutta, Viswanath, Pradeep Singh, Naresh Bhuma. I would like to thank my NCL friends Sagar, Swamy, Srikanth, Pravin, Anand, Naleeni, Naresh killi, Kumar Raja, Srikanth Koregaonker, Pranjal, Anil H. A, Sharad, Dheeraj, Mohitosh, Arun, Sourya and Dhananjay. A special thanks to my friends & roommates Gopi, Surender, Eshvender, Abhinay, Saikrishna, Vinay, Venkatesh, Harsha, Rizwan, Dheeraj and Sandeep; who were always with me throughout my journey.

I would also like to thank all my high school and college friends, who are with me along the way: Santhosh, Kumar, Gopi Krishna, Srinivas Reddy, Raju, Shekar, Shiva Krishna, Rambabu, Narsimha, Naresh, Dinesh, Suresh and Linga Raju.

Last but not least, my deepest acknowledgement goes to Amma, Nanna, Annaya and all my relatives, friends for their love, support and encouragements throughout my life.

K. PRABHAKAR REDDY

Contents

List of Abbreviations

UHV	Ultra-High Vacuum
RGA	Residual Gas Analyzer
PES	Photoelectron Spectroscopy
NAPPES	Near-Ambient Pressure Photoelectron Spectroscopy
NEXAFS	Near Edge X-ray Absorption Fine Structure
NAP-XPS	Near-Ambient Pressure X-ray Photoelectron Spectroscopy
NAP-UPS	Near-Ambient Pressure Ultraviolet Photoelectron Spectroscopy
STM	Scanning Tunnelling Microscopy
HPSTM	High Pressure Scanning Tunnelling Microscopy
TPD	Temperature Programmed Desorption
BE	Binding Energy
KE	Kinetic Energy
UV	Ultra-Violet
MBI	Molecular Beam Instrument
QMS	Quadrupole Mass Spectrometer
VB	Valence Band
RT	Room Temperature
ELR	Electrostatic Lens Regime
EEA	Electron Energy Analyzer
FWHM	Full Width Half Maximum
IMFP	Inelastic Mean Free Path
XRD	X-ray diffraction
TPD	Temperature Programmed Desorption
TPR	Temperature Programmed Reduction
SEM	Scanning Electron Microscopy
IMFP	Inelastic Mean Free Path

List of Symbols

Θ_o	Oxygen Coverage
ϕ	Work Function
h	Plank Constant
E_F	Fermi Level
υ	Frequency
E_F	Fermi Energy
σ	Photo ionization Cross Section

List of Figures

Preface

In the thesis entitled on “Exploration of catalysts and catalysis under near working conditions” focuses on the electronic structural changes of metal to metal oxides/metal carbides on polycrystalline foils under near ambient pressure and elevated temperatures conditions was explored by Near ambient pressure photoelectron spectroscopy (NAPPES). The current thesis comprises of six chapters, out of which the first is the introductory chapter; second chapter describes the experimental techniques employed and the last chapter summarizes the work and provides a future outlook. About a decade ago, it was not possible to explore the catalysts under catalysis conditions or close to that in a typical photoelectron spectrometer, since the technique was not available. However, this is an essential technique to understand the direct surface changes that occur under working or near-working conditions of catalysts. Indeed, this bridges the large pressure gap that exists between ideal high vacuum measurements employed in surface science and the real-world catalysis conditions that occur at ambient or high pressures. Oxidation and reduction are the two important classes of reactions in catalysis and how the catalyst interacts under these conditions is a pre-requisite to understand the ensuing catalysis. Further, how the phase formation occurs is very relevant from material as well as catalysis point of view. All three working chapters address these issues.

Chapter 1. In the surface science approach towards the catalysis is discussed, especially measuring surface changes under the catalysis conditions or close to that. Among those surface techniques, complete details on photoelectron spectroscopy and its advancement towards bridging the pressure gap is to be discussed. A molecular-level understanding of catalysis on the catalyst surface can be studied by using surface science. From the past four decades, surface science gave the vast knowledge in the interaction of the gas molecules with single crystal surfaces at ultrahigh vacuum conditions. However, it was questioned often on to what extent the information obtained in UHV conditions can be extrapolated to real-world catalysis, where reactions take place at high pressures and more often with complex powder catalysts. These apparent gaps between surface science and real-world catalysis have been termed as a pressure gap and the materials gap, and much effort has been put into bridging them. To address these disconnect between the real world catalysis from conventional surface science studies, an attempt has been made to bridge the pressure and material gap by using NAPPES in the current thesis.

Chapter 2. The NAPPES unit is equipped with a VG Scienta-R3000HP electron energy analyzer, and its several advantages will be described. In contrast to the many NAP systems employed with a closed high pressure cell, the system employed for the present studies involves an open reactor design. The polycrystalline foil was sputter cleaned by reported procedures. The helium-I ($h\upsilon$ = 21.2 eV) discharge lamp was used to record the valence band at a pass energy of 5 eV. Core level and x-ray VB spectra were also recorded using a monochromatic Al Kα radiation source ($h\nu$ = 1486.6 eV). A complete detail about NAPPES is explained in this chapter. CASA software was used for data analysis. Various analytical techniques employed were described for the basic principle along with the description of the instrument.

Chapter 3. In this chapter valence band (VB) and core level, photoelectron spectroscopy was carried out to investigate the electronic structural changes from polycrystalline Co to spinel Co_3O_4, via CoO at near ambient pressures (NAP; 0.1 mbar). O_2-Co and H_2-CoO_x gas−solid oxidative and reductive interactions, respectively, have been explored with UV photons (He-I) or low kinetic energy electrons (≤16 eV) under NAP conditions. Typical VB features of Co metal; CoO, Co_3O_4, and a mixed phase between any two adjacent features were observed and well corroborated with core level changes. Very significant and characteristic changes were observed with Co 3d features in the VB for each stage from Co oxidation to Co_3O_4 as well as Co_3O_4 reduction to CoO. Co_3O_4 and CoO can be reversibly obtained by alternating the conditions between 0.1 mbar of H_2 at 650 K and 0.1 mbar of O_2 at 400 K, respectively. A meaningful correlation is observed between the changes in work function (ϕ) with cation oxidation state; small changes in the stoichiometry can strongly influence the shift in Fermi level. Reversible ϕ changes are observed between oxidation and reduction conditions. While the O 2p derived feature for CoOx was observed at a constant BE (~5 eV) throughout the redox conditions, the Co 3d band and molecular oxygen or hydrogen vibration feature shifts significantly underscoring the physicochemical changes, such as charge transfer energy and hence changes in satellite intensity. The peak close to E_F originated from the $3d^6\underline{L}$ final state of the octahedral Co^{3+} 3d band of Co_3O_4. A meaningful correlation is observed between the changes in ϕ with cation oxidation state; small changes in the stoichiometry can strongly influence the shift in Fermi level and changes in ϕ under NAP conditions. It is to be noted that ϕ changes alters the valence band edge energy and directly affects the reaction. Reversible ϕ changes are observed between oxidation and reduction conditions. While the O 2p derived feature for CoOx was observed at a constant BE (~5 eV) throughout the redox

conditions, the Co 3d band and molecular oxygen or hydrogen vibration feature shifts significantly underscoring the physicochemical changes, such as charge transfer energy and hence changes in satellite intensity. The peak close to E_F originated from the $3d^6\underline{L}$ final state of the octahedral Co^{3+} 3d band of Co_3O_4.

Chapter 4. Tuning the surface energetics, especially ϕ of the materials is a great deal of interest for the wide range of surface and interface based devices and applications. How the ϕ of a solid surface change under the reaction conditions is of paramount interest to the chemists, particularly to the areas of surface dependent phenomena such as catalysis, electrochemistry. In the present study, by using valence band and core level photoelectron spectroscopy, surface electronic changes from Mo to MoO_3 via MoO_2 was studied under relevant near ambient pressure and high temperature conditions. Very significant change in the ϕ from Mo to MoO_3 was observed and it is well corrborated with the changes in gas-phase vibrational features of O_2 in both NAPUPS as well in NAPXPS. Reversible changes in electronic structure are observed when MoO_3 was reduced in H_2 to MoO_2. Based on the extent of oxidation/reduction of MoO_x, NAPUPS has shown, one or two additional peaks in the band gap at 0.6 and 1.6 eV below the Fermi level. Mo^{5+} features are identified in the VB and in the Mo 3d core levels with distinct features. Mo^{5+} features are also stable and essential to bridge MoO_2 and MoO_3 layers, and their co-existence. In addition, characteristic changes in Mo 4d and O 2p features observed from Mo to MoO_3 and well correlated to the band gap of MoO_3. Oxidation and reduction propagate from the surface to bulk; indeed this has significant implications in surface dependent phenomena. The present study demonstrates (a) the uniqueness of NAPUPS in identifying the subtle to large changes in the electronic structure on solid surfaces under common oxidation and reduction (in general, under reaction) conditions, and (b) relevance of NAPUPS to all surface dependent phenomena, such as catalysis, electrochemistry.

Chapter 5. The materials gap can be partly bridged by refining the model systems and, e.g., powder metal carbides, polycrystalline foil. One example of such a model system for a hydrogenation catalyst is given in this chapter. Here we studied the hydrogenation of CO_2 using hydrogen as reducing agent via reverse water gas shift reaction by using an active, selective and low-cost Mo_2C catalyst. From this study, we found that Mo_2C catalyst, with ratio 1:3 of CO_2: H_2, is highly active (58 %) and selective (62 %) towards carbon monoxide at 750 K and 1 atm pressure. XRD and Raman analysis have shown the synthesized samples

are in the β-Mo_2C form and even after the reaction as well. Further, we extended the RWGS reaction by In-situ XPS with model Mo_2C foil as a catalyst to understand the mechanistic aspects of this reaction at near ambient pressure (0.1 mbar) and various temperature. Throughout the reaction, no significant changes in the Mo 3d indicate the catalyst is highly stable, however from C and O 1s spectrum we could able to find the oxycarbide species as an active intermediate. **Chapter 6.** This chapter summarizes the overall outcome and future outlook of the research work carried out in the present thesis.

List of Publications (From Ph.D Thesis)

1. **Reddy**, **K. P.**; Mhamane, N. B.; Ghosalya, M. K.; Gopinath, C. S., Mapping Valence Band and Interface Electronic Structure Changes during Oxidation of Mo to MoO_3 via MoO_2 and MoO_3 Reduction to MoO_2: A NAPPES Study. *J. Phys. Chem. C.* **2018**, *122*, 23034-23044.
2. **Reddy**, **K. P.**; Jain, R.; Ghosalya, M. K.; Gopinath, C. S., Metallic Cobalt to Spinel Co_3O_4-Electronic Structure Evolution by Near-Ambient Pressure Photoelectron Spectroscopy. *J. Phys. Chem. C.* **2017**, *121*, 21472-21481.
3. **Reddy**, **K. P**.; Dama, S.; Mhamane, N. B.; Ghosalya, M. K.; Chilukuri, S.; Gopinath, C. S., Molybdenum Carbide Catalyst for the Reduction of CO_2 to CO: Surface Science Aspects by NAPPES and Catalysis Studies. (Manuscript Submitted.).

List of Publications (From Collaborations)

4. Ghosalya, M. K.; **Reddy**, **K. P.**; Jain, R.; Roy, K.; Gopinath, C. S., Subtle Interaction between Ag and O_2: a Near Ambient Pressure UV Photoelectron Spectroscopy (NAP-UPS) Investigations. *J. Chem. Sci*. **2018**, *130*, 30.
5. Dubey, A.; **Reddy, K. P.**; Gopinath, C. S., Ambient CO Oxidation on In-Situ Generated Co_3O_4 Spinel Surfaces with Random Morphology. *ChemistrySelect*. **2017**, *2*, 533-536.
6. Ghosalya, M. K.; Jain, R.; **Reddy**, **K. P.**; Gopinath, C. S., Silicon Oxidation by NAPPES: From Dangling Bonds to Oxygen Islands to 2D SiOx Layer to the Onset of Bulk SiO_2 Formation. *J. Phys. Chem. C.* **2018**, *122*, 4331-4338.
7. Jain, R.; **Reddy**, **K. P.**; Ghosalya, M. K.; Gopinath, C. S., Water Mediated Deactivation of Co_3O_4 Nanorods Catalyst for CO Oxidation and Resumption of Activity at and Above 373 K: Electronic Structural Aspects by NAPPES. *J. Phys. Chem. C.* **2017,** *121*, 20296-20305.
8. Roy, K.; Jain, R.; Ghosalya, M. K.; **Reddy, K. P.**; Gopinath, C. S., Three-way Catalytic Converter Reactions Aspects at Near Ambient Temperatures on Modified Pd-Surfaces. *Comptus Rendus Chimie*. **2016**, *19*, 1363-1369.
9. Burange, A. S.; **Reddy**, **K. P.**; Gopinath, C. S.; Shukla, R.; Tyagi, A. K., Role of Palladium Crystallite Size on CO Oxidation Over $CeZrO_{4-\delta}$ Supported Pd Catalysts. *J. Mol. Catal*. **2018**, *455*, 1-5.
10. Chauhan, M.; **Reddy, K. P.**; Gopinath, C. S.; Deka, S., Copper Cobalt Sulfide Nanosheets Realizing a Promising Electrocatalytic Oxygen Evolution Reaction. *ACS Catal.* **2017**, *7*, 5871-5879.

11. Mohan, M.; Nandal, V.; Paramadam, S.; **Reddy**, **K. P.**; Kumar, R. S.; Agarwal, S.; Gopinath, C. S.; Nair, P. R.; Namboothiry, M. A. G., Efficient Organic Photovoltaics with Improved Charge Extraction and High Short-Circuit Current. *J. Phys. Chem. C.* **2017**, *121*, 5523-5530.
12. Sorathiya, K.; Mishra, B.; Kalarikkal, A.; **Reddy**, K. P.; Gopinath, C. S.; Khushalani, D.; Enhancement in Rate of Photocatalysis Upon Catalyst Recycling. *Sci. Rep.* **2016**, *6*, 35075.

Chapter-1

Introduction to Surface Science-based approach to Heterogeneous Catalysis

1.1 Catalysis

Catalyst is a substance, which affects the rate of a chemical reaction, generally by lowering the activation energy and without being a part of its end products; this process is known as catalysis. In 1836, Berzelius introduced the concept of catalysis. Based on the phases of catalyst to reactants, catalysis can be classified into two types, namely homogeneous and heterogeneous catalysis. In homogeneous catalysis, both reactant(s) and catalyst are in the same phase. In contrast to homogeneous catalysis, phases of both reactants and catalyst are different in heterogeneous catalysis. Although, homogeneous catalysts have better activity and selectivity than heterogeneous catalysis, separation of homogeneous catalyst from the (unreacted) reactants and products mixture makes economically expensive and hence not preferred by industries. As solid surfaces have unsaturated coordination sites and allows adsorption of gas/liquid phase reactants easy on it. Porosity of solid catalysts allow the diffusion of reactants to the active sites and finally chemical transformation of reactants to products occurs. All the heterogeneous catalysis happens on the surfaces/interfaces of the solid catalysts. Due to positive free energy of solids surface, reactants can diffuse to active sites to keep surface tension at low value. On other hand, the surface atom coordination number of solid always tries to have same as that of the bulk atoms; hence it can attract the reactants molecules from the immediate surroundings.

Based on the strength of the bond between the surface (adsorbent) and reactants (adsorbate), adsorption process is classified into two types; first one is physisorption with weak van der Waals forces, and it can desorbs as such from the surface by simple heating. The Second is the chemisorption (a chemical bond); reactant or adsorbate molecule may be dissociated and react with other adsorbate species leading to products desorption at appropriate temperatures. Industrial catalysis started in 1875 with production of sulphuric acid with Pt catalyst. In succeeding years NH_3 oxidation to nitric acid on Pt gauge was developed by Ostwald. However major breakthrough in industrial catalysis happened in 1914 with the production of ammonia from the elements, namely, N_2 and H_2, using iron-based catalyst at high pressure and temperature process. This process is known as Haber process and research associated with ammonia alone won three Nobel prizes, for ammonia making, industrial process of ammonia production and mechanism of ammonia formation. In subsequent years, Fischer-tropsch synthesis, development of catalytic cracking process for oil refining, reforming reaction, Ziegler Natta catalyst and three way catalytic converters were

the major breakthroughs in the chemical industry. Indeed, all these processes made the modern-day life possible. However, too much exploitation of natural resources, fossil fuels and large industrialization around the globe led to pollution in many fronts. Heterogeneous catalysis is expected to play a main role in solving the environmental problems with improved or new catalysts. In the present scenario, nearly 90% of chemical reactions in industries involve catalysis. An ideal catalyst should be chemically inert, high surface area, specific in activity, sustainable for years together and economically viable.

Importance of catalyst for a simple gas phase reaction is shown in Figure. 1.1 with an energy diagram. A reaction with catalytic pathway has low activation energy than non-catalysed pathway.

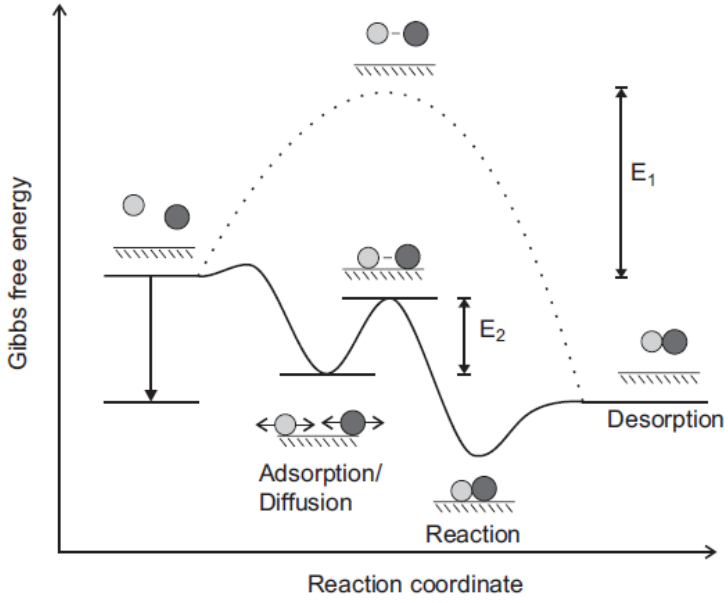

Figure 1.1: Illustration of the role of a heterogeneous catalyst with an energy diagram. E_1 and E_2 are the activation energy for gas phase reaction without and with catalyst respectively.

Rate of the reaction for a heterogeneous catalysed reaction is represented as,

$$A + B \xrightarrow{Catalyst} AB \qquad \text{(Eq. 1.1)}$$

$$Rate = k[A][B] \qquad \text{(Eq. 1.2)}$$

The dotted trace shows the reaction pathway without a catalyst; whereas solid line shows the surface catalyzed pathway for the same reaction. Reactants A and B shows adsorption on the surface followed by diffusing to active sites followed by reaction and finally product

desorption occurs. Net change in the Gibbs free energy for the reaction is same in both the cases; however activation energies (E_a) are different. Rate constant k can be described by Arrhenius equation.

$$k = Ae^{-Ea/RT} \qquad \text{(Eq. 1.3)}$$

Since activation energy (E_a) exponential to the rate constant k, small decrease in the activation energy can increase the rate of reaction significantly.

Although, rate equation itself can give some macroscopic information about the mechanism of chemical reaction, it ignores the microscopic surface phenomena like adsorption, diffusion and desorption process. It is to be noted that ammonia production catalyst was discovered by simple hit-and-trial approach by screening few thousand catalysts. For this reason, heterogeneous catalysis was traditionally considered as black-box magic. Nonetheless, surface science analysis provides microscopic details which occur on the surface of catalysis and it is essential for the design of the active and selective catalyst for the particular reaction. A better understanding of the microscopic details allows us to design more active and selective catalyst.

In addition to that employing various surface science techniques to address the dynamic processes that occur on the catalyst surface during the actual reaction conditions gives most of the above mentioned fundamental information. This approach may be employed in the rational design of the improved catalysts and this approach is known as surface science-based approach in heterogeneous catalysis.

1.2. Surface science approach towards heterogeneous catalysis

To meet the rapidly growing population and global energy demands, conventional trial and error approach to design catalysts is no longer been able to satisfy the demands of industries. In contrast to that understanding the surface properties of various catalysts plays a vital role in improving the efficiency of a catalytic reaction. Such a trend was started after commercial availability of high vacuum and ultra high vacuum (UHV~10^{-9} Torr) instruments from in 1970 and this led to development of surface science, in which atomic-scale catalyst investigations are made possible through surface science techniques.[1] This technique reveals the physical and chemical process that occurs at the interface of two phases, under conditions which are well controlled. The catalytic activity of surfaces is controlled by many parameters such as adsorption capacity, bonding strength of reactants, reaction intermediates, co-

adsorbates, impurities (if any), surface structure/morphology and products desorption etc. Understanding of these different aspects gives a huge impact on the reactivity of a catalyst surface for a particular reaction. Surface science research is motivated by the need to determine the chemical composition of the surface, its structure and morphology, its electronic structure and the molecular identity of the species that may be present on the surface and their influence on the catalytic reaction. These surface science experiments performed at UHV and on well defined single crystal surfaces.[2] Generally UHV condition is essential to maintain an atomically clean single crystal surface to study the adsorption/diffusion/desorption kinetics of the reaction using photon/electron/Ions based experiments. In addition, it can minimize the scattering of gas phase probe molecules with photons/electron/ions. In contrast to the real-world industrial powder catalysts, well defined single crystal surfaces helps in the understanding of the fundamental catalysis reaction and its reaction mechanism and the nature of the adsorbed species, etc under UHV conditions.[3] These information are crucial to understand the basic catalysis aspects. However, real-world catalyst contains many different components (such as support, promoters), mainly towards improving the catalytic activity and each component have a definite role. Although it is very difficult to address all aspects of real-world catalyst through surface science, efforts are continuously being made towards that. For example, metal particles supported on thin film supports are being evaluated for catalysis reactions to bridge the gap.[4] Similarly, thin film form of powder catalyst is being explored for complex reactions, such as methane activation, by surface science approach.[5]

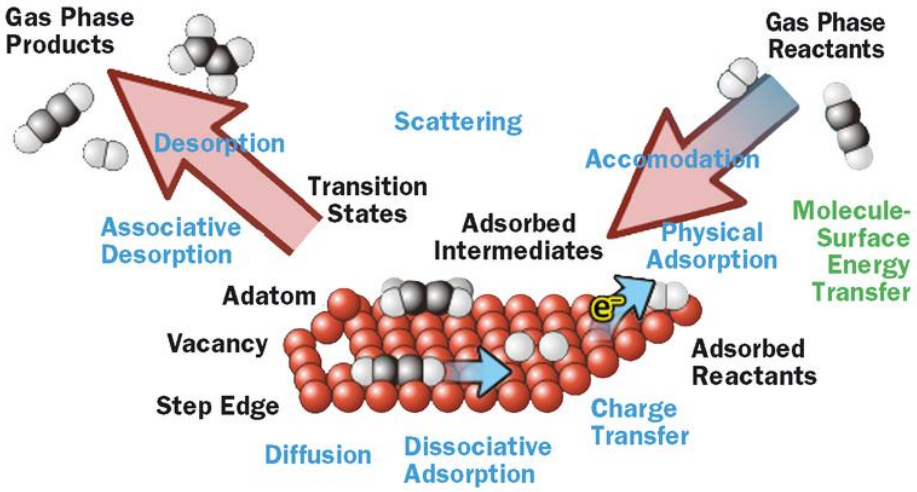

Figure 1.2: Various surface chemical phenomena during a heterogeneous catalytic reaction. From Ref 6; Copyright permission obtained from PSI.[6]

There are several surface science techniques to probe the top most layers of the surface/interfaces exposed to vacuum. These includes Low energy electron diffraction (LEED), Electron energy loss spectroscopy (EELS), X-ray photoelectron spectroscopy (XPS), Auger electron spectroscopy (AES), Thermal desorption spectroscopy (TPD), Ion scattering spectroscopy (ISS), Atomic force microscopy (AFM), Scanning tunnelling microscopy (STM), surface x-ray diffraction (SXRD) and Secondary ion mass spectroscopy (SIMS) etc.[7] Many of these techniques works under UHV conditions, since it depends on the detection of the ion or electron emitted from the surface. Optical techniques like polarised modulation Infra red reflection absorption spectroscopy (PM-IRRAS), Sum frequency generation (SFG) can be used to study interfaces like solid-vacuum, solid-gas and solid-liquid.[8] Annaland et al. studied the adsorption of CO_2 and water on hydrotalcite by using FTIR and observed that bidentate carbonate formed after adsorption of CO_2. Additionally, co-adsorption of water breaks strong bidentate carbonate.[9] The electronic structure of surfaces can be studied with AES and photoelectron spectroscopy. AFM, LEED and SXRD can be used to probe the surface structure as well as molecules adsorbed on it. Invention of scanning tunnelling microscopy by Binnig and Rohrer in 1981 and its later developments transformed surface chemistry into a truly atomic-level scale science.[10] For example, by monitoring an individual adsorbate in motion, the surface diffusion rate of a single molecule or a cluster can be obtained based on statistics of molecular events.[11] By in-situ imaging of the evolution of co-adsorbed surface intermediates under reaction conditions, the active sites for many catalytic processes were unveiled. Surface coverage (Θ), sticking coefficient (s), oxygen storage capacity (Θ_{osc}) of reactants and kinetics of the reaction can be possible to study with Molecular beam Instrument (MBI).[12] Dubey et al. calculated the oxygen storage capacity in $Ce_{1-x}Zr_xO_2$ thin films with varying ratio of Ce to Zr ratio and temperatures.[5] Traditional surface science techniques were also shown the Rh surface reconstruction by ethylene chemisorptions.[13] Theoretically, density functional theory (DFT) calculation can be used to measure the energy of surface structures, diffusion barriers, reaction barriers and adsorption energies.[14] Along with the experimental data, the d-band model provides answers to fundamental questions such as why bulk gold is noble while small gold clusters are not and why surface defect sites (steps and kinks) are more chemically active.[15] From the past four decades, surface science gave the vast knowledge in the interaction of the gas molecules with single crystal surfaces at UHV conditions using these techniques.

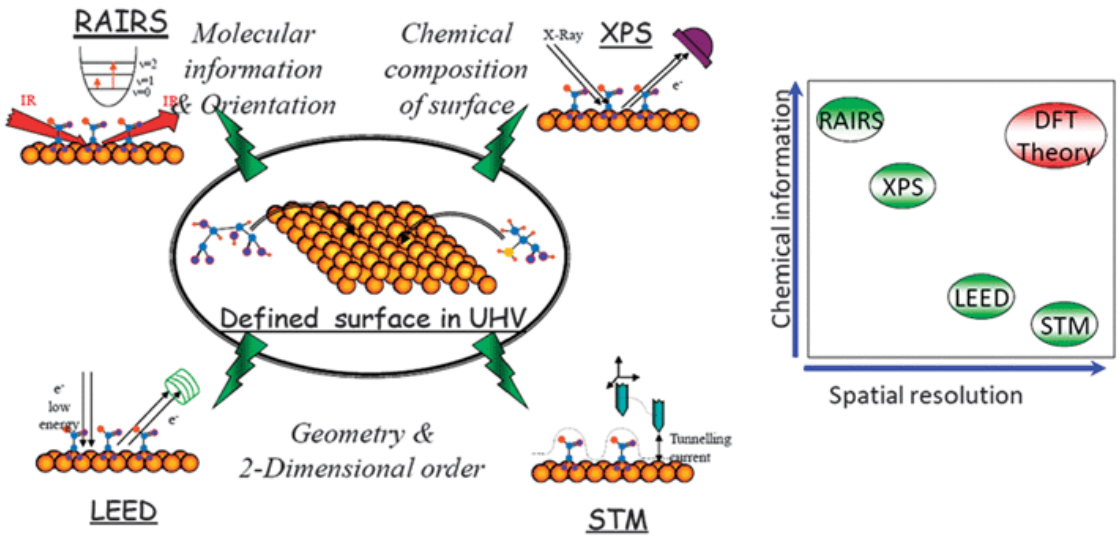

Figure 1.3: Various surface science techniques (Left) shows how the use of complementary surface spectroscopy enables structural details and molecular ordering to be probed. (Right) shows the complementary chemical and spatial information provided by different techniques. Good experiment–theory collaborations have the potential to provide high quality chemical and spatial information from molecular layers at surfaces. From Ref 16; Copyright permission obtained from RSC.[16]

However, the surface science approach towards heterogeneous catalysis was recognized by awarding the Nobel Prize in 2007 to Gerhard Ertl for his studies on fundamental understanding for many chemical reactions including NH_3 synthesis and non-linear kinetics observation for CO oxidation on Pt catalyst. The structural and activity correlations of the Fe crystal faces for NH_3 synthesis compared and suggested that the surface atoms with high coordination number (Fe (111) (C7 and C8) are the active sites for ammonia synthesis.[17] These findings helped in molecular level understanding and improvement of the industrial NH_3 synthesis. More importantly, this example highlighted the essence of surface science approach for extracting complex surface chemical processes in industries, which were previously believed impossible to obtain.[2,18,19]

1.3. Pressure gap and material gap

Many surface processes like adsorption, desorption, reaction of reactants, desorption and surface reconstruction and species involved in the reaction can be detected by conventional surface science techniques. Although conventional UHV techniques provided a vast knowledge in catalysis since last four decades, it is often questioned for its validity. For

example, to what extent the information obtained under UHV conditions for a given defined system can be extrapolated to real-world catalysis. It is to be noted that surface catalytic reactions occur under atmospheric pressure or high pressure and at high temperatures on complex materials catalysts like porous materials/metal supported metal oxides, which complicates the kinetic and mechanistic analysis of heterogeneous catalysis.[20-22] Indeed, few studies in recent times revealed the restructuring on Pt surface occurs under ambient pressures of CO and H_2, where conventional surface techniques cannot gives these information.[23] Muhler et al. investigated the CO oxidation over Rh, Pt and Pd under UHV conditions. In contrast to low CO oxidation activity on Rh surface in UHV conditions over Pt, Pd, in strongly oxidising conditions shown superior activity with Rh.[24] While single crystal surfaces are well defined and it's not like real world powder catalyst, contains metal oxide supported catalyst, porous materials, composites, mixed oxides, alloys or promoters, etc.

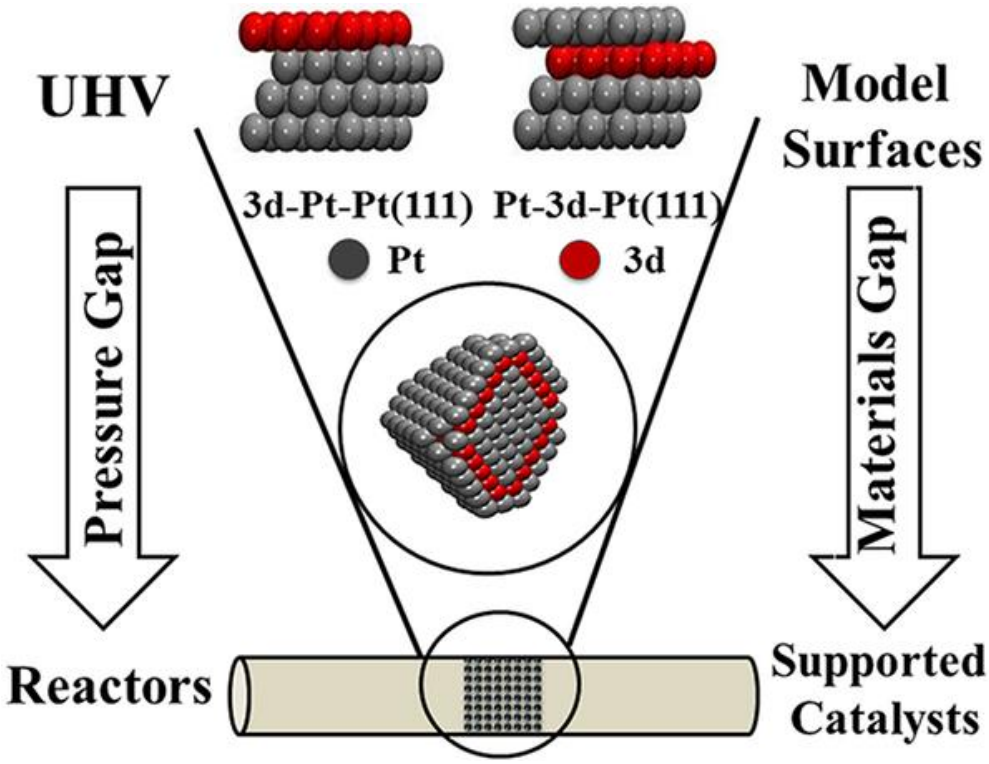

Figure 1.4: Schematic representation of bridging the material and pressure gap. From Ref 25; Copyright permission obtained from ACS.[25]

Moreover, Activity of any catalytic reaction also depends upon the particle morphology, size, metal support interaction, metal dispersion and even type of synthesis method adopted for the reaction. However, activity correlation on well defined surfaces from surface science studies

need not correlate well with real world catalysis. This is the main reason why many researchers attempting to monitor the surface processes under realistic conditions and these apparent gaps between surface science and real-world catalysis conditions have been termed as a pressure gap and the materials gap, and much effort has been put into bridging them. To advance the science and develop applications in these fields, it is important to obtain a detailed knowledge of the atomic scale geometrical and electronic structure of the interfaces as close as possible to real operating conditions in terms of pressure and temperature. For the same, in-situ techniques are required to access the molecular level understanding of gas-solid, gas-liquid interfaces under ambient or atmospheric pressures and required temperature conditions.

1.4. Near ambient pressure photoelectron spectroscopy

Among the surface science techniques, photoelectron spectroscopy is considered to be the powerful tool due to its exclusive exploration of surface layers with the maximum depth of 2-10 nm, and elemental, chemical specific in nature. Indeed, this is the only technique that provides the direct electronic structure aspects of solids. More importantly, we can use it as an in-situ technique known as near ambient pressure photoelectron spectroscopy (NAPPES), due to the advances made in the last fifteen years. It is one of the most versatile surface technique for probing the composition and electronic structure under elevated pressures. Initially, Siegbahn and co-workers from Uppsala University introduced conventional (UHV) x-ray photoelectron spectroscopy, in late sixties and early seventies. Thereafter Siegbahn group developed the near ambient pressure photoelectron spectroscopy and studied the vapour-liquid interfaces.[26] In subsequent years, Joyner and Roberts, from Cardiff University, UK recorded the solid-gas interfaces by further developments in NAPPES instrument. These instrument equipped with laboratory x-ray sources/ synchrotron source, Electrostatic lenses and differential pumping stages between the sample compartment to hemispherical analyzer.[27] However, the first two efforts did not sustain after initial studies, due to various problems, especially in handling the high pressure. Thereafter many efforts are introduced into in the PES unit, without compromising the spectral quality to fulfil the pressure gap as much as possible.[28] Today, NAPPES became a multidisciplinary tool used in various fields such as energy materials, solid-gas interfaces, catalysis, dielectric oxides, aerosols, electrochemistry, solid-liquid interfaces and operando spectroscopy as evidence by number of research articles in the last 10 years.[29-34] The mm-scale mean free path of electrons with

kinetic energies (KE) 100-1000 eV in high pressure gas phase atmosphere (say 1 mbar) makes the NAPPES a strongly desired surface-sensitive method to understand the materials under working conditions or close to that.

Recent developments in lab based NAPPES with small spot size and monochromatised x-ray source with high photon flux allows for solid surfaces to probe at ambient conditions. Today, NAPPPS systems are commercially available and growing in demand with instruments available at synchrotrons as well as individual laboratories around the world. Among those, a custom-built laboratory based NAPPES unit was installed in 2012 at National chemical laboratory, Pune, India. Here we can able to probe the surfaces up to 1 mbar pressure with core level x-ray photoelectron spectroscopy and 0.3 mbar with ultra violet photoelectron spectroscopy with temperatures up to 900 K.[35,36] The complete details about principle and design aspects will be discussed in chapter 2. However, few important applications of NAPPES in catalysis are discussed in the next section.

1.5. Electronic structure evolution of materials and its relevance to catalysis

A survey on literature related to NAPPES studies of heterogeneous catalysis reaction illustrates the chemistry of a catalyst surface during catalysis is crucial towards understanding the catalytic process. However tracking a catalyst surface under relevant catalysis condition can provide a significant output on the surface electronic structure and catalyst nature; it also helps to establish a fundamental correlation between the catalytic performance and mechanistic aspects of the catalytic reaction. The recent development in surface science and development of NAPPES gives us an excellent opportunity to study the "real" surfaces under real world (or close to that) catalysis conditions and opens a new and vital chapter in the area of surface science by bridging the existing pressure gap and material gap.

1.5.1. Gas-solid interaction

Understanding the chemical reactions on catalyst surfaces, especially gas-solid interaction is very important process in heterogeneous catalysis. Among those, catalytic CO oxidation is a very important reaction in three way catalytic converters and more extensively studied model reaction in surface science to understand the surface nature and surface properties. Turner et al. investigated the temporal oscillations in CO oxidation reaction in (non-)steady state conditions over Pt surface under low pressure condition.[37] However, for

the first time Ertl et al. performed kinetic oscillations on well defined Pt (111) surfaces under UHV conditions. According to the reaction mechanism the high sticking co-efficient of CO and the consequent surface reconstruction strongly inhibit the dissociative adsorption of O_2. While clean or relatively low-covered CO surfaces allows oxygen adsorption and dissociation. However, under reaction conditions, both extremes occurs and this leads to an oscillation in the rate of the reaction at a given temperature and hence non-linear kinetics. As a result, significantly high temperature is required (>400 K) during the steady state flow condition to maintain continuous desorption of CO adsorbates to create the free adsorption sites.[38,39] Gopinath et al. have demonstrated a shift in catalysis regime by surface modification. By diffusing oxygen atoms into the subsurfaces of Pd-layers, significantly electron-deficient Pd-surface (or cationic $Pd^{+\delta}$) was generated. This leads to the weakening of CO-chemisorption (hence CO-poisoning is lifted), and makes CO more mobile on the surface even at 350 K. On unmodified Pd(111) surfaces, strong CO chemisorption is observed and reported by many others, which prevents oxygen adsorption and hence effectively no steady state CO oxidation activity was observed below 400 K. It is to be noted that back-bonding from Pd to CO is minimized due to cationic nature of modified Pd(111) surfaces. These types of relevant mechanistic understanding is possible from in-situ surface science methods under technically relevant conditions.[40]

In transition metal oxides, adsorption of water vapour on catalyst surface inhibits catalytic activity due to blockage of active sites. This was a serious problem in heterogeneous catalysis, and it leads to deactivation of catalyst. In the same line Jain et al. investigated the surface electronic structure changes of Co_3O_4 nanorod under CO oxidation conditions with water vapour and without it. In the presence of water vapour (and CO + O_2), reaction opens in a new path way and formation of carbonate and formate species were observed.[41,42] These types of studies may help in the catalysis, where water as a usual part of the reaction. As mentioned above, progress in surface science techniques, especially NAPPES, along with well developed colloidal synthesis methods made a new insight in the surface characterisation of working nano catalyst. Qadir et al. investigated the different size Ru nanoparticle surface (2.8 and 6 nm) active species under reducing, oxidising and CO oxidation reaction conditions using NAPPES. In mild oxidative and reduction conditions, extent of oxide formation (RuO_2) depended on the particle size. Ru nanparticles with higher size (6 nm) contains a less oxide thickness shown more activity (CO oxidation) than 2.8 nm nanoparticles under reactions conditions of 56-200 ^oC temperature.[43] Dubey et al. prepared porous ceria-zirconia thin films

on silicon wafer and addressed the fundamental aspects such as adsorption, diffusion, and other elementary reaction steps, heat and mass transfer by using MBI and NAPPES.[5,33,44,45] These kind of in-situ observations of nanoparticles are useful in identifying the active state of the catalysts during use and, hence, may allow for rational catalyst designs for practical applications.

A dynamic change in the electronic structure of Au surface was observed by Alexander et al. during oxidation under 0.3 mbar of O_3 with NAPPES at temperature 100 ^oC. Au foil shows the low coordinated Au atoms along with gold-oxide phase, however, oxide phase is restricted to the few surface layers (between 0.29 nm to 0.58 nm), unstable and disappeared with increasing of temperature or pumping out O_3 gas. Thus low coordinated gold observed during oxidation and it's not disappearing even after pumping down to UHV and same conclusions was supported with ex-situ SEM.[46] Silver supported on metal oxides is a commercially available heterogeneous catalyst for ethylene epoxidation. Despite being complete combustion to CO_2, silver makes kinetically controlled oxidation to ethylene oxide. Here plays the role of gas-solid interaction to understand the kinetically controlled oxidation of Ag. To address this aspect, Ghoslaya et al. investigated the Ag-O_2 interaction by using NAPUPS up to 0.2 mbar pressure between 295 to 550 K temperatures. Ag surface work function remains the same at 4.9 eV under 0.1 mbar O_2 and up to 390 K. Thereafter it changes from 4.9 to 5.3 eV between 390 and 450 K; further increase in temperature increases the work function to 5.7 eV. Dissociatively adsorbed O atoms diffused into the sub surface layers of Ag occurs between 390 and 450 K, and hence the Ag surface becomes electrophonic in nature.[29]

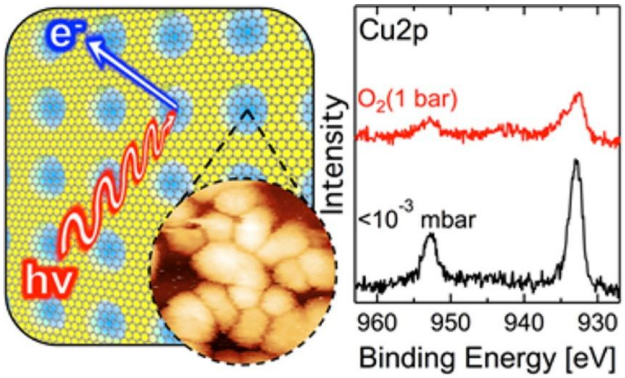

Figure 1.5: Sketch of the graphene-based membrane and XPS Cu 2p spectra at 10^{-3} and 1 bar pressure of O_2 at room temperature. From Ref 47; Copyright permission obtained from ACS.[47]

Salmeron et al. had shown the dynamic oxidation of Cu metal to Cu^{+2} in 1 bar pressure of O_2 using single layer graphene membrane. This graphene act as the support for Cu nanoparticles, photoelectron transparent and protects pressure gradient from analysis chamber to detector as shown in Figure. 1.5. Where Cu^{2+} oxidation state is very stable in 1 bar O_2 however, it's reduced spontaneous in vacuum to Cu metal.[47]

Transition metal oxides supported gold catalyst is mostly used in oxidation reactions, where the support can play an important role.[48] Using Au nanoparticles inside meso and micro porous materials (with broad particle size distribution, around 2–8 nm) forms various CO and NO complexes depending on particle size, loading, catalyst structure, temperature, and pressure.[49,50] The first step in the CO + NO reaction is the adsorption of the reactants. There are few references in the literature dealing with NO adsorption over Au/TiO_2.[51,52]

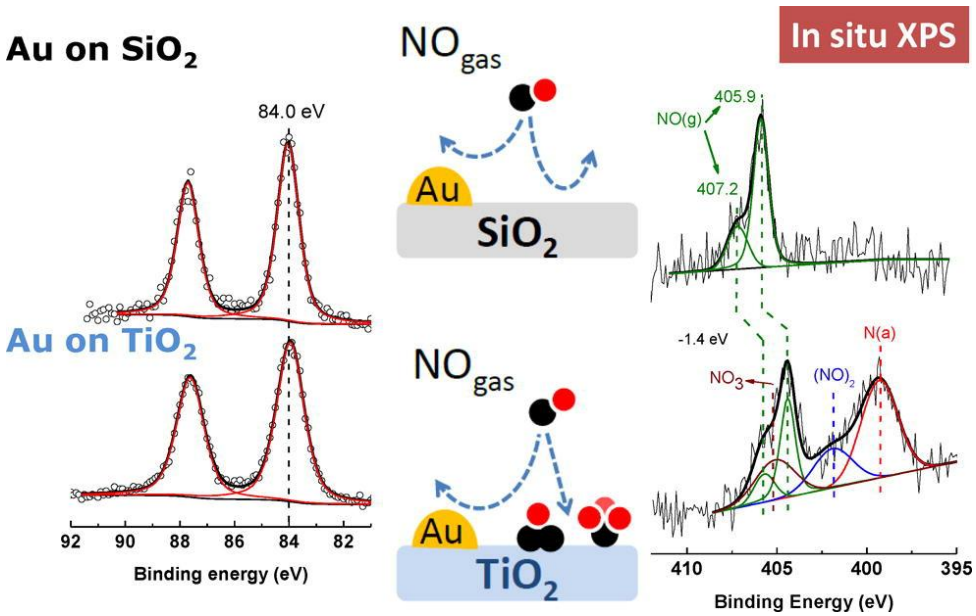

Figure 1.6: Au 4f and N 1s XPS spectra of 4 nm Au nanoparticle deposited on TiO_2 and SiO_2 thin films in the presence of 240 m Torr of NO. From Ref 53; Copyright permission obtained from Elsevier.[53]

NAPPES has been used to study the adsorption of nitric oxide (NO) and molecular oxygen (O_2) over gold-based model catalysts consisting of mono-dispersed nanoparticles with different diameters (2-5 nm) supported on poly crystalline TiO_2, SiO_2. NAPPES experiments revealed that NO and O_2 adsorb only on the TiO_2 support and gives rise to various N-containing species as shown in the Figure. 1.6. Band bending effects caused by the adsorption of NO and O_2 on the TiO_2 substrate resulted in binding energy shifts of the Ti 3p,

O 1s, and N 1s peaks. Interesting changes in the width of the Au 4f core level peaks were observed that depend on particle size. Understanding the origin of this size dependent broadening may yield clues to the enhanced catalytic activity of small Au nanoparticles in CO oxidation reactions. Tao et al. studied the restructuring of the core shell $Rh_{0.5}Pd_{0.5}$ and $Pt_{0.5}Pd_{0.5}$ bimetallic nanoparticles under in-situ oxidising (NO or O_2), catalytic (NO, CO) and reducing (CO, H_2) conditions using synchrotron NAPPES. They observed the different chemical structure and composition of both nanoparticles under same reaction conditions. This results demonstrates the reaction driven tunability of bimetallic nanoparticles structure.[54] Above studies shows the importance of gas-solid interaction and the dynamic changes of surface electronic structure under relevant conditions.

1.5.2. Work function changes

The catalytic activity of surfaces is controlled by many parameters such as binding energy of reactants, intermediates, products, co-adsorbates, impurities and surface morphology etc. Understanding of these different aspects leads to a huge impact on the reactivity of a surface and it helps to improve the design aspects of catalysts. Further, various microscopic phenomena of any catalytic reaction will be affected by the work function (ϕ) of the catalytic material; in fact, chemisorption itself would induce changes in the ϕ of the solid surface, due to formation of chemical bonds and effectively there are changes in the density of states of the solid surface. ϕ is defined as the minimum energy required to remove an electron from the Fermi level (E_F) of the solid to vacuum level. It is a key property of any materials or devices due to its surface sensitive nature. In metals there is no gap between the conduction band (CB) and valence band (VB) and E_F lies at the interface of VB and CB. In comparison to a metal, semiconductors and insulators exhibit an absence of electronic states at and around the E_F. Therefore, the ϕ of semiconductors/insulators is not equivalent to the ionization energy (E_{ion}) and electron affinity (χ). Any surface ϕ can be contributed by two parameters, 1. Electron chemical potential 2. Surface dipole (δ). Electron chemical potential represents the E_F to absolute vacuum level and additional energy required to remove electron from the surface called as dipole charge.[55] Variation of the vacuum level without a change of the E_F is a result of the formation of a surface dipole. Oxidation state, impurities, crystal structure defects can change the electron chemical potential. However, dipole charge can be altered by surface reconstruction, surface orientation and mostly by presence of adsorbates, particularly by chemisorbed species. Generally surface dipole charge caused by charge

transfer across the interface. A negative surface charge causes an increase of the surface dipole and a positive surface charge causes a decrease of the surface dipole, i.e. a work function reduction. It's to be noted that measured ϕ is more of materials conditions than material constant. However, some materials like Au, Cu show the reproducible ϕ in UHV. A detailed description about how to measure the work function changes under reaction conditions with NAPPES will be discussed in chapter-2.

1.5.3. Surface chemistry of CO_2

Rapid developments in the industries are increasing the global energy demands and there is no sign of slowing down of energy consumption. It is estimated that energy needs by 2050 will become 80 % higher than current consumption, that will be highly impossible to satisfy with our present conventional resources.[56] Accompanying to the global energy demands, carbon dioxide concentration is increasing in the atmosphere and causes global warming and ocean acidification. Hence there is an urgent need for the mitigation of CO_2 in the atmosphere by capture and storage or conversion into commodity chemicals. Carbon neutral (and possibly carbon negative) concept is one of the important points to recycle the atmospheric CO_2 by its activation and generate a useful feedstock. However, due to high stability of CO_2 molecule (linear and symmetric molecule) with other possible products, it is highly challenging task to the scientific community to reduce it and convert to other chemicals. In order to activate CO_2, a suitable catalyst with an active site for CO_2 adsorption and an ample amount of energy are required.

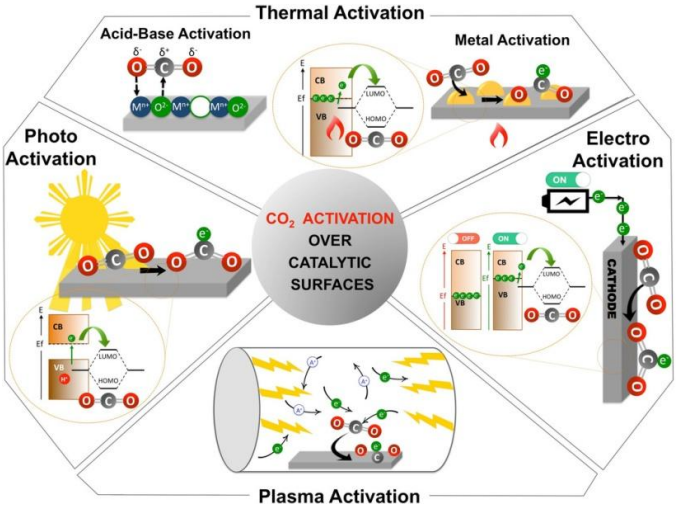

Figure 1.7: Various approaches of CO_2 activation over catalyst surfaces. From Ref 57; Copyright permission obtained from Wiley.[57]

As shown in Fig. 1.7 various approaches are being employed in the CO_2 activation over catalytic surfaces. Among those, CO_2 hydrogenation with metal supported on metal oxides is a leading approach in the industries. Various surface science techniques have been employed to study the CO_2 adsorption on many catalyst surfaces to understand active sites for the CO_2 adsorption. Initially, Eren et al. studied the CO_2 dissociative adsorption on both Cu (100) and Cu(111) surfaces with NAPPES and HP-STM (high pressure scanning tunnelling microscope. They found that dissociative adsorption of CO_2 is more in the case of Cu(100) than Cu(111) and left over atomic oxygen block the surface for further adsorption of CO_2. For the same reason, in industries mix the CO to feed to remove the oxygen.[58]

Similarly, Xingyi et al.[59] studied the surface chemistry of clean Cu, Cu_2O and Zn/Cu (0.1 monolayer (ML)) surfaces in 0.1 Torr of CO_2 alone and mixture (0.1 Torr CO_2 + 0.1 Torr H_2O) at room temperature using NAPPES. Initially, Cu foil in the presence of 0.1 Torr CO_2 shows the presence of chemisorbed $CO_2^{\delta-}$ and C^0, which only exist in the gaseous environment, however, no species formed on the Cu_2O. This observation reveals the importance of Cu-oxidation state in the activation of CO_2. After deposition of Zn (0.1 monolayer) on Cu foil $CO_2^{\delta-}$ converted to carbonate (CO_3^{-2}). In addition to the species ($CO_2^{\delta-}$, C^0, $CO_2^{\delta-}$) observed in pure CO_2, methoxy, hydroxyl and formate species are also observed in the mixture of 0.1 Torr of CO_2 and 0.1 Torr of H_2O, which gives the hydrogen required for the reaction. These studies are helpful in the fundamental understanding of catalytic reactions like methanol synthesis, water gas shift reaction and photo catalysis for CO_2 activation.[60-62]

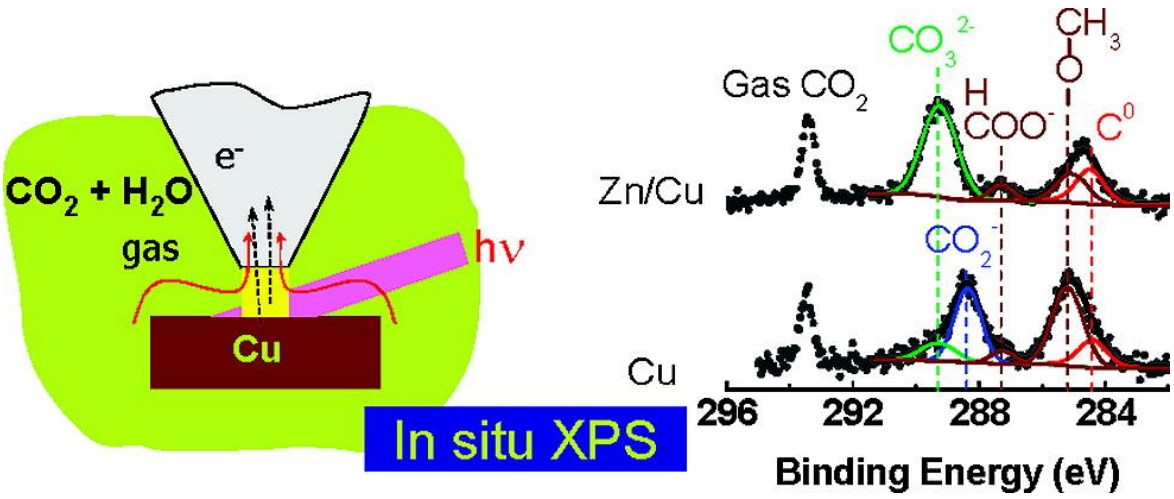

Figure 1.8: XPS C 1s spectra of pure Cu and Zn/Cu (0.1 ML Zn) in the presence of mixture of 0.1 Torr of CO_2 and 0.1 Torr of H_2O at room temperature. From Ref 59; Copyright permission obtained from ACS)[59]

There are some other catalysts reported in the literature, where in-situ reaction was performed for CO_2 activation studies. Hao et al. studied the effect of CO_2 activation on the ZrO_2 film by co-adsorption of H_2O with NAPPES and IRRAS. After dosing 2×10^{-2} mbar of CO_2 at room temperature on the ZrO_2 surface, they did not observe any carbonaceous species on the surface. Whereas after co-adsorption of H_2O (CO_2+ H_2O), carbonaceous species were observed on the surface. Apparently CO_2 was activated and surface species like formate, dioxymethylene, formaldehyde and carbon were observed.[63]

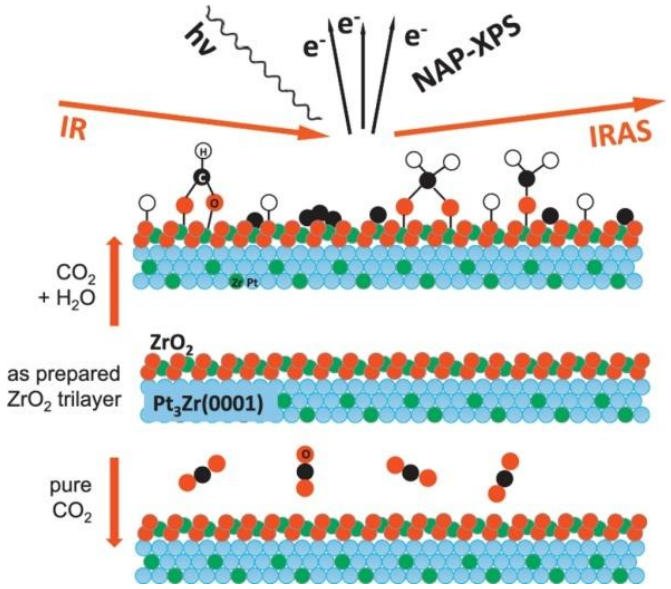

Figure 1.9: Schematic illustration of effect of co-adsorption of water on the carbon dioxide activation. From Ref 63; Copyright permission obtained from Elsevier.[63]

Currently, an active metal, bimetal or alloy of the following metals (Ru, Ni, Cu, Pd and Pt) supported on an oxide (eg. SiO_2, Al_2O_3, TiO_2, ZrO_2, CeO_2) are the commonly used catalyst for the evaluation of CO_2 hydrogenation. However, due to their complexity and cost, above systems limit their widespread use in the industries.[58,64-66] In the recent times, transition metal carbides have attracted special attention due to its similar electronic structure as that of noble metals, and makes carbide as a potential substitute for noble metal catalysts for a wide variety of reactions like reforming,[67-69] hydrogenation,[70] water gas shift reactions.[71-80] Among those metal carbides, molybdenum carbide (Mo_2C) exhibit remarkable catalytic activity due to its unique d band electronic structure, which show very similar to the Pt group metals.[72] Initially, CO_2 adsorption on the Mo_2C (100) surface was studied by Solymosi and observed that CO_2 is weakly and reversibly adsorbed even at 100 K with UHV based technique.[81] Later studies shown that higher reactivity of CO_2 was observed when the

surface metal to carbon ratio is 2.[82] The effect of CO_2 dissociation on the Mo_2C at different oxygen coverage's was calculated by Dixit et al. by using DFT. DFT calculations predicted that CO_2 chemisorption no longer occurs on the Mo_2C surface, if it is pre-covered with >0.5 ML of oxygen.[83]

In-situ XPS and XANES studies show the oxycarbide is an active phase for CO_2 hydrogenation to CO.[84] In spite of that, there is no consensus about the role of carbide/oxycarbide and work function changes in the activity for CO_2 hydrogenation to CO. However understanding the mechanism and catalyst surface structure under in-situ reaction conditions are always critical for further improving the activity and selectivity of the catalyst.

1.6. Objectives of the thesis

Present thesis is focused to utilize NAPPES technique to explain the surface chemistry behind chemical conversions, reaction mechanisms and active states of the catalyst surfaces under working conditions. We emphasize the application of the technique for the fundamental studies and its utilization to unravel the events that occur under real world conditions. Transition metal oxides and carbides are capable of exhibiting a wide range of oxidation states with different work functions.[85] This quality allows them to be used in many applications that involve charge transfer with adsorbed molecules.[86] Charge exchange at the interfaces mainly depends on the surface energies, especially work function; this is mainly due to the addition or removal of electron to/from the surface and work function depends on it. Tuning the surface ϕ of the materials is of a great deal of interest for a wide range of surface and interface-based devices and applications. How the ϕ of a solid surface changes under the reaction conditions is of paramount interest to the chemists, particularly in the areas of surface dependent phenomena such as, catalysis and electrochemistry. Catalysis aspects/results are often fully not reproducible due to various reasons; difficulty in maintaining a same or similar electronic structure and surface chemical composition are the prime reasons. A minor change in the reaction condition or different catalyst preparation methods lead to a different set of results in catalysis, often due to changes in the electronic and structural factors. Surface electronic structure plays a dominant role in catalysis and how it changes as a function of reaction parameters is hardly studied by valence band (VB) photoelectron spectroscopy (PES) with low energy photons. VB changes of catalysts with ultraviolet PES (UVPES) under different reaction conditions are of paramount interest, as they explore only the surface changes (~2 nm), which decide the catalysis or any surface

dependent physical and chemical properties. Some of the important parameters, such as changes in E_F and change of ϕ, can be determined in the presence of pressure and temperature by NAPUPS and we addressed these aspects in the working chapters 3 and 4.

Carbon dioxide reduction is a challenging process among the scientific community. It is also a necessity to address this issue urgently, due to effects in global warming felt across the nations. It needs a suitable catalyst and external energy as an input to convert into value added chemical; this would simultaneously helps to reduce the dependency of fossil fuels. However most of the catalyst used in this process was noble metals over reducible oxides as support. Most of the reported catalysts are not cost effective, complex structures and unstable at high temperature and makes them unsuitable for wide spread use in industries. In searching for an active and cost effective catalyst, we found that molybdenum carbide (Mo_2C) as an alternative and potential catalyst for the hydrogenation of CO_2. The role of surface structure, carbide/oxycarbide and work function changes of Mo_2C under relevant conditions and its activity are addressed in the chapter 5.

1.7. Outline of the thesis

Oxidation and reduction are the two important classes of reactions in catalysis and how the catalyst interacts under these conditions is a pre-requisite to understand the ensuing catalysis. Further, how the phase formation occurs is very relevant from material as well as catalysis point of view. All three working chapters (Chapters 3-5) address these issues. In **chapter 3** valence band (VB) and core level photoelectron spectroscopy was carried out to investigate the electronic structural changes from polycrystalline Co to spinel Co_3O_4, via CoO at near ambient pressures (NAP; 0.1 mbar). O_2−Co and H_2−CoO_x gas−solid oxidative and reductive interactions, respectively, have been explored with UV photons (He−I) or low kinetic energy electrons (≤16 eV) under NAP conditions. Typical VB features of Co metal; CoO, Co_3O_4, and a mixed phase between any two adjacent features were observed and well corroborated with core level changes. Very significant and characteristic changes were observed with Co 3d features in the VB for each stage from Co oxidation to Co_3O_4 as well as Co_3O_4 reduction to CoO. Co_3O_4 and CoO can be reversibly obtained by alternating the conditions between 0.1 mbar of H_2 at 650 K and 0.1 mbar of O_2 at 400 K, respectively. A meaningful correlation is observed between the changes in the ϕ with cation oxidation state; small changes in the stoichiometry can strongly influence the shift in E_F. Reversible ϕ changes are observed between oxidation and reduction conditions. While the O 2p derived

feature for CoOx was observed at a constant BE (~5 eV) throughout the redox conditions, the Co 3d band and molecular oxygen or hydrogen vibration feature shifts significantly underscoring the physicochemical changes, such as charge transfer energy and hence changes in satellite intensity. The peak close to E_F originated from the $3d^6\underline{L}$ final state ($\underline{L}$ indicating charge transfer from O-ligand to Co-metal) of the octahedral Co^{3+} 3d band of Co_3O_4. A meaningful correlation is observed between the changes in ϕ with cation oxidation state; small changes in the stoichiometry can strongly influence the shift in E_F and changes in ϕ under NAP conditions. It is to be mentioned that ϕ changes alters the valence band edge energy and directly affects the reaction. Reversible ϕ changes are observed between oxidation and reduction conditions. While the O 2p derived feature for CoO was observed at a constant BE (~5 eV) throughout the redox conditions, the Co 3d band and molecular oxygen or hydrogen vibration feature shifts significantly underscoring the physicochemical changes, such as charge transfer energy and hence changes in satellite intensity. The peak close to E_F originated from the $3d^6\underline{L}$ final state of the octahedral Co^{3+} 3d band of Co_3O_4.

Tuning the surface energetics, especially ϕ of the materials is a great deal of interest for the wide range of surface and interface based devices and applications. How the ϕ of a solid surface change under the reaction conditions is of paramount interest to the chemists, particularly to the areas of surface dependent phenomena such as catalysis, electrochemistry. In the **chapter 4**, by using valence band and core level photoelectron spectroscopy, surface electronic changes from Mo to MoO_3 via MoO_2 was studied under relevant near ambient pressure and high temperature conditions. Very significant change in the ϕ from Mo to MoO_3 was observed and it is well corrborated with the changes in gas-phase vibrational features of O_2 in both NAPUPS as well in NAPXPS. Reversible changes in the electronic structure are observed when MoO_3 was reduced in H_2 to MoO_2. Based on the extent of oxidation/reduction of MoO_x, NAPUPS has shown, one or two additional peaks in the band gap at 0.6 and 1.6 eV below the E_F. Mo^{5+} features are identified in the VB and in the Mo 3d core levels with distinct features. Mo^{5+} features are also stable and essential to bridge MoO_2 and MoO_3 layers, and their co-existence. In addition, characteristic changes in Mo 4d and O 2p features observed from Mo to MoO_3 and well correlated to the band gap of MoO_3. Oxidation and reduction propagate from the surface to bulk; indeed this has significant implications in surface dependent phenomena. The present study demonstrates (a) the uniqueness of NAPUPS in identifying the subtle to large changes in the electronic structure on solid surfaces under common oxidation and reduction (in general, under reaction) conditions, and

(b) relevance of NAPUPS to all surface dependent phenomena, such as catalysis, electrochemistry.

The materials gap can be partly bridged by refining the model systems and, e.g., powder metal carbides, polycrystalline foil. One example of such a model system for CO_2 hydrogenation catalyst is given in **chapter 5**. Carbon dioxide is a greenhouse gas, needs to be converted into one of the useful feedstock, such as carbon monoxide, methanol. We evaluated the hydrogenation of CO_2 using hydrogen as reducing agent, via reverse water gas shift reaction (RWGS) by using a potential and low cost Mo_2C catalyst. Mo_2C was studied for CO_2 hydrogenation as a function of temperature, CO_2:H_2 ratio. It is demonstrated that Mo_2C catalyst with 1:3 ratio of CO_2:H_2 is highly active and selective towards carbon monoxide at 723 K and particularly at ambient pressure. XRD and Raman analysis shows the Mo_2C remains stable before and after the reaction. Further we evaluated the mechanistic aspects of the RWGS reaction by NAPXPS with Mo_2C generated in-situ from carbonisation of Mo-metal foil. NAPXPS measurements were carried out at near ambient pressure (0.1 mbar) and various temperatures. Throughout the reaction, no significant changes in the Mo^{2+} oxidation state (of Mo_2C) was observed indicating the catalyst is highly stable; C and O 1s spectral results indicates the oxycarbide species as an active intermediate for RWGS. A good correlation is observed between catalytic activity from atmospheric pressure reactors with the electronic structure details from NAPXPS results establish the structure-activity relation. Chapter 6 summarizes the work reported in the current thesis and a possible future outlook.

1.8. References

(1) Redhead, P. A. *J. Vac. Sci. Technol.* **1994**, *12*, 904-914.

(2) Ertl, G. *Catal. Rev.* **1980**, *21*, 201-223.

(3) Liu, J.; Xu, M.; Nordmeyer, T.; Zaera, F. *J. Phys. Chem.* **1995**, *99*, 6167-6175.

(4) Johánek, V.; Schauermann, S.; Laurin, M.; Gopinath, C. S.; Libuda, J.; Freund, H. J. *J. Phys. Chem. B* **2004**, *108*, 14244-14254.

(5) Dubey, A.; Kolekar, S. K.; Gnanakumar, E. S.; Roy, K.; Vinod, C. P.; Gopinath, C. S. *Catal. Struct. React.* **2016**, *2*, 1-12.

(6) https://www.psi.ch/swissfel/chemical-time-scales

(7) Velu, S.; Suzuki, K.; Gopinath, C. S.; Yoshida, H.; Hattori, T. *Phys. Chem. Chem. Phys.* **2002**, *4*, 1990-1999.

(8) Hind, A. R.; Bhargava, S. K.; McKinnon, A. *Adv. Colloid Interface Sci.* **2001**, *93*, 91-114.

(9) Coenen, K.; Gallucci, F.; Mezari, B.; Hensen, E.; van Sint Annaland, M. *J. CO_2. Util.* **2018**, *24*, 228-239.

(10) Binnig, G.; Rohrer, H.; Gerber, C.; Weibel, E. *Phys. Rev. Lett.* **1982**, *49*, 57-61.

(11) Leonhard, G. *J. Phys.: Condens. Matter* **2008**, *20*, 053001.

(12) Thirunavukkarasu, K.; Thirumoorthy, K.; Libuda, J.; Gopinath, C. S. *J. Phys. Chem. B* **2005**, *109*, 13272-13282.

(13) Wander, A.; Van Hove, M. A.; Somorjai, G. A. *Phys. Rev. Lett.* **1991**, *67*, 626-628.

(14) Mishra, A. K.; Roldan, A.; Leeuw, N. H. d. *J. Chem. Phys.* **2016**, *145*, 044709.

(15) Lopez, N.; Nørskov, J. K. *J. Am. Chem. Soc.* **2002**, *124*, 11262-11263.

(16) Raval, R. *Chem. Soc. Rev.* **2009**, *38*, 707-721.

(17) Strongin, D. R.; Carrazza, J.; Bare, S. R.; Somorjai, G. A. *J. Catal.* **1987**, *103*, 213-215.

(18) Ertl, G. *Angew. Chem. Int. Ed.* **1990**, *29*, 1219-1227.

(19) Ertl, G. *Angew. Chem. Int. Ed.* **2008**, *47*, 3524-3535.

(20) Bell, A. T. *Science* **2003**, *299*, 1688-1691.

(21) Mizuno, N.; Misono, M. *Chem. Rev.* **1998**, *98*, 199-218.

(22) Maschmeyer, T.; Rey, F.; Sankar, G.; Thomas, J. M. *Nature* **1995**, *378*, 159.

(23) Somorjai, G. A.; Hwang, K. S.; Parker, J. S. *Top. Catal.* **2003**, *26*, 87-99.

(24) Over, H.; Muhler, M. *Prog. Surf. Sci.* **2003**, *72*, 3-17.

(25) Yu, W.; Porosoff, M. D.; Chen, J. G. *Chem. Rev.* **2012**, *112*, 5780-5817.

(26) Siegbahn, H. *J. Phys. Chem.* **1985**, *89*, 897-909.

(27) Joyner, R. W.; Roberts, M. W.; Yates, K. *Surf. Sci.* **1979**, *87*, 501-509.

(28) Hussain, Z.; Huff, W. R. A.; Kellar, S. A.; Moler, E. J.; Heimann, P. A.; McKinney, W.; Padmore, H. A.; Fadley, C. S.; Shirley, D. A. *J. Electron. Spectrosc. Relat Phenom.* **1996**, *80*, 401-404.

(29) Ghosalya, M. K.; Reddy, K. P.; Jain, R.; Roy, K.; Gopinath, C. S. *J. Chem. Sci.* **2018**, *130*, 30.

(30) Ghosalya, M. K.; Jain, R.; Reddy, K. P.; Gopinath, C. S. *J. Phys. Chem. C.* **2018**, *122*, 4331-4338.

(31) F. Cauduro, A. L.; dos Reis, R.; Chen, G.; Schmid, A. K.; Méthivier, C.; Rubahn, H.-G.; Bossard-Giannesini, L.; Cruguel, H.; Witkowski, N.; Madsen, M. *ACS Appl. Mater. Inter.* **2017**, *9*, 7717-7724.

(32) Kim, H.-S.; Cook, J. B.; Lin, H.; Ko, Jesse S.; Tolbert, Sarah H.; Ozolins, V.; Dunn, B. *Nat. Mater.* **2016**, *16*, 454.

(33) Jain, R.; Dubey, A.; Ghosalya, M. K.; Gopinath, C. S. *Catal. Sci. Technol.* **2016**, *6*, 1746-1756.

(34) Du, Y.; Peng, H. Y.; Mao, H.; Jin, K. X.; Wang, H.; Li, F.; Gao, X. Y.; Chen, W.; Wu, T. *ACS Appl. Mater. Inter.* **2015**, *7*, 11309-11314.

(35) Roy, K.; Vinod, C.; Gopinath, C. S. *J. Phys. Chem. C* **2013**, *117*, 4717-4726.

(36) Roy, K.; Gopinath, C. S. *Anal. Chem.* **2014**, *86*, 3683-3687.

(37) Turner, J. E.; Sales, B. C.; Maple, M. B. *Surf. Sci.* **1981**, *103*, 54-74.

(38) Ertl, G.; Norton, P. R.; Rüstig, J. *Phys. Rev. Lett.* **1982**, *49*, 177-180.

(39) Nagarajan, S.; Thirunavukkarasu, K.; Gopinath, C. S. *J. Phys. Chem. C* **2009**, *113*, 7385-7397.

(40) Gopinath, C. S.; Roy, K.; Nagarajan, S. *ChemCatChem* **2015**, *7*, 588-594.

(41) Jain, R.; Reddy, K. P.; Ghosalya, M. K.; Gopinath, C. S. *J. Phys. Chem. C* **2017**, *121*, 20296-20305.

(42) Jain, R.; Gnanakumar, E. S.; Gopinath, C. S. *ACS Omega* **2017**, *2*, 828-834.

(43) Qadir, K.; Joo, S. H.; Mun, B. S.; Butcher, D. R.; Renzas, J. R.; Aksoy, F.; Liu, Z.; Somorjai, G. A.; Park, J. Y. *Nano Lett.* **2012**, *12*, 5761-5768.

(44) Dubey, A.; Kolekar, S. K.; Gopinath, C. S. *ChemCatChem* **2016**, *8*, 3650-3656.

(45) Dubey, A.; Reddy, K. P.; Gopinath, C. S. *ChemistrySelect.* **2017**, *2*, 533-536.

(46) Klyushin, A. Y.; Rocha, T. C. R.; Hävecker, M.; Knop-Gericke, A.; Schlögl, R. *Phys. Chem. Chem. Phys.* **2014**, *16*, 7881-7886.

(47) Weatherup, R. S.; Eren, B.; Hao, Y.; Bluhm, H.; Salmeron, M. B. *J. Phys. Chem. Lett.* **2016**, *7*, 1622-1627.

(48) Xie, X.; Li, Y.; Liu, Z.-Q.; Haruta, M.; Shen, W. *Nature* **2009**, *458*, 746-749.

(49) Valden, M.; Lai, X.; Goodman, D. W. *science* **1998**, *281*, 1647-1650.

(50) Haruta, M.; Kobayashi, T.; Sano, H.; Yamada, N. *Chem. Lett.* **1987**, 405-408.

(51) Comotti, M.; Li, W.-C.; Spliethoff, B.; Schüth, F. *J. Am. Chem. Soc.* **2006**, *128*, 917-924.

(52) Akolekar, D. B.; Bhargava, S. K. *J. Mol. Catal. A: Chem.* **2005**, *236*, 77-86.

(53) Herranz, T.; Deng, X.; Cabot, A.; Liu, Z.; Salmeron, M. *J. Catal.* **2011**, *283*, 119-123.

(54) Tao, F.; Grass, M. E.; Zhang, Y.; Butcher, D. R.; Renzas, J. R.; Liu, Z.; Chung, J. Y.; Mun, B. S.; Salmeron, M.; Somorjai, G. A. *Science* **2008**, *322*, 932-934.

(55) Eichelbaum, M.; Hävecker, M.; Heine, C.; Wernbacher, A. M.; Rosowski, F.; Trunschke, A.; Schlögl, R. *Angew. Chem. Int. Ed.* **2015**, *54*, 2922-2926.

(56) Lewis, N. S.; Nocera, D. G. *Proc. Natl. Acad. Sci.* **2006**, *103*, 15729-15735.

(57) Álvarez, A.; Borges, M.; Corral-Pérez, J. J.; Olcina, J. G.; Hu, L.; Cornu, D.; Huang, R.; Stoian, D.; Urakawa, A. *ChemPhysChem* **2017**, *18*, 3135-3141.

(58) Eren, B.; Weatherup, R. S.; Liakakos, N.; Somorjai, G. A.; Salmeron, M. *J. Am. Chem. Soc.*, **2016**, *138*, 8207-8211.

(59) Deng, X.; Verdaguer, A.; Herranz, T.; Weis, C.; Bluhm, H.; Salmeron, M. *Langmuir* **2008**, *24*, 9474-9478.

(60) Pradhan, S.; Reddy, A. S.; Devi, R. N.; Chilukuri, S. *Catal. Today* **2009**, *141*, 72-76.

(61) Bharad, P. A.; Nikam, A. V.; Thomas, F.; Gopinath, C. S. *ChemistrySelect* **2018**, *3*, 12022-12030.

(62) Mota, N.; Guil-Lopez, R.; Pawelec, B. G.; Fierro, J. L. G.; Navarro, R. M. *RSC Adv.* **2018**, *8*, 20619-20629.

(63) Li, H.; Rameshan, C.; Bukhtiyarov, A. V.; Prosvirin, I. P.; Bukhtiyarov, V. I.; Rupprechter, G. *Surf. Sci.* **2019**, *679*, 139-146.

(64) van den Berg, R.; Prieto, G.; Korpershoek, G.; van der Wal, L. I.; van Bunningen, A. J.; Lægsgaard-Jørgensen, S.; de Jongh, P. E.; de Jong, K. P. *Nat. Commun.* **2016**, *7*, 13057.

(65) Sebastian, K.; Christian, C.; Georg, M. P.; Ib, C.; Jens, S. *Angew. Chem. Int. Ed.* **2014**, *53*, 5941-5945.

(66) Daza, Y. A.; Kuhn, J. N. *RSC Adv.* **2016**, *6*, 49675-49691.

(67) Velu, S.; Satoh, N.; Gopinath, C. S.; Suzuki, K. *Catal. Lett.* **2002**, *82*, 145-152.

(68) Maity, P.; Gopinath, C. S.; Bhaduri, S.; Lahiri, G. K. *Green Chemistry* **2009**, *11*, 554-561.

(69) Maity, N.; Rajamohanan, P. R.; Ganapathy, S.; Gopinath, C. S.; Bhaduri, S.; Lahiri, G. K. *J. Phys. Chem. C* **2008**, *112*, 9428-9433.

(70) Gnanamani, M. K.; Hamdeh, H. H.; Shafer, W. D.; Hopps, S. D.; Davis, B. H. *Appl. Catal., A.* **2018**, *564*, 243-249.

(71) Li, Z.; Choi, J.-S.; Wang, H.; Lepore, A. W.; Connatser, R. M.; Lewis, S. A.; Meyer, H. M.; Santosa, D. M.; Zacher, A. H. *Energy Fuels* **2017**, *31*, 9585-9594.

(72) Levy, R. B.; Boudart, M. *Science* **1973**, *181*, 547-549.

(73) Claridge, J. B.; York, A. P. E.; Brungs, A. J.; Marquez-Alvarez, C.; Sloan, J.; Tsang, S. C.; Green, M. L. H. *J. Catal.* **1998**, *180*, 85-100.

(74) Chen, Y.; Choi, S.; Thompson, L. T. *J. Catal.* **2016**, *343*, 147-156.

(75) Yao, S.; Zhang, X.; Zhou, W.; Gao, R.; Xu, W.; Ye, Y.; Lin, L.; Wen, X.; Liu, P.; Chen, B.; Crumlin, E.; Guo, J.; Zuo, Z.; Li, W.; Xie, J.; Lu, L.; Kiely, C. J.; Gu, L.; Shi, C.; Rodriguez, J. A.; Ma, D. *Science* **2017**, 357, 389-393.

(76) Kunkel, C.; Vines, F.; Illas, F. *Energ. Environ. Sci.* **2016**, *9*, 141-144.

(77) Velu, S.; Suzuki, K.; Vijayaraj, M.; Barman, S.; Gopinath, C. S. *Appl. Catal., B.* **2005**, *55*, 287-299.

(78) Velu, S.; Suzuki, K.; Gopinath, C. S. *J. Phys. Chem. B* **2002**, *106*, 12737-12746.

(79) Subramanian, V.; Gnanakumar, E. S.; Jeong, D.-W.; Han, W.-B.; Gopinath, C. S.; Roh, H.-S. *Chem. Commun.* **2013**, *49*, 11257-11259.

(80) Mathew, T.; Sivaranjani, K.; Gnanakumar, E. S.; Yamada, Y.; Kobayashi, T.; Gopinath, C. S. *J. Mater. Chem.* **2012**, *22*, 13484-13493.

(81) Solymosi, F.; Oszkó, A.; Bánsági, T.; Tolmacsov, P. *J. Phys. Chem. B.* **2002**, *106*, 9613-9618.

(82) Jean-Luc, D.; Kazuhiro, S.; Hironori, A. *Chem. Lett.* **1992**, *21*, 5-8.

(83) Dixit, M.; Peng, X.; Porosoff, M. D.; Willauer, H. D.; Mpourmpakis, G. *Catal. Sci. Technol.* **2017**, *7*, 5521-5529.

(84) D., P. M.; Xiaofang, Y.; Anibal, B. J.; G., C. J. *Angew. Chemie. Int. Ed.* **2014**, *53*, 6705-6709.

(85) Greiner, M. T.; Chai, L.; Helander, M. G.; Tang, W.-M.; Lu, Z.-H. *Adv. Funct. Mater.* **2012**, *22*, 4557-4568.

(86) Lin, Z.; Wan, W.; Yao, S.; Chen, J. G. *Appl. Catal., B* **2018**, *233*, 160-166.

Chapter-2

Experimental methods, Insitu and Ex-situ charactrisation studies

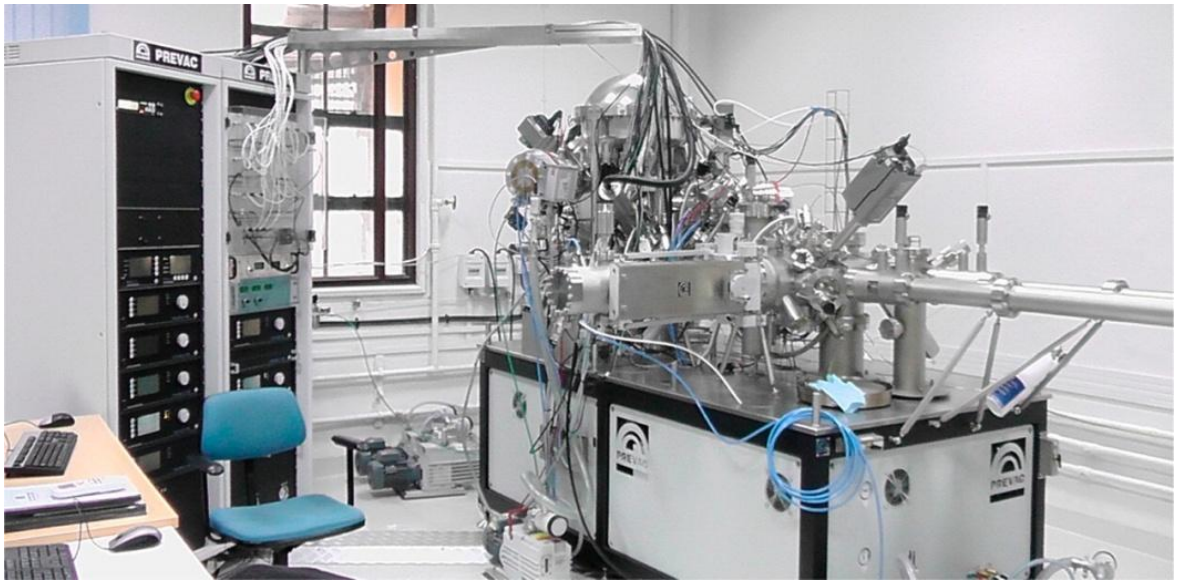

2.1. Introduction

There are various surface science techniques to characterize the catalyst surfaces. None of the single technique can give complete details about the surface structure. However, combination of these techniques can give elementary information like surface adsorption of reactants, diffusion to active sites, intermediates, possible products, changes in surface electronic structure and morphology and correlation between a catalytic performance and possible intermediate(s). Among those techniques, photoelectron spectroscopy is a powerful technique that is inherently surface sensitive, elemental, chemical specific and more importantly, we can use it as an in-situ technique known as NAPPES. In this chapter we discuss about the history, principle and design aspects of in-situ x-ray photo electron spectroscopy (or NAPPES), experimental conditions and measurements of work function changes under reaction conditions. We also describe about the sputter cleaning of metal foils and wet chemical synthesis of Mo_2C powder catalyst. Further we discussed about various ex-situ characterisation techniques like powder X-ray diffraction (XRD), Energy dispersive x-ray analysis (EDAX), Raman spectroscopy, scanning electron microscopy (SEM), Temperature-programmed desorption (CO_2-TPD) and Temperature programmed reduction (H_2-TPR) principles and its experimental conditions. Reaction procedure for CO_2 hydrogenation with Mo_2C catalyst and analysis method of various products is explained.

2.2. Photoelectron spectroscopy

Photoelectron spectroscopy (PES) is an elemental and chemical specific surface technique that enables to probe the changes in the occupied states of solids and molecules in sub monolayer resolution. PES works based on the principle of photoelectric effect and Heinrich Hertz was among the first to discover the effect; Albert Einstein, the first physicist, to describe principle based on quantized concept of electronic structure of atoms and molecules. However, complete experimental setup of high resolution photoelectron spectrometer was reported by Kai Siegbahn with his research group at Uppsala (Sweden) in 1954.[1] In PES, surface of sample is illuminated with radiation of sufficient energy; incident photons generated photoelectrons and helped to analyse the chemical identity of the material surfaces. Excess energy or kinetic energy associated with ejected electrons are measured by analyzer.[2] The Kinetic energy (E_{KE}) of emitted photoelectrons depends on the binding energy (E_b) of the electron in the orbital and the incident photon energy ($h\upsilon$). Energy conservation is governed by the following photoelectric effect equation (Eq. 2.1),

$$E_{K.E} = h\vartheta - E_b - \Phi \qquad \text{(Eq. 2.1)}$$

Binding energy is the energy required to excite the electron from any occupied orbital level to the Fermi level, and is the characteristic feature of any element in periodic table. The additional energy required to take it out the electron from Fermi level (E_F) to vacuum level, is called the work function (Φ) and it depends on the nature of the sample surface and analyzer. The remaining energy is the kinetic energy of photoelectron which varies with the incident photon energy. As shown in Fig. 2.4, conducting sample is in electrical contact with analyzer in order that both analyzer and sample have the common reference for measuring photo electron energy called E_F.[3] The incoming photons create a photoelectron with E_{KE} relative to the vacuum level of the sample is given by Eq. 2.2,

$$E_{K.E} = h\vartheta - E_b - \Phi_{sample} \qquad \text{(Eq. 2.2)}$$

However, the work function of the analyzer is different from the sample work function and hence in order to be detect the photoelectron, it has to overcome the contact potential difference

$$(\Phi_{analyser} - \Phi_{sample}). \qquad \text{(Eq. 2.3)}$$

$$E_{K.E} = h\vartheta - E_b - \Phi_{sample} - (\Phi_{analyser} - \Phi_{sample}) \qquad \text{(Eq. 2.4)}$$

$$E_{K.E} = h\vartheta - E_b - \Phi_{analyser} \qquad \text{(Eq. 2.5)}$$

As a result, obtained binding energy is independent of ϕ_{sample}.
Since Fermi level is equilibrated, the kinetic energy values can be converted to binding energy and $\Phi_{analyzer}$ already known.[4]

Depending on the source of ionisation energy, PES can be divided into Ultra-violet photoelectron spectroscopy (UPS) and X-ray photoelectron spectroscopy (XPS). In UPS usually He-I (hυ = 21.2 eV) used as a source, this energy is sufficient to knock out the electron from the valence orbital. Moreover electron energies (Mg kα =1253.6 eV and Al kα = 1486.6 eV) used in XPS, can able to knock out the electrons from many core level orbital as well as valence orbital. Each core level electron of any atomic/molecular orbital has a specific binding energy; it gives presence of elements in the sample and its oxidation state.

UPS give information about hybridisation, fermi level energy and work function information of the material, is mostly dependent on the surface.[5,6]

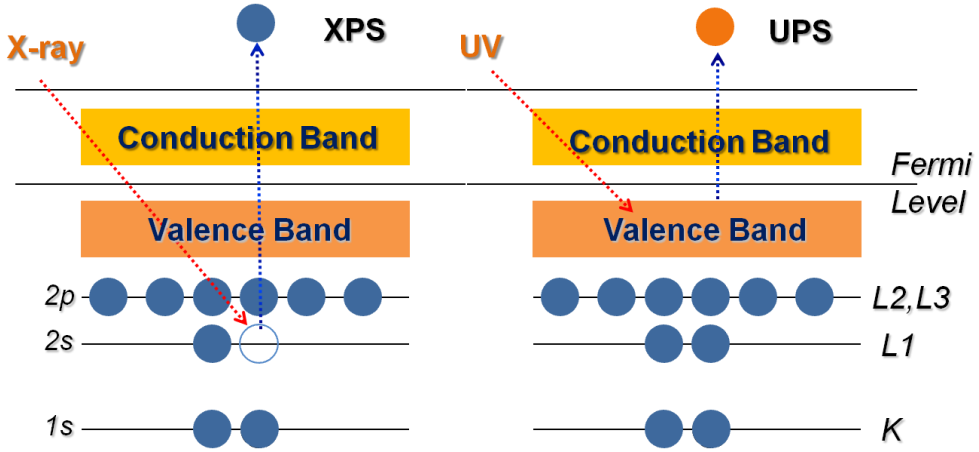

Figure 2.1: Photo ionisation in x-ray photoelectron spectroscopy and ultraviolet photoelectron spectroscopy.

Sample analysis requires ultrahigh vacuum (UHV), typically of the order of 10^{-10} mbar, and this facilitates the reaching of photoelectrons to the detector without losing its energy. More importantly, PES is a highly surface sensitive with few nm depth probing and hence very high vacuum conditions are required to minimize the re-contamination rate of the sample. As a result of photo excitation process, element will become photo ionized and the photo emitted electron can be detected by spectrometer. Probability of the photo ionisation, called photo ionisation cross section, varies with the orbitals of the electrons where it originates from.

In order the electron spectroscopy to be more effective, the emitted photoelectron should be ejected from the atom/molecule and into the vacuum level and finally it should reach the electron energy analyzer. An average distance that a photoelectron can travel without suffering energy losses by inelastic collisions within a solid called inelastic mean free path (IMFP). The larger the KE, the longer the IMFP. The electrons within the probing depth can be ejected without losing its KE. Emitted photoelectrons are collected by the set of electrostatic lens units and transferred it through the apertures and focused onto the analyzer entrance slit. By applying the electrostatic fields within in the hemispherical analyzer (HSA), we can allow the electrons of a given energy (Pass Energy) to detector.[7,8]

The conventional x-ray tube consists of Al Kα or Mg Kα anode and thoria-coated Iridium cathode. The cathode can emit electrons upon direct current heating, and anode onto which the emitted electrons are accelerated by applying the certain voltage, it creates the orbital vacancies in Al or Mg atoms. During this process, characteristic orbital energies of x-rays emits from the Al or Mg atoms due to electron relaxation. The x-ray source is covered by housing with a thin aluminium or Si_3N_4 window through which the x-rays can pass onto the surface under analysis. The size of the x-ray spot on the sample depends upon on the size of the cathode electron beam spot on the anode. Therefore, probing area can be controlled by the beam spot size.[8,9] Water cooling is required during the continuous operation of x-rays to avoid the melting of the anode.

Photo ionisation inevitably accompanies with two competitive secondary processes, namely, Auger electron spectroscopy (AES) and x-ray fluorescence spectroscopy (XRF). AES dominates in low energy photo ionisation processes (below 1.4 keV), while XRF dominates at high energies (~10 keV). Since the conventional PES utilize relatively low photon energy, contributions from the fluorescence is negligible. In contrast to that, Auger transitions are commonly appears in XPS.[2]

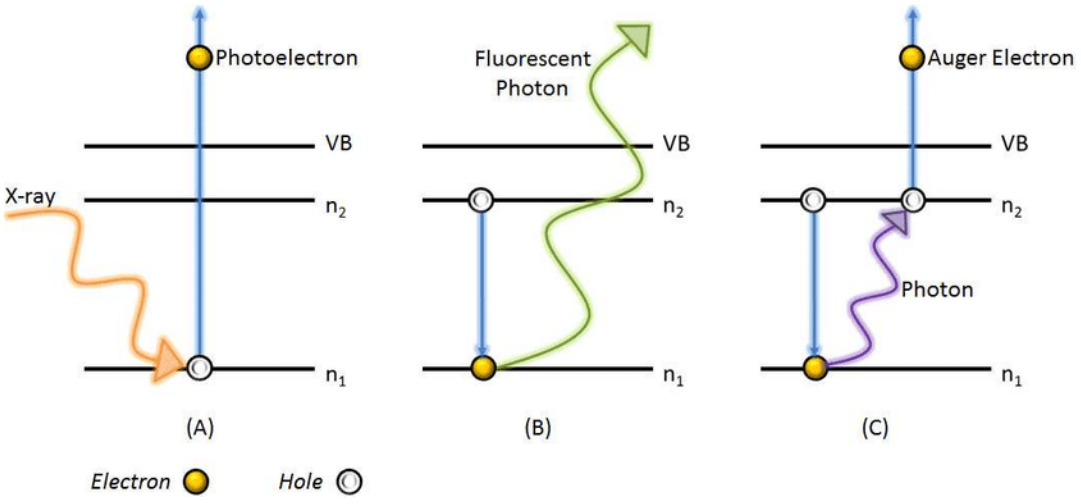

Figure 2.2: Schematic representation of a) Photoelectron spectroscopy b) X-ray absorption spectroscopy (c) The Auger decay electron spectroscopy. From Ref 2; Copyright permission obtained from Thesis.[2]

2.3. Near ambient pressure photo-electron spectroscopy (NAPPES)

To understand the interaction of the catalysts surface with the gaseous molecules, as well as to address the Pressure gap in catalysis and materials science, it is highly desirable that the surface technique which can work even at ambient pressure or close to that. However, surface sensitive techniques such as PES cannot be used at high pressures due to severe attenuation of photoelectrons by gas phase molecules. The attenuation of the photoelectrons follows Beer's law,

$$I = I_0 e(-z\sigma_{K.E} P/kT) \qquad \text{(Eq. 2.6)}$$

I emitted electron intensity detected by analyzer at a given pressure *P*; I_0 emitted electrons intensity detected by analyzer in UHV; z the distance travelled by electrons in gas at pressure *P* and temperature *T* and k is the Boltzmann constant, $\sigma_{K.E}$ the electron scattering cross section (it depends up on the electron K.E and nature of gas).[10] At high pressures, elastically scattered photoelectrons which retain their kinetic energy, but will scatter out of the acceptance cone of the analyzer and/or inelastic scattering caused due to the excitation of gas molecules by vibrational, rotational and electronic states. As a result of inelastic scattered photoelectrons, an increase in the background at lower kinetic energies coupled with reduction of the peak intensity.

The mean free path of electron λ_e depends on energy of the electron and gas pressure *P,* and as the pressure increases the λ_e decreases, and hence, the sample must be placed very close to the analyzer cone aperture. Also, the distance (d) between the solid sample surface and the analyzer cone should be appropriate to maintain the uniform pressure at sample surface. The IMFP of electrons in solid is of the order of few nm, but it is of the order of mm in gas (1 Torr). Moreover, electrons has to travel ~ 1m distance to reach the detector and it requires the use of several efficient differential pumping stages in the electrostatic lens regime and in the electron energy analyzer. By reducing the aperture diameter of the analyzer cone, the differential pumping can be improved**.** Differential pumping stages (Figure 2.3) allow the solid sample to remain in the gaseous environmental pressures, while maximizing the mean free path of emitted electrons, so that they can reach the detector.[7,11] Additionally, by applying voltage to the electrostatic lenses in the unit can accelerate and focus towards electron energy analyzer. The detector is a standard hemispherical electron energy analyzer and must remain in vacuum to function.[12] Optimization of these features of NAPPES allow studying the molecular level solid-gas, solid-liquid interfaces under near ambient conditions.

NAPPES is a interdisciplinary tool as evidenced from a number of research articles over the past decade utilized to unravel different aspects of catalysis, solid-gas interfaces, energy materials, electrochemistry and solid-liquid interfaces.

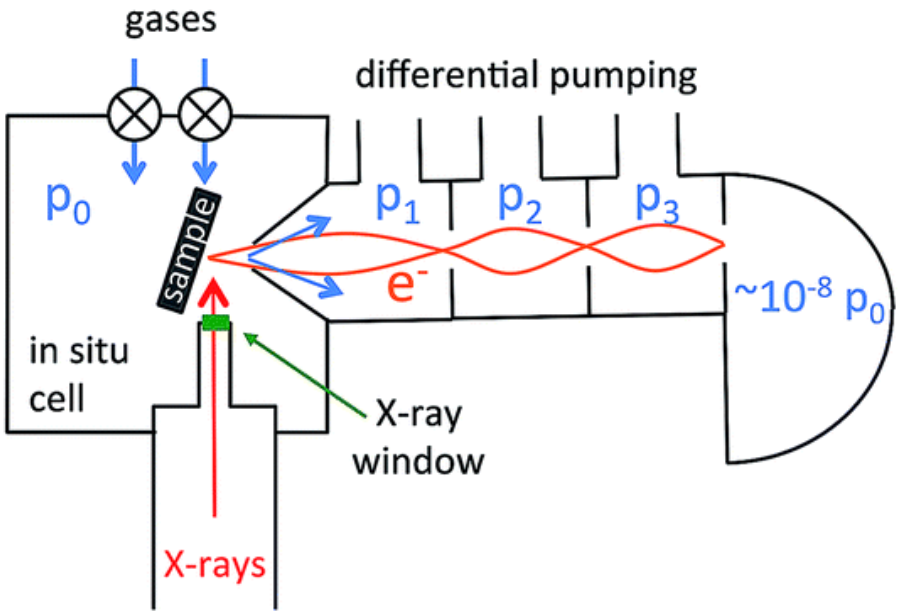

Figure 2.3: Principal layout of the NAPPES. From Ref 7; Copyright permission obtained from RSC.[7]

2.4. Gas-phase photoelectron spectroscopy and work function changes

It is important to understand the gas-phase spectra of reactant molecules that interact with the surface and a brief note is added herewith. Gas phase photoelectron spectroscopy was first described by Kai Siegbahn.[13] NAPUPS of gaseous oxygen and hydrogen molecules recorded at 0.1 mbar partial pressure with He-I (21.2 eV) photons is presented in Figure 2.5. The gas-phase photoelectron spectrum arises due to the electrons ejected from the various electronic states shown in Figure 2.5.

$$E_{BE} = h\vartheta - E_{KE} - \Phi_{analyser} \qquad \text{(Eq. 2.7)}$$

Since solid samples are grounded to the earth, obtained BE referenced to the E_F level. However in the case of gas phase photoelectron spectra, ionisation energy (IE) of the gas molecule is referenced to the vacuum level. Hence,

$$IE_{gas} = BE_{gas} + \Phi_{sample} \qquad \text{(Eq. 2.8)}$$

Kinetic energy of gas phase photoelectron near to the surface of any solid sample

$$KE_{gas} = h\vartheta - BE_{gas} - \Phi_{analyser} = h\vartheta - IE_{gas} + \Phi_{sample} - \Phi_{analyser} \qquad \text{(Eq. 2.9)}$$

For a free gas molecule ionisation energy is always constant, change in the vacuum level of a given gas molecule relative to the fermi level corresponds to change in the work function of any material.[14]

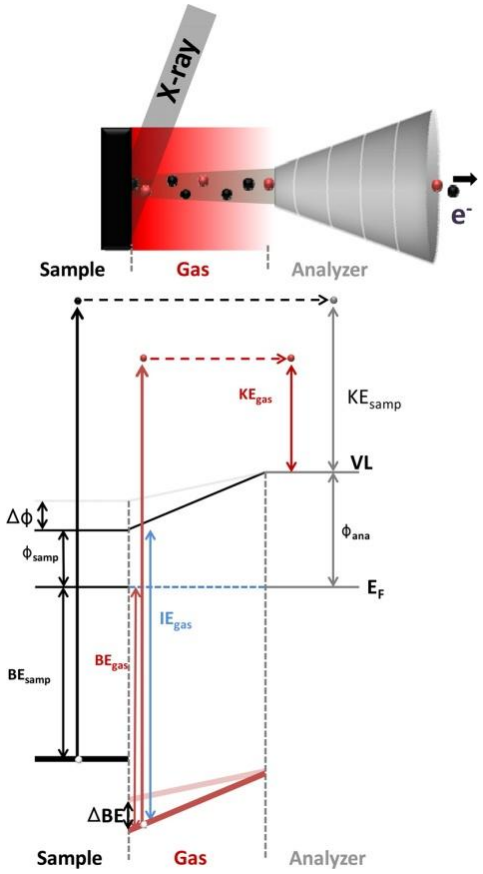

Figure 2.4: The schematic representation with band energy diagram of sample, gas, analyzer and its co-relation with photoelectron process. Relative change between vacuum level and sample fermi level gives the work function change, which can be detected by change in gas phase binding energy. From Ref 14; Copyright permission obtained from ACS.[14]

Excitation of electrons with 21.2 eV photon results in the formation of photoelectron bands with vibration features around the binding energy (BE) of 8.0, 12.5, and 13.5 eV for oxygen and 11.2 eV for hydrogen due to photo excitation of an electron from the valence orbital Π*2p, Π2p, and 3σ of oxygen and the σ1s orbital of hydrogen molecule, respectively.[15] Each group of photoelectron bands consists of closely spaced and well-resolved fine structures due to the formation of M_2^+ with varying degrees of vibrational excitation. At room temperature, most of the M_2 molecules are in their lowest vibrational ground states, v = 0, 1, 2, 3, and higher states are thinly populated. Ionization to M^+ can result

in an ion in any of its possible electronic states, each of which may be in any of their allowed vibrational states v′.

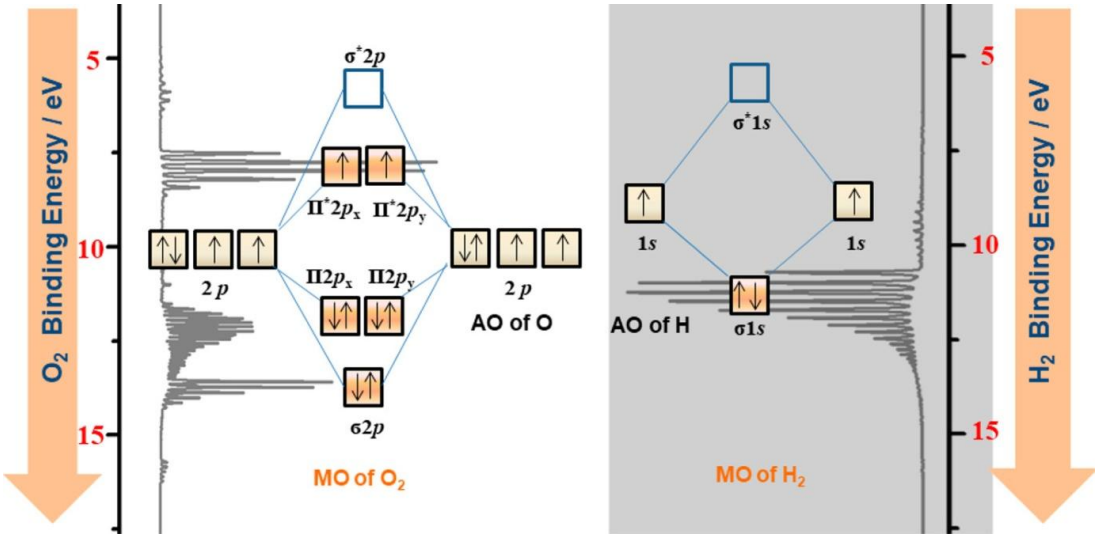

Figure 2.5: Schematic representation of the O_2 and H_2 vibrational features. AO and MO stand for atomic and molecular orbitals.

The resolution of the vibrational features also depends upon the lifetime of molecular ion states or density of the vibrational states; however, the same gas phase spectra are bound to change, when the gas-phase molecules are in adsorption desorption equilibrium with the surface, reaction with surface, simple close proximity to the solid surface and the surface heterogeneity, due to different surface potentials.[16] In fact, this phenomenon is very relevant to any surface dependent physicochemical phenomenon like sensing, adsorption, catalysis, and electrochemistry. On the solid surfaces, these vibrational features in BE may shift due to exertion of a solid surface potential on a gas molecule.

2.5. Near ambient pressure photoelectron spectrometer at CSIR-NCL

To address the nature of surfaces and interfaces and how they behave under reaction measurement conditions, a custom built laboratory based NAPPES (Prevac, Poland) was installed at National Chemical Laboratory, India. Existing unit consist of Load lock, where samples can be introduced and high vacuum is quickly achieved with fast pumping with HiPace300 Pfeiffer turbo molecular pump (TMP-260 l/s) backed by the DUO 10M Pfeiffer double stage rotary vane pump. Preparation chamber equipped with sputter ion gun (IS 40C1, Prevac) and Residual gas analyzer (SRS, RGA200). Sputter ion gun can operate between 0 to 5 kV and 0 to 10 mA with argon gas. Reaction product analysis and vacuum leak test of the

instrument can be carried with RGA. Preparation chamber also consists of 3-axis manipulator with sample heating (950 K) and cooling (120 K, with liquid N_2) setup. In conjunction with preparation chamber, storage unit is attached, where up to 10 samples can be stored; however the pumping system common for the both chambers (355 L/s HiPace300 Pfeiffer TMP, DUO 20M Pfeiffer double stage rotary vane Pump). Analysis chamber equipped with dual anode x-ray source, Monochromator (VG Scienta MX 650 Al-kα), UV source (He-I and He-II), 3 stages of differential pumping system, Flood source (Charge compensator on surface), hemispherical analyzer (VG Scienta R3000HP) and 3-axis manipulator with heating (1025 K) and cooling (100 K, with liquid N_2) setup. All three chambers were separated by manual gate valves and sample transfer can be done with help of manual linear arm and 3-axis manipulator. Additional details about instrument can be found in earlier articles.[12] Analysis chamber may be considered as an open type of reactor, where one can perform various reactions at different temperatures and pressures up to 1 mbar. Different gas ratios can be mixed with mass flow controllers in gas mixing chamber and it can dose into the analysis chamber through fine leak valve. Further, we can heat the gas dozer also up to 825 K. The reaction pressure on sample surface can be measured through CTR gauge. The analysis chamber vacuum can be maintained by various capacities TMP, Rotary vane pumps, Ion pump and Titanium sublimation pump (TSP). The spectrum recording and data analysis is being carried out with SES and CASA software respectively.

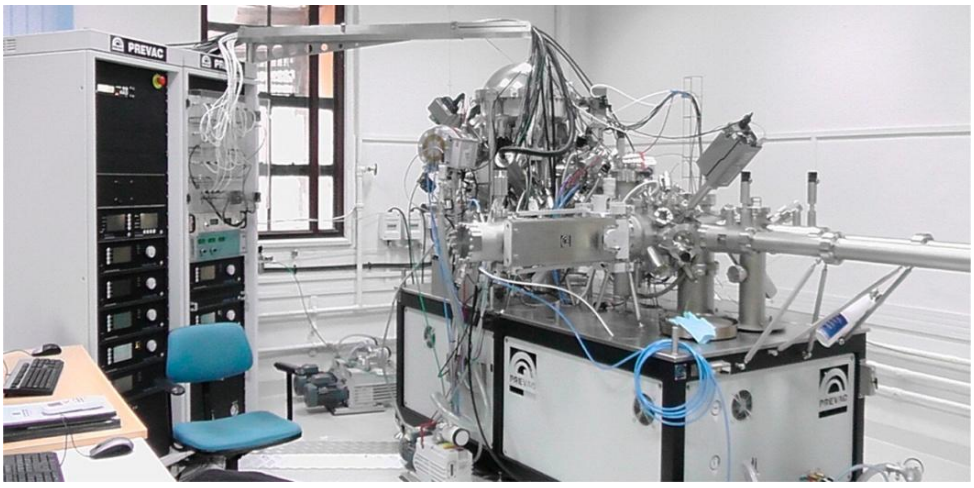

Figure 2.6: A photograph of NAPPES unit at CSIR-NCL.

To understand the interaction of the catalysts surface with the gaseous molecules and to address the pressure gap in catalysis, three main steps were taken during the design and fabrication of NAPPES unit to carry out the experiments at 1 mbar.

1. Sample to analyzer distance
2. Differential pumping setup
3. Aperture free electrostatic lenses.

As mentioned in the earlier section mean free path of electron decreases with increasing pressure. According to literature reports on IMFP calculations for increasing KE of electrons, electrons with 400 eV KE in O_2 gas at 1 mbar pressure can travel up to 4 mm, before it encounters first collision with gas molecules. Hence, to retain the electron count, we maintained 1.5 mm distance between samples to the analyzer cone with an aperture of 1.2 mm. As shown in the Fig. 2.7 electron can enter into the ELR (Electro static lens regime).

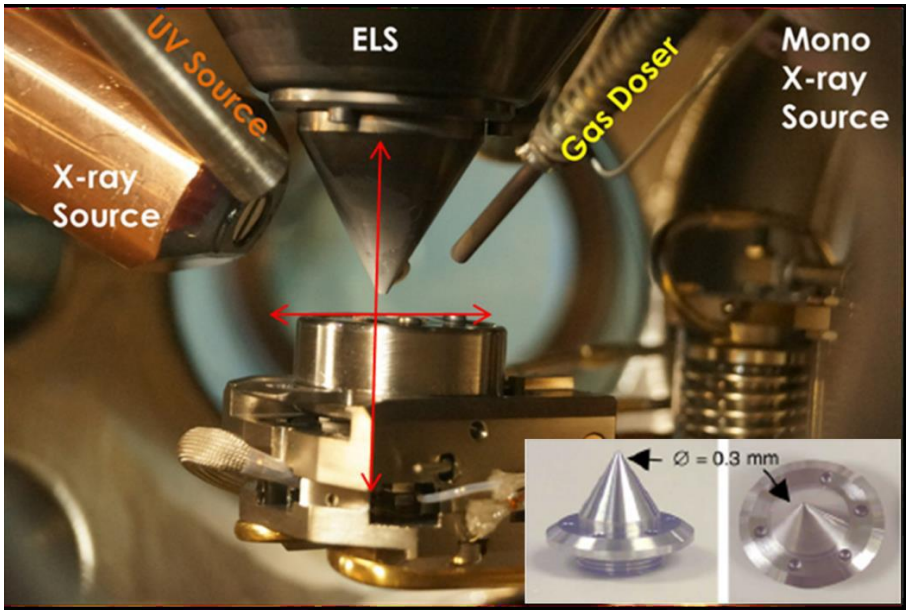

Figure 2.7: Inside view of analysis chamber; Inset picture shows the analyzer cone aperture. Cone with 0.3 mm aperture is shown only for reference.

Second one is the three differentials pumping stages in the analyzer. To extend the mean free path of electron, in ELR region first (400 L/s) and second (300 L/s) pumps were arranged and third one (400L/s) is in Electron energy analyzer (EEA). In addition to that double cone pumping and exchangeable analyzer cone helps in generating steep pressure decrease within small distance (Fig. 2.8b). It has been experimentally observed that, in the NAPPES unit at NCL, at 1 mbar with N_2 gas; 5×10^{-4}, 10^{-6}, and 10^{-7}-10^{-8} mbar could be maintained in the first, second and third differential pumping stages with 0.8 mm diameter analyzer cone.

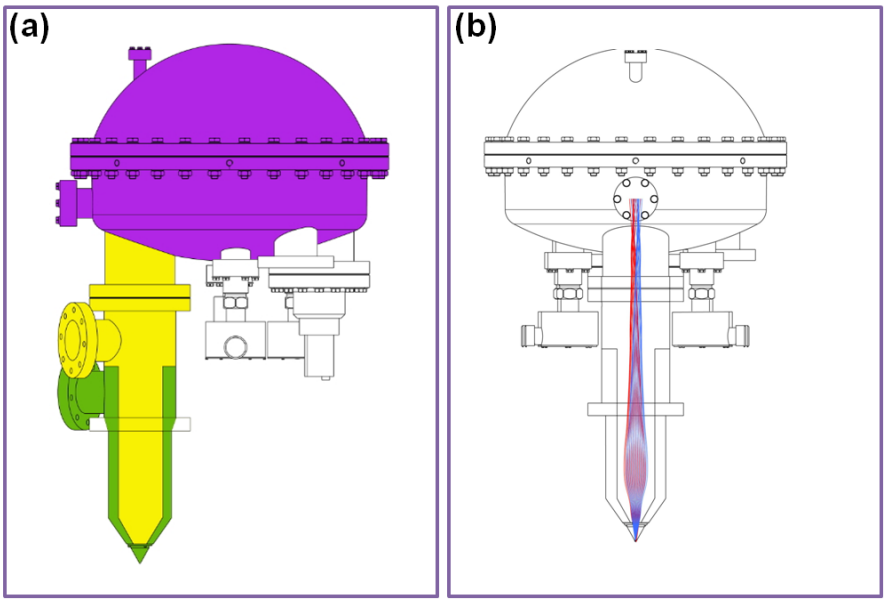

Figure 2.8: Near ambient pressure photoelectron spectrometer (a) A double front cone pumping arrangement, (b) A schematic of the aperture free ELR and the electron trajectory for faster data acquisition.

As shown in Fig. 2.8b aperture free electrostatic lenses with effective R3000HP analyzer design is adopted to minimize the electron loss and electrons convergence achieved by applying voltage. With our current setup at 50 eV pass energy, 1.2 mm aperture diameter, and analyzer slit (0.2 mm) 0.42 ± 0.02 eV resolutions was achieved. However, the resolution decreased to 0.6 ± 0.02 eV with the maximum slit width of 3.0 mm. of the analyzer.

2.6. General experimental conditions for NAPPES measurements

1 M HNO_3 acid-etched cobalt and Mo metal foil was introduced into the NAPPES unit. Co and Mo metal foil was sputter cleaned repeatedly by several cycles of Ar^+ sputtering at a pressure of 5.5×10^{-6} mbar with 4 kV and 7 mA at 500 K followed by annealing under oxygen (1×10^{-6} mbar) at 600 K for 15 min and vacuum annealing at 1000 K for half an hour; this sputter cleaning procedure is continued, until no peaks other than those of Co or Mo metal were detected by XPS. The above sputter cleaning procedure removes the carbon impurities as CO_2, and vacuum annealing cleans any excess surface oxygen from the previous annealing. No common impurities, such as sulphur, silicon, and phosphorus, were detected, or it is lower than the detection limits of the R3000 analyzer. The helium-I ($h\upsilon$ = 21.2 eV) discharge lamp was used to record the valence band at a pass energy of 5 eV. At this photon energy, the PES is highly sensitive to the surface, surface changes, and layer of adsorbates on

the surface than many other techniques, due to a limited probing depth of around 2 nm. Core level and x-ray VB spectra were also recorded using a monochromatic Al Kα radiation source (hν = 1486.6 eV). High pressure experiments were performed in the pressure range from 10^{-6} to 1 mbar with required gases, such as O_2 (99.999%), hydrogen (99.999%), CO_2 (99.999%). An analyzer cone aperture (D) of 1.2 mm was employed at a distance (sample surface to cone aperture) of 1.5 mm; this is to ensure that the applied pressure was fully felt by the surface. Spectra recording and analysis of obtained data was carried out with SES and CASA software's respectively. In contrast to closed reactor cell, analysis chamber employed with open type reactor design, where high pressure gas doser extends right up to the sample surface. Reactor pressure measurements were made very close to the surface to ensure the pressure values reported are highly reliable.

2.7. Synthesis of molybdenum carbide

Mo_2C powder catalyst was prepared by direct carbonisation of the precursor (ammonium heptamolybdate (AHM)) procured from Thomas Baker. Initially AHM was placed into a quartz tubular reactor in a ceramic boat and then heated to 773 K at 5 K/min, subsequently temperature was increased from 773 to 973 K at a rate of 2 K/min and held at 973 K for 5 h in CH_4/ H_2 (1/3) environment. The resulting material was cooled down to room temperature in the same environment and used for the CO_2 hydrogenation reaction and characterisation studies.

2.8. Ex-situ characterisations

2.8.1. X-ray diffraction

XRD is one of the most common non-destructive analytical techniques used in catalyst characterization. It is a primary and very important techniques used for phase identification, crystal structure, inter planar distance, and crystallite size and crystallite purity of any crystalline materials. Smallest repetitive unit in the lattice is called unit cell. It describes the arrangement of atoms and geometry of the crystal. Since wavelength of x-ray used in this technique, (for eg. 1.54 Å (Cu Kα)), is comparable to size of the atoms in the lattice, hence x-ray can penetrate in to the solids and well suited for probing the arrangement of atoms in the bulk.[17] When x-ray is incident on crystalline solid material, it may coherently scattered or in-coherently absorbed. The coherently scattered waves interfere with each other

either constructively and destructively give bright and dark fringes respectively. However, constructive interference forms when x-rays scatter in a particular angle and path difference should be integral number of wavelength. These phenomena called as x-ray diffraction. Bragg's equation relates electromagnetic ray's wavelength, diffraction angle and lattice spacing.[18]

$$n\lambda = 2dsin\theta \qquad \text{(Eq. 2.10)}$$

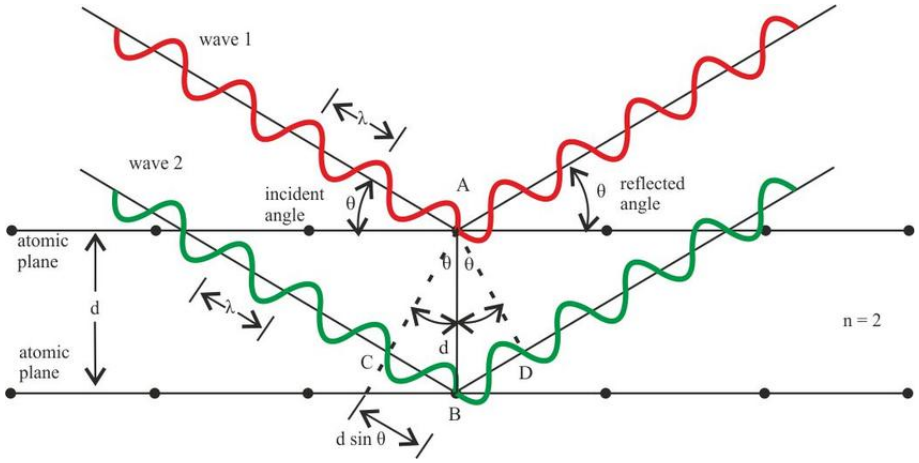

Figure 2.9: Schematic representation of the diffraction of x-ray in crystalline materials. From Ref 18; Copyright permission obtained from AAPT.[18]

Where, θ is the Bragg's angle, x-rays wavelength is λ; d is inter planer distance and n is the order of diffraction. Analysis of the various solids through different 2θ angles (0-90) gives different diffraction pattern from lattices, due to random orientations of crystallites in a particle. Since any material has its unique d-spacing value, using Bragg's equation d-values can be calculated; comparison with reference pattern (JCPDS) can identify the material structure. Full width half maximum (FWHM) of diffraction peak in diffraction pattern describes the dimensions of reflecting planes. By using Scherer formula one can calculate the average crystallite size of any nano materials.

$$t = 0.9\lambda/\beta cos\theta \qquad \text{(Eq. 2.11)}$$

Where t is thickness of the crystal, θ is angle between incident rays and lattice plane and β is obtained from warren formula, $\beta = \beta^2_M - \beta^2_S$, Where β is FWHM difference between materials and standard sample (silicon). In the present study, XRD of as synthesized powder Mo_2C, Mo foil and Co and its oxides were carried out using a PANalytical X'pert Pro dual goniometer diffractometer equipped with a Cu Kα (1.5418 Å) radiation.

2.8.2. Raman spectroscopy

Vibrational spectroscopy is a non-destructive and fastest technique used to measure the unique fingerprint vibrational modes of any molecules. Among those techniques, Raman spectroscopy is a promising technique, can provides chemical structure, nature of bonds in a molecule. The interaction of photon with molecules leads two types of scattering. First one is elastic scattering and next is inelastic scattering. In elastic scattering, no changes in the photon energy occur (also called as Rayleigh scattering). In contrast to elastic scattering, there occurs change in the photon frequency of scattered light from the incident photon due to interaction with molecular vibrations that leads to excitation/deactivation (exchange of energy) of molecular vibrations. In inelastic scattering, if scattered photon gains energy, net frequency of scattered light (E = Eo + Ev) is higher than the incident light, process know as anti-stokes Raman scattering. Instead, if loses its energy due to the interaction, net frequency change will be lower than the incident photon energy (E = Eo − Ev) and this process known as Stokes Raman scattering. For the first time in 1928, Chandrashekhara Venkata Raman an Indian scientist associated with his student K. S Krishnan observed the inelastic scattering of light in organic liquids, later known as Raman Effect. Raman Effect explains about inelastic scattering in the small fraction of light, which reflected from the surface.[19] In Raman spectroscopy, utilizing scattered light can give direct results of the analysis without sample preparation and easy interpretation of the results making it as a time saving and cost effective technique. Raman spectra of powder Mo_2C samples and Co_3O_4 recorded on a Horiba JY lab RAM HR 800 spectrometer coupled with a microscope in reflectance mode with a 488 nm laser source.

2.8.3. Scanning electron microscope

In a sufficient light, a human eye can resolve the image up to 0.2 mm within optimum distance. A light microscope has a maximum resolution 1000x times to human eye. White light has the average wavelength of 550 nm which results in a theoretical limit of resolution of the light microscope to be about 200-250 nm. The resolving power of the light microscope was not only depends upon the quality and number of the lenses but also depends on the wavelength of the photon. To overcome this limitation, electrons were used over white light due to electron have much shorter wavelengths, in order that we can get better resolution.[20] There are two types of electron microscope uses for material characterisation.1) Transmission electron microscopy (TEM), 2) Scanning electron microscopy (SEM).

Scanning electron microscopy (SEM) is a microscopy technique widely used for morphological studies. SEM scans the surface of solid with highly energetic focused e^- beam to create an image. These interactions give the information about morphology, chemical compositions. Tungsten or lanthanum hexa boride (LaB6) generates the electron source and its passes through the combination of lenses and apertures to focus the electron beam on the sample surface under UHV conditions. Depending upon the accelerating voltage of electrons and density of sample, it penetrates few microns depth into the sample and yields secondary electrons, back scattered electrons (reflected), transmitted electrons and characteristic x-rays. Secondary electron emission from the near to the surface atoms and it will be detected to produce high resolution images. Contrast is generally caused by the orientation of the sample towards detector. Parts of the surface facing the detector appear brighter than the surface pointing away from the detector. When an electron from the beam encounters a nucleus in the sample, the resultant columbic attraction leads to a deflection in the electron's path, known as Rutherford elastic scattering. A fraction of these electrons will be completely backscattered, re-emerging from the incident surface of the sample. Since the scattering angle depends on the atomic number of the nucleus, the primary electrons arriving at a given detector position can be used to produce images containing topological and compositional information. Energy of the characteristic x-rays can be measured by Energy dispersive x-ray spectroscopy (EDX analysis). EDX analysis helps in the qualitative and quantitative analysis of elements presents in the sample.[21] SEM samples were prepared by dispersing in isopropanol (IPA) by ultra sonication for 30 min. After proper dispersion, drop casted on silicon wafer, allowed for drying at room temperature for 12 h and subjected to analysis. The images were recorded using an ESEM Quanta-200 3D instrument operating at 20 kV. The chemical composition of the catalysts was also estimated from SEMEDAX by probing the samples at different random places.

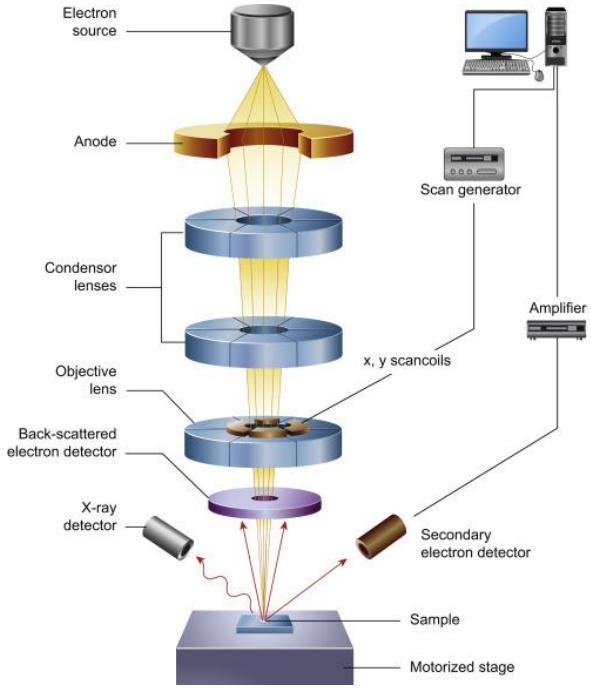

Figure 2.10: Graphical representation of scanning electron microscopy. From Ref 20; Copyright permission obtained from book.[20]

2.8.4. Temperature-programmed desorption

Temperature programmed desorption (TPD) also known as temperature desorption spectroscopy (TDS) is the method to quantify the basic/acidic sites on the solid surface by desorbing CO_2/NH_3 as a probe molecule with temperature. Since solid surfaces (adsorbent) always have a vacant coordinate site to minimize its surface energy by making a bond with incoming reactants (adsorbate). This bond energy depends upon the combination of materials and reactants. Once the surface is ramped, at certain temperature energy transferred to reactants and causes desorption and this particular temperature is known as desorption temperature. Based on desorption temperature one can estimate the types surface nature (acidic/basic), strength and quantity of surface nature.

In the present work, TPD measurements were carried out with CO_2 on a Micromeritics Auto Chem 2910 instrument. Initially, as synthesized catalyst was pre-treated in He (30 mL/min) at 473 K for 1 h. It was then cooled to 373 K and a mixture of CO_2 in He (10 vol%) was fed to the sample (30 ml/min) for 1 h. Then, the sample was flushed with He (30 ml/min) for 1 h at 373 K. CO_2-TPD measurements were made in the temperature range of 373-973 K at a heating rate of 10 K/min.

2.8.5. Temperature programmed reduction

Temperature-programmed reduction (TPR) is a physical technique widely used in heterogeneous catalysis for characterisation of metal oxides, metal carbides, metal supported on oxides. It gives the quantitative information about the reducibility of those materials and the heterogeneity of the reducible surface. In this method reducing gas (usually H_2/CO) diluted with Argon flows over the sample. Due to changes in the quantity of reducing gas gives the changes in thermal conductivity and it will be detected by thermal conductivity detector (TCD).

H_2-temperature programmed reduction (H_2-TPR) experiments were carried out using a Micromeritics Autochem 2920 system, equipped with a TCD detector. Initially, as synthesized catalyst was heated to 573 K in He gas (30 ml/min) at a ramping rate of 5 K/ min.; the sample was held at 30 min at 573 K, and then cooled to 325 K. Subsequently, gas station was changed to 10 % H_2 in Ar gas (30 ml/min) and the catalyst was heated to 1173 K (5 K/ min) and H_2 consumption was detected by TCD detector.

2.9. Reaction experiments

The RWGS activity was evaluated at atmospheric pressure using a fixed bed down flow SS316 reactor of 11 mm ID, with a Cr-Al thermocouple placed at the centre of the catalyst bed. About 0.5 cm^3 of the catalyst in the particle size range of 35–50 mesh diluted with an equal volume of alumina pieces in the same size range was loaded in the uniform heating zone of tubular reactor. Prior to the reaction, the catalyst was pre-treated in 20 vol % CH_4 in H_2 at 473 K for 2 h @ 2 K/min. After reduction for 2 h, the temperature was set to the desired reaction temperature. CO_2:H_2 gas mixture was fed to the reactor using two mass flow controllers. The product gas mixture obtained following the reaction was cooled using a chilled water condenser and the dry gas was analyzed using online GC (Chemito-1000) equipped with TCD and a spherocarb column (1/8” id, 8 ft length). A calibrated gas mixture was used for the identification of the gas components and their quantification.

2.10. References

(1) Siegbahn, K. *J. Electron Spectrosc. Relat. Phenom.* **1974**, *5*, 3-97.

(2) Hieulle, J., École Polytechnique, 2014.

(3) Shirley, D. A. *Phys. Rev. B* **1972**, *5*, 4709-4714.

(4) Van den Berg, J. *Surf. Interface Anal.* **1993**, *20*, 1081-1082.

(5) Langell, M.; Anderson, M.; Carson, G.; Peng, L.; Smith, S. *Phys. Rev. B* **1999**, *59*, 4791.

(6) Ghosalya, M. K.; Reddy, K. P.; Jain, R.; Roy, K.; Gopinath, C. S. *J. Chem. Sci.* **2018**, *130*, 30.

(7) Karslıoğlu, O.; Nemšák, S.; Zegkinoglou, I.; Shavorskiy, A.; Hartl, M.; Salmassi, F.; Gullikson, E. M.; Ng, M. L.; Rameshan, C.; Rude, B.; Bianculli, D.; Cordones, A. A.; Axnanda, S.; Crumlin, E. J.; Ross, P. N.; Schneider, C. M.; Hussain, Z.; Liu, Z.; Fadley, C. S.; Bluhm, H. *Faraday Discus.* **2015**, *180*, 35-53.

(8) Newberg, J. T.; Åhlund, J.; Arble, C.; Goodwin, C.; Khalifa, Y.; Broderick, A. *Rev. Sci. Instrum.* **2015**, *86*, 085113.

(9) Starr, D. E.; Liu, Z.; Hävecker, M.; Knop-Gericke, A.; Bluhm, H. *Chem. Soc. Rev.* **2013**, *42*, 5833-5857.

(10) Frank Ogletree, D.; Bluhm, H.; Hebenstreit, E. D.; Salmeron, M. *Nuclear Instruments and Methods in Physics Research Section A: Accelerators, Spectrometers, Detectors and Associated Equipment* **2009**, *601*, 151-160.

(11) Ogletree, D. F.; Bluhm, H.; Lebedev, G.; Fadley, C. S.; Hussain, Z.; Salmeron, M. *Rev. Sci. Instrum.* **2002**, *73*, 3872-3877.

(12) Roy, K.; Vinod, C.; Gopinath, C. S. *J. Phys. Chem. C* **2013**, *117*, 4717-4726.

(13) Gelius, U.; Siegbahn, K. *Faraday Discus. Chem. Soc.*, **1972**, *54*, 257-268.

(14) Axnanda, S.; Scheele, M.; Crumlin, E.; Mao, B.; Chang, R.; Rani, S.; Faiz, M.; Wang, S.; Alivisatos, A. P.; Liu, Z. *Nano Lett.* **2013**, *13*, 6176-6182.

(15) Rabalais, J. W. *Principles of ultraviolet photoelectron spectroscopy*; Wiley, New york, **1977**.

(16) Ghosalya, M. K.; Jain, R.; Reddy, K. P.; Gopinath, C. S. *J. Phys. Chem. C* **2018**, *122*, 4331-4338.

(17) Post, B. *X-Ray Spectrometry* **1975**, *4*, A17-A22.

(18) Cullity, B. D. *Am. J. Phys.* **1957**, *25*, 394-395.

(19) Raman, C. V.; Krishnan, K. S. *Nature* **1928**, *121*, 501.

(20) Inkson, B. J. In *Materials Characterization Using Nondestructive Evaluation (NDE) Methods*; Hübschen, G., Altpeter, I., Tschuncky, R., Herrmann, H.-G., Eds.; Woodhead Publishing: **2016**, 17-43.

(21) Abd Mutalib, M.; Rahman, M. A.; Othman, M. H. D.; Ismail, A. F.; Jaafar, J. In *Membrane Characterization*; Hilal, N., Ismail, A. F., Matsuura, T., Oatley-Radcliffe, D., Eds.; Elsevier: **2017**, 161.

Chapter-3

Metallic Cobalt to Spinel Co_3O_4-Electronic Structure Evolution by Near-Ambient Pressure Photoelectron Spectroscopy

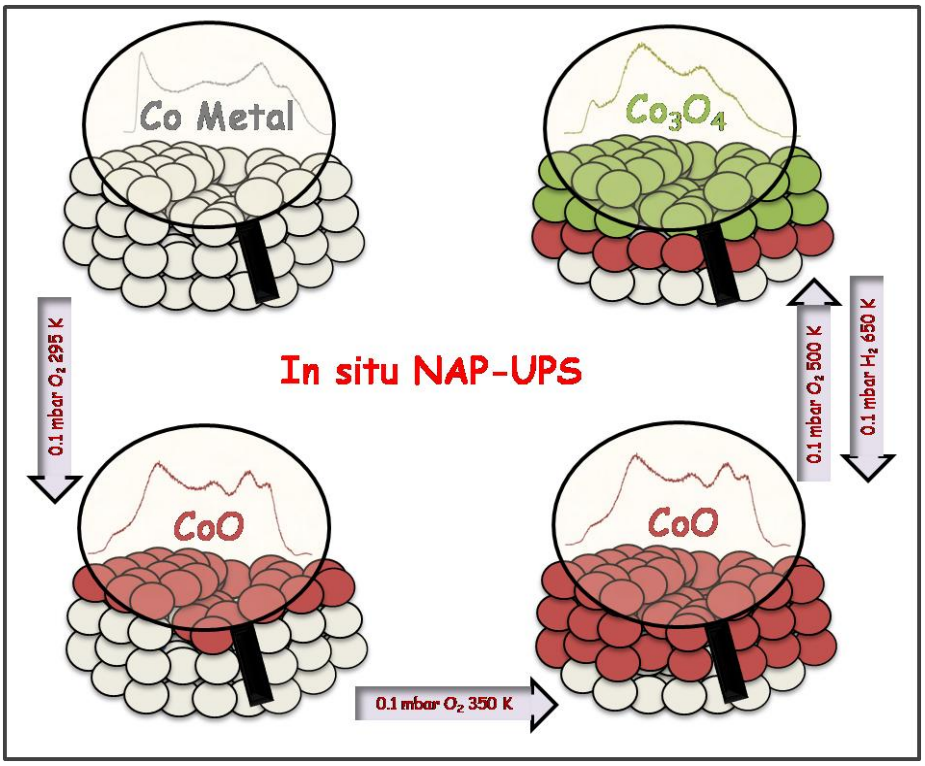

Part of chapter 3 has been published and the details are [1]

[1]Reddy, K. P.; Jain, R.; Ghosalya, M. K.; Gopinath, C. S.; Metallic Cobalt to Spinel Co_3O_4-Electronic Structure Evolution by Near-Ambient Pressure Photoelectron Spectroscopy. *J. Phys. Chem. C.* **2017**, *121*, 21472-21481.

3.1. Introduction

The first-row 3*d* transitional metals in the periodic table and corresponding oxides form an important class of materials with diverse structures and applications. These materials exhibit many interesting physical and chemical properties and it depend on the electronic structures and oxidation states of constituent elements. Among those materials, cobalt and its oxides, cobalt monoxide (also known as rock salt CoO), and tricobalt tetra oxide (also spinel Co_3O_4) have attracted renewed attention due to remarkable electronic, magnetic, optical, and chemical properties.[1,2] These oxides have close thermodynamic stabilities, which can be inter-converted by varying the oxidation and reduction conditions. These materials have been used in magnetic applications,[3] anode material as in Li-ion batteries, gas sensors,[4] catalysis for energy/fuel, and environment-related applications.[5-7] Cobalt oxides have been attempted often to replace noble metals in these catalysis applications with limited success; indeed this aspect makes them worth investigating further. The superior activity of spinel Co_3O_4 in the CO and methane oxidation is due to the abundance of Co^{3+} ions in the spinel structure.[7] The oxidation states of Co in CoO and Co_3O_4 are very sensitive to the nature of the reaction medium, temperature and pressure. The electronic structure and reducibility/oxidizability of these oxides are the critical factors in determining the physical and chemical properties, such as magnetism, sensors, catalysis.[8-10] Therefore the basic understanding of the reduction of Co_3O_4, oxidation of CoO to spinel and any intermediate species is likely to be helpful in the development of better materials with improved properties.

Catalysis aspects/results are often fully not reproducible due to various reasons; difficulty in maintaining a same or similar electronic structure and surface chemical composition are the prime reasons. A minor change in the reaction condition or different catalyst preparation methods lead to a different set of results in catalysis, often due to changes in electronic and structural factors.[11-14] Surface electronic structure plays a dominant role in catalysis and how it changes as a function of reaction parameters is hardly studied by valence band (VB) photoelectron spectroscopy (PES) with low energy photons. VB changes of catalysts with ultraviolet PES at different reaction conditions is of paramount importance, as it explores only the surface changes (~2 nm), which decides the catalysis or any surface dependent physical and chemical properties. Some of the important parameters, such as fermi level (E_F) changes and work function (ϕ), can be determined in the presence of pressure and temperature by near-ambient pressure ultra violet photoelectron spectroscopy (NAPUPS).[8,15]

The changes observed with He-I excitation is not possible to detect with Al Kα , due to (a) about three fold higher σ of Co 3*d* (4.356 with 21.2 eV; 0.0037 Mb with Al Kα photons) and O 2*p* (10.67 with 21.2 eV; 0.00024 Mb with Al Kα photons),[16] (b) low resolution of x-ray, and (c) comparatively high probing depth. Additionally, gas phase vibrational features of oxidant or reductant gas can give information about the ϕ changes and it overcomes the limitations of the conventional ϕ measurement methods.[17]

Although studies on the oxidation of Co gave the valuable information on the growth of bulk phase and kinetics of cobalt oxidation,[18] however, the surface electronic structure evolution of cobalt is yet to be dealt by surface sensitive techniques, such as UVPES.[19-21] From the fundamental point of view, a detailed understanding of the transition between the metallic and the oxide phases is far from being conclusively achieved. Indeed such cases are common in Co-based nanomaterials and under heterogeneous catalysis conditions and it are critical to understand the same for further development. Being a highly pyrophoric element, it is even more important to understand the oxidation of Co-surfaces. As testified by large number of theoretical studies, aiming to rationalize the subtle atomistic mechanism at work during the early stages of surface oxidation is important.[22] In the present report, an attempt has been made to explore the electronic structure evolution of metallic cobalt to CoO and then to spinel cobalt oxide in the presence of O_2 atmosphere and high temperatures. Reduction of later spinel to CoO in the H_2 atmosphere was also studied at high temperatures.

Studies on single crystal and polycrystalline cobalt indicated that dissociative adsorption of oxygen begins at 120 K, followed by diffusion into the lattice, leads to the formation of oxides.[23-25] Based on the oxygen pressure and temperature, Co initially oxidises to CoO and subsequently to Co_3O_4 at significantly higher temperatures and/or pressures. The gas-solid (O_2-Co) interaction of cobalt oxide surfaces were addressed with NAPXPS core level spectroscopy at 0.2 mbar O_2 pressure and temperature of 520 K.[26,27] However, no attention has been dedicated to the electronic structure evolution through VB, as it formed by the hybridization of Co 3*d* and O 2*p* ligand orbitals which directly influences various application aspects.[28]

Herein, a combination of NAPUPS and XPS has been exploited to explore the changes in the valence band electronic structure and ϕ changes of Co and CoO_x surfaces under O_2 (oxidising) and H_2 (reducing) atmospheres around mbar pressure regime and elevated temperatures. We address the fundamental issues concerning the various stages of oxidation

of Co metal to Co_3O_4 via CoO. Significant changes in Co 3*d* and 2*p* levels were observed, while O 2*p* observed at a fairly constant energy.

3.2. Results and discussions

3.2.1. Co + O_2 Interaction: pressure and temperature dependent NAP-UPS studies

VB spectra of the Co surfaces were recorded as a function of oxygen partial pressure and temperature, and the representative results are shown in Figure 3.1. The clean cobalt surfaces show typical 3*d* VB features between 0 and 2 eV binding energy (BE) with high-intensity fermi level (E_F) features at 0 eV. A broad and low intensity feature observed at 5.5 eV is attributed to the defects due to the polycrystalline nature of Co surface. O 1s core level analysis rules out the possibility of any surface contamination by oxygen (vide infra, Fig. 3.2b). Oxygen pressure was increased gradually from 10^{-6} to 0.1 mbar through several stages at room temperature (RT; 295 K) and representative results are shown in Fig. 3.1. Even at an oxygen partial pressure of 1×10^{-6} mbar, many significant changes are observed: At least an order of magnitude reduction in E_F intensity was observed. Similar studies on copper surfaces at 0.3 mbar O_2 at RT retains E_F and VB features intensity largely, except the disappearance of Cu 3d fine structure;[29,30] this demonstrates the highly pyrophoric or exothermic oxidizing nature of Co-surfaces. A new and broad VB feature develops around 1.5-2 eV. A significant sharpening of the features at 5.3 and 10.5 eV was observed.

On further increasing the O_2 partial pressure from 10^{-5} mbar and above to 0.01 mbar at 295 K, a metallic feature of Co-surface vanished completely and no significant E_F feature was observed. Both high BE features shift marginally to 5.2 and 10.3 eV, compared to the spectra recorded at 10^{-6} mbar O_2. Both the above features are attributed to oxygen 2p derived states and indicating the growth of oxide layer at the expense of Co-metal. Molecular oxygen (or any gas-phase) vibrational features begin to appear at a partial pressure of about 0.01 mbar and above between 7 and 8 eV. No gas-phase features were observed at pressures lower than 0.01 mbar. Nonetheless, compared to the reference gas-phase O_2 spectra (Fig. 3.1c), 0.5 eV shift to lower BE was observed at 0.01 mbar (Fig. 3.1c). This shift is attributed to the surface potential exerted by cobalt oxide surface layers. In contrast to the sharp vibration features of reference spectrum, broad vibrational features observed on Co-surfaces indicating a possible heterogeneous surface character with different Co-species, such as Co_xO_y (x = 1-2; y = 1-3).

A further increase in O_2 partial pressure to 0.1 mbar at 295 K displays a complete oxidation of the Co-surfaces with no metallic character. This underscores the propagation of oxidation to few atomic layers (up to 2 nm) of Co surface to CoO, which is beyond the detection limit of UVPES (but observed in core level XPS in Fig. 3.2a). However, the

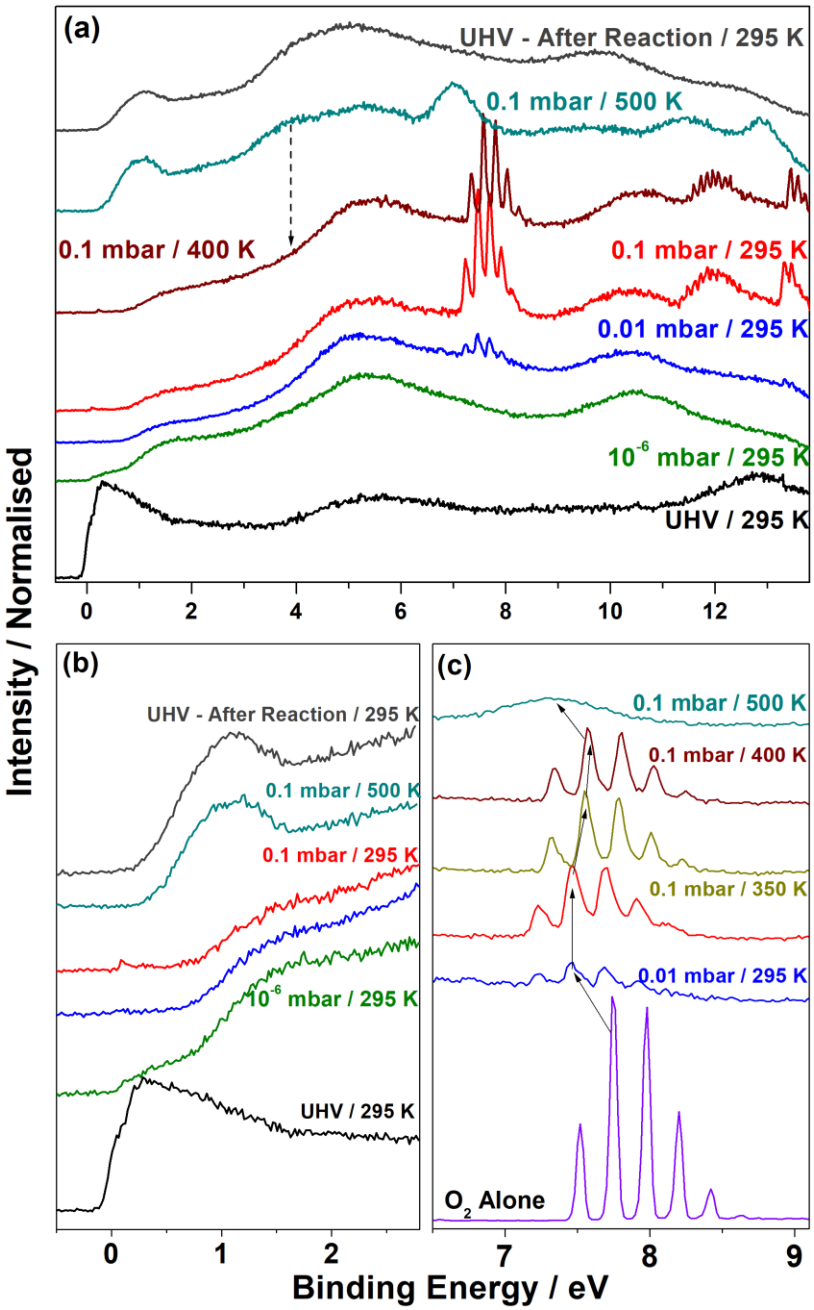

Figure 3.1: (a) NAP-UPS studies on Co metal oxidation in the presence of increasing O_2 partial pressures to Co_3O_4. Changes in (b) Fermi level features and (c) O_2 vibrational features are shown on an expanded scale. Same color codes are followed in all panels.

features observed at 1.5, 5.2 and 10.3 eV in the VB spectrum is retained, as in the spectrum obtained at 0.01 mbar. The first feature at 1.5 eV is attributed to the $3d^7\underline{L}$ final state of CoO; $\underline{L}$ indicates the charge transfer from oxygen ligand to Co.[31] Vibrational features are observed with high intensity due to the high partial pressure of O_2. Unlike the sharp reference gas-phase O_2 features, relatively broadened features underscoring a significantly heterogeneous nature of the surface, due to the Co_xO_y formation. Further increase in O_2 partial pressure up to 0.4 mbar at 295 K, does not show any significant changes (data not shown). No surface features could be observed in NAPUPS at pressures higher than 0.4 mbar. On increasing the temperature to 350 and 400 K at 0.1 mbar O_2 partial pressure, VB features are largely retained as that of at 295 K. O_2 vibrational features are resolved better and shows a shift to higher BE by 0.1 eV at 350 K; at 400 K, a further marginal shift in O_2 vibrational feature was observed. A careful analysis of spectrum recorded at 400 K-0.1 mbar reveals a low intensity and broad hump at 3.8 eV. A good correlation was observed between the present results recorded at 350-400 K and 0.1 mbar partial pressure of O_2 to that of CoO VB spectrum reported in the literature.[32]

On increasing the temperature to 500 K at 0.1 mbar O_2, the most dramatic changes in the VB spectrum was observed with an appearance of a new sharp feature at 1 eV at the expense of $3d^7\underline{L}$ feature of CoO at 1.5 eV. This is attributed to the characteristic and typical feature of the $3d^6\underline{L}$ final state of Co^{3+}.[31,33] Additional states from Co^{2+} form a band that appears to overlap with an O 2*p* band. The peak at 3.8 eV grew in intensity at 500 K and overlaps with O 2*p* band (indicated by dashed arrow). This indicates the onset of oxidation of CoO to Co_3O_4 at 400 K and 0.1 mbar. Brundle et al.[23] observed the x-ray VB maxima of Co_3O_4 at ~1 eV and it is assigned to 3*d* t_{2g} orbitals of Co^{3+} and another broad peak at ~2–4 eV corresponds to t_2 orbital of Co^{2+} 3*d*. Sawatzky et al[33] investigated the VB features of polycrystalline $LiCoO_2$ and observed a sharp VB maxima at ~1 eV that corresponds to Co^{3+} in the low spin state with short Co-O bond distance.

Present results show the satellite peak with low intensity observed at ~9.6 eV due to the low probability of $3d^5$ final state and a similar conclusion was arrived by Langell et al.[31] Indeed, $3d^6\underline{L}$ final state peak was observed prominently. From this observation, it is clear that Co_3O_4 exhibit charge transfer characteristics, like CoO, in 3*d* band structure. Spinel cobalt oxide exhibited VB maxima along with a shoulder at low BE in the spectra recorded with Al K-alpha (Figure 3.10). This is in good agreement with literature reports.[23]

Vibrational features of O_2 was shifted as well as broadened enormously and it appears as a single broad band at 7 eV at 500 K and 0.1 mbar. Compared to the well resolved vibrational feature at 400 K and 7.6 eV (for second or high-intensity feature), 0.6 eV low BE shift was observed with O_2 on Co_3O_4 (at 500 K); this strongly indicates a change in the ϕ of the surface. Indeed, high BE vibrational features (12 eV) also show an exactly similar shift. Broadening observed could indicate a possibility of surface heterogeneity at micro structural level with sufficiently bigger patches of different islands. However, careful in-situ microscopy studies could throw more light on this aspect. After the oxygen treatment at 0.1 mbar at 500 K, the Co-oxide surface was allowed to cool to 295 K and oxygen was evacuated simultaneously. VB spectrum recorded after the evacuation at UHV was as that of observed at 0.1 mbar at 500 K, indicating the stability of the oxidized surface. The CoO $3d^6$ satellite features at 10.5 eV abruptly changed during the oxidation of CoO into Co_3O_4. Initially, the $3d^6$ satellite features appeared at the BE 10.3 eV with high intensity up to 400 K, has changed into low-intensity feature and BE shifted to 9.6 eV.

3.2.2. Co + O_2 Interaction: pressure and temperature dependent NAP-XPS studies

Core level XPS data was recorded along with NAP-UPS measurements at different partial pressures of O_2 and the representative results are given in Fig. 3.2a and 3.2b for Co 2*p* and O 1*s* core levels, respectively. Basically, it supports the conclusions arrived from the VB analysis shown in Fig. 3.1. Clean Co-metal surface shows narrow Co $2p_{3/2}$ feature at 777.8 eV with 15 eV spin-orbit energy gap. This also testifies the surface cleanliness. 0.1 mbar O_2 partial pressure at 295 K dramatically changed the Co 2*p* spectrum to show Co^{2+} feature with the satellite at high BE (784-788 eV), along with metallic Co-feature. It is to be noted that, under the same experimental conditions (at $\geq 10^{-5}$ mbar), while VB features recorded with NAP-UPS (Fig. 3.1a) do not show any E_F at 0 eV, metallic Co 2*p* feature observed in XPS is entirely due to the high probing depth of up to 6-7 nm and high kinetic energy electrons. The satellite and broad main peak in Co 2*p* core levels are indicative of a paramagnetic high spin Co^{2+}, as the unpaired electrons in the *d* shell of the cobalt give rise to excitation (causing the satellite peak) and multiplet splitting of the main peak.[34] On 0.1 mbar O_2 treatment up to 400 K, high-intensity satellite peak and marginally broadened main peak was observed in the XPS spectrum of Co 2*p* core level; they are indicative of paramagnetic nature of CoO. A careful look at the data reveals the presence of metallic Co at 778 eV. Although surface layers are oxidized, 0.1 mbar O_2 pressure and 400 K is not sufficient to oxidize the bulk Co to CoO.

However, on increasing the temperature to 500 K at 0.1 mbar O_2, Co 2*p* spectrum changed considerably and with a marginal metallic Co 2*p* feature at 778 eV; this underscores the propagation of oxidation just extended up to the XPS probing depth (7 nm) under the measurement conditions. Main line intensity at 780 eV increased at the expense of satellite features. Satellite features intensity decreased further on prolonged exposure and a weak satellite feature observed indicating the conversion of spinel Co_3O_4.

O 1*s* core-level spectra recorded is shown in Fig. 3.2b. No O 1*s* feature was observed on clean Co metal indicating the purity of the surface. Oxygen pressure was increased slowly from 10^{-6} mbar pressure to 0.1 mbar. Even at an oxygen pressure of 10^{-6} mbar, significant O 1s peak observed at 529.3 eV and its intensity increased with further increasing of O_2 pressure. Up on O_2 exposure at 0.1 mbar and any temperatures, a high- intensity O 1*s* peak

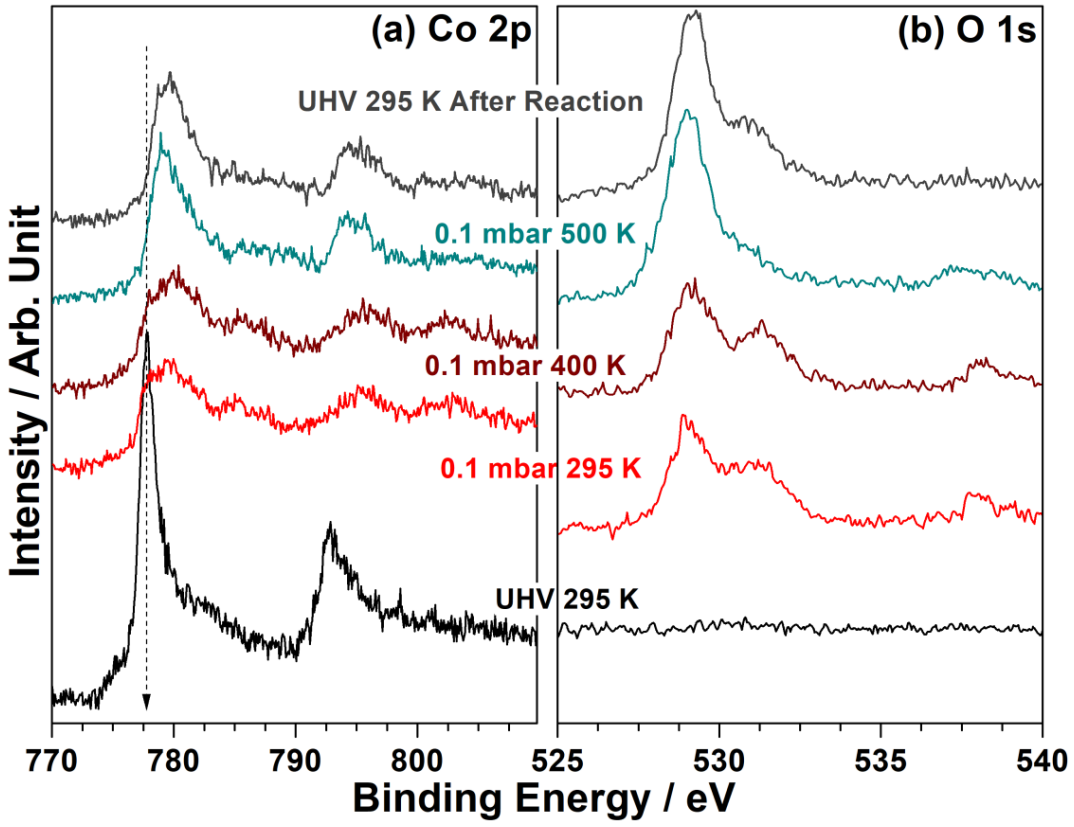

Figure 3.2: *In-situ* NAPPES studies of Co 2*p* and O 1*s* core level spectra recorded during the oxidation from metallic cobalt to Co_3O_4 at different pressures and temperatures.

was observed at 529.3 eV. This is attributed to the lattice oxygen of CoO and/or Co_2O_3. Another O 1*s* feature was also observed at 531 eV with different intensities and it depends on the experimental conditions. This is attributed to the electrophilic oxygen adsorbed on the

Co-metal or cobalt oxide. However, this feature is observed with low intensity at 500 K/0.1 mbar indicating the adsorbed oxygen oxidized the surface of cobalt oxides under the present experimental conditions. Weak core level feature for molecular oxygen was observed at 538.2 and 537.3 eV at 300 and 500 K, respectively, at 0.1 mbar O_2 partial pressure. Low BE shift observed in core level feature of molecular O_2 is attributed to the electronic factor due to change in the ϕ of CoO and Co_3O_4, respectively. This is in good correspondence with the shift in the BE of gas-phase O_2 in NAP-UPS (Fig. 3.1c).

3.2.3. Energy level changes of various Co-oxides

A significant admixture of cobalt 3*d* with oxygen 2*p* orbitals leads to a hybridized description of the valence band,

$$\Psi_{vb} = \alpha 3d^7 + \beta 3d^8 \underline{L} + \gamma 3d^9 \underline{L}^2 \qquad \text{(Eq. 1)}$$

where, $\underline{L}$ represents a hole in the O 2*p* orbital due to charge transfer to Co 3*d* orbitals. Possible initial states and final state configurations in PES are shown in Figure 3.3. The significant admixture of O 2p with Co 3*d* orbitals results in the formation of Co $3d^7$ and Co $3d^8$L-O $2p^5$ initial states (Fig. 3.3). The contribution from $3d^9 \underline{L}^2$ O $2p^5$ initial states is assumed to be negligible, due to high ligand to metal charge transfer energy (Δ) (LMCT) and d-d Coulomb interaction energy (U). Among the two initial states, Co $3d^8 \underline{L}$-O $2p^5$ state is at higher energy due to Δ, compared to Co $3d^7$ state. The photo excitation from a cobalt 2*p* core level to high probability final states Co-$2p^5 3d^7$ and Co-$2p^5 3d^8 \underline{L}$ is shown in Fig. 3.3a. Due to the charge transfer, Co-$2p^5 3d^8 \underline{L}$ effectively screens the core hole, and this leads to the main line at lower BE. The another competing process corresponds to the less screened state Co-$2p^5 3d^7$, where there is no charge transfer from the ligand. Corresponding state Co-$2p^5 3d^7$ peak appears as a broad satellite peaks at higher BE relative to the main line. Charge compensation occurs through the core *s*, *p* orbitals in the latter case. The energy reversal occurs due to the strong columbic attraction between the Co 2*p* core hole and Co 3*d* valence electron and the same is denoted as Q.[35]

CoO exhibits rock salt structure with the octahedral high spin Co^{2+} species comprising 4 atoms per unit cell with a Co-O bond length of 2.13 Å. Cobalt monoxide has high spin $t_{2g}^5 e_g^2$ configuration in the ground state, and hence the main VB generated from the Co 3*d* t_{2g} orbital. Due to LMCT, CoO shows two VB features resulted from $3d^7\underline{L}$ and $3d^6$ final states and the second feature appeared at 10.1 eV (Fig. 3.1a). This intense satellite peak was

expected due to stable low spin $3d^6$ final state configuration. Feature reported at 3.8 eV originates from the Co 3*d* orbital with e_g character. Oxygen 2*p* bands are observed at 5.1 and 7.6 eV.[36] Strong hybridization between the Co 3*d* and O 2*p* leads to such changes and this is confirmed by Co 2*p* core level and VB spectroscopy. Modifications of the Co 2*p* satellite are directly related to the oxide stoichiometry and it is extremely sensitive to the oxidizing conditions. The energy of these features is in good agreement with the values reported for standard CoO.[26,31] Although the secondary electrons increase above 10 eV, gas-phase features are fully observed.

The Co_3O_4 is a normal spinel structure with octahedral coordinated Co^{3+} and tetrahedral coordinated Co^{2+} in 2:1 ratio, respectively. In Co_3O_4, two different cationic sites are available and each type occupies partially to give unit cell of 56 atoms. All the oxygen atoms are at equivalent sites in Co_3O_4 with a Co^{3+}-O bond length of 1.89 Å and Co^{2+}-O bond length of 1.99 Å.[37] Because of two oxidation states and different *d* electron configurations, the electronic structure of Co_3O_4 (and similar spinel with other metal ions) is more complex than dioxide. As a result of different Co-O bond lengths and oxidation states, it is expected to exhibit a difference in the bonding nature (covalent or ionic nature), and chemical shift leads to different satellite features and valence band structure.

The 3*d* orbital of Co^{3+} in Co_3O_4 undergo crystal field splitting in the presence of O^{2-} ligands to form the low energy t_{2g} singlet state with full occupancy (6 electrons; t_{2g}^6) and high energy e_g doublet state. According to cluster energy calculations by Sawatzky et al.[38], if charge transfer energy (Δ) is more than that of Coulombic attraction energy (Q), there is no satellite or very low intensity satellite peak to be observed. The charge transfer energy depends upon the nature of ligands and its hybridization nature with metal.[39] Due to high ionic character of Co^{3+}-O (1.89 Å) bond in Co_3O_4 (compared to Co^{2+}-O (2.13Å) in CoO), charge transfer energy (Δ) is very high and it leads to low energy difference between Δ and Q. Thus, there is very low intensity satellite feature at high BE was observed; the schematic representation is shown in Fig. 3.3b. Tetrahedral coordinated Co^{2+} forms the low energy e^4 state with fully-filled electrons and high energy t_2^3 states with half-filled electrons.[37] Hence, the high probability of formation of both Co-$2p^5 3d^7$, and Co-$2p^5 3d^8$ $\underline{L}$ final states, as shown in Fig 3.3c, was observed due to the ample charge transfer from O^{-2} to Co^{2+}. However, we observed very low intense and broad satellite feature for Co_3O_4 in both NAP-UPS and XPS, compared to CoO. It is attributed to the presence of low percent of Co^{2+} (33.3 %) ions and the nature of

the bond Co^{2+}-O (1.99 Å). From the present NAPUPS results, it is evident that the significant electronic structure details are observed with differently filled Co 3*d* levels in Co_3O_4.

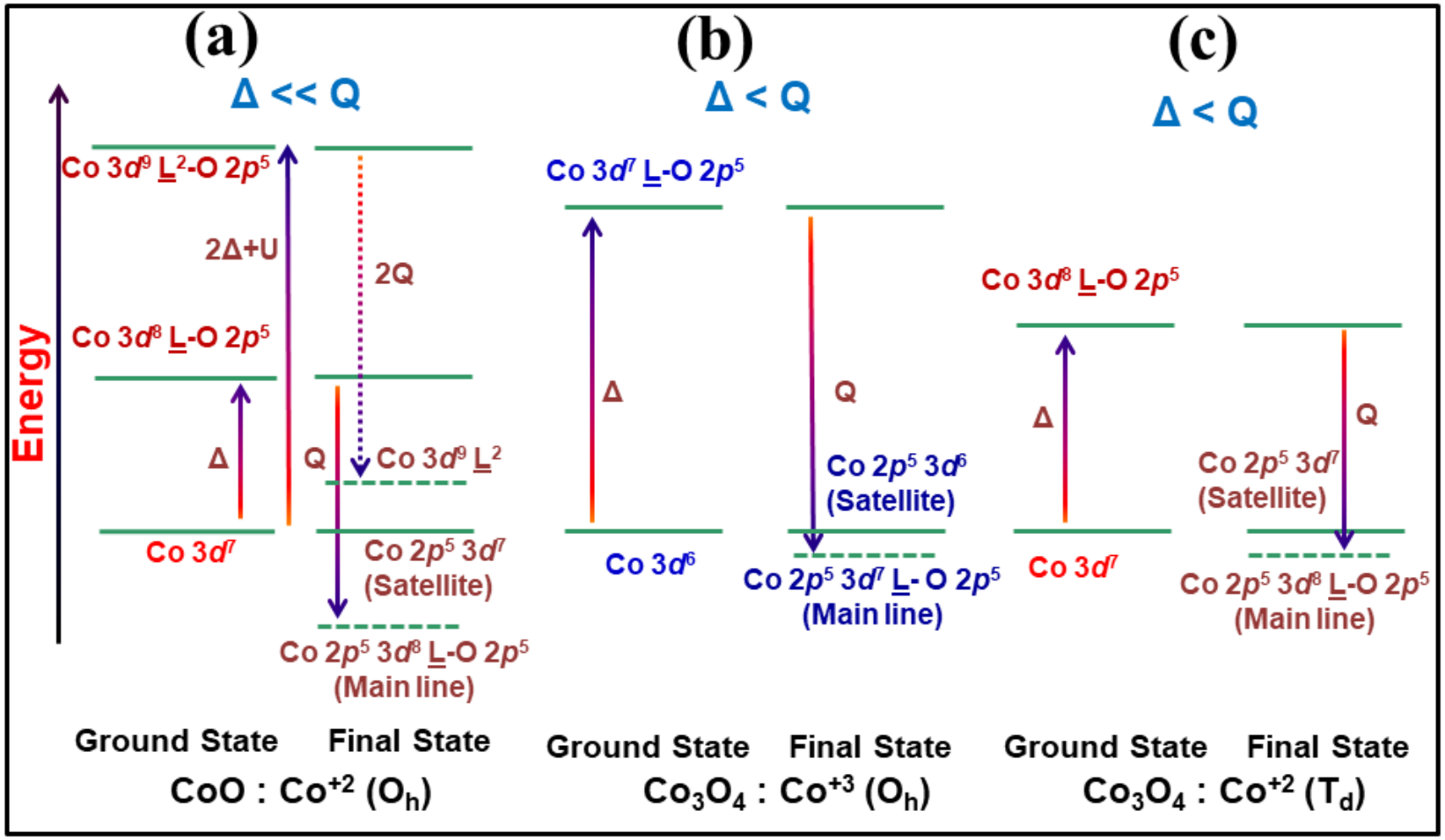

Figure 3.3: Schematic energy level to show charge transfer (Δ) in the ground state and energy reversal in the final state configuration corresponding to the main line.

3.2.4. Co + O_2 Interaction: UHV to 1 mbar O_2 pressure at room temperature

We have attempted to generate Co_3O_4 oxide film on metallic Co foil by systematically increasing the temperature and O_2 partial pressure. Co metal has been oxidized easily to CoO by increasing the oxygen pressure from 10^{-6} to 1 mbar at 295 K and NAP-UPS (Fig. 3.4a) and NAP-XPS (Fig. 3.4b) recorded were evident for that. Nonetheless, Co metal cannot be oxidised beyond CoO at 1 mbar and 295 K. In fact, Co 2*p* core level (Fig. 3.4b) shows the metallic Co, in addition to CoO, underscoring the oxidation is limited to few surface layers.

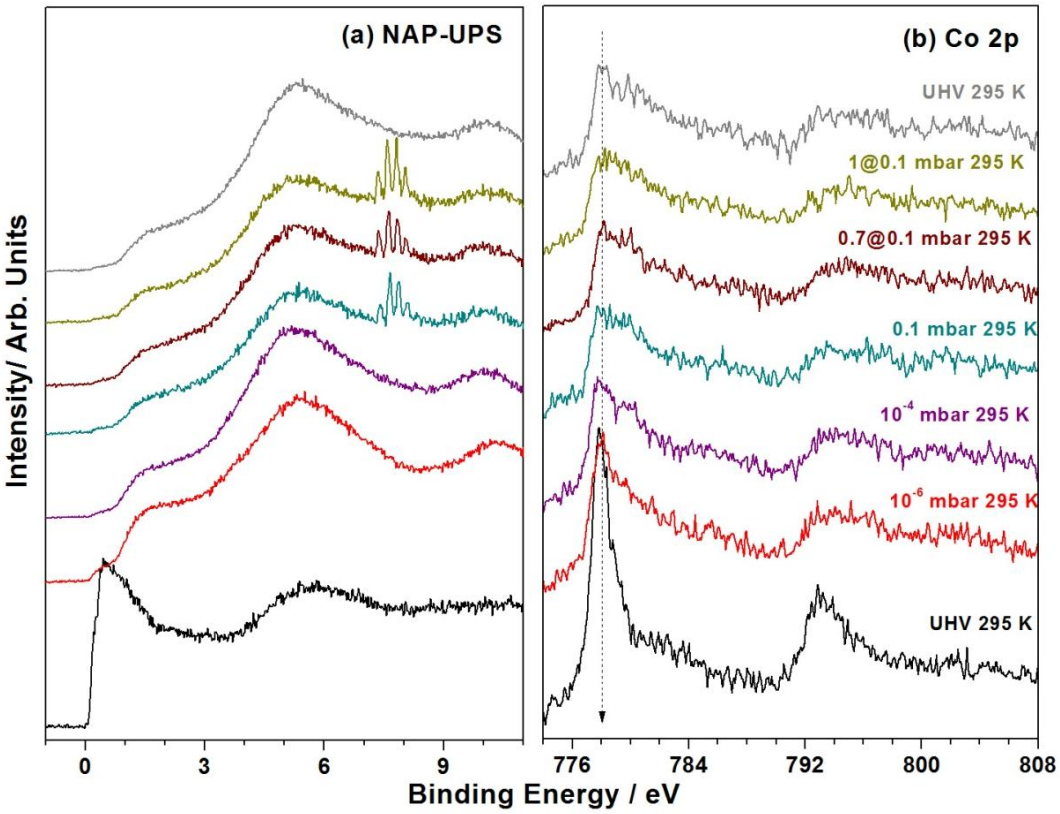

Figure 3.4: NAP-UPS results recorded during oxidation of Co metal with different pressure and at 295 K. Last but two spectra were recorded at 0.1 mbar pressure, but oxidized at 0.7 (maroon) 1 (dark yellow) mbar. No significant change in spectrum was observed in NAP-UPS above 0.1 mbar; whereas significant changes were observed in core level due to exposure to high pressures.

3.2.5. Co + O_2 Interaction: UHV to 10^{-4} mbar O_2 at different temperatures

We also attempted a set of spectra recorded at 10^{-6} mbar and up to 750 K towards maximum possible oxidation to Co_3O_4 was not successful; even after prolonged exposure to

few hours at 750 K, surface layers were not oxidized beyond CoO (Fig. 3.5a). Upon increasing the temperature metallic features decreased rapidly and oxide VB character increased; complete oxidation to CoO occurs at 600-650 K. Metallic Co 2*p* feature disappeared completely and a strong satellite observed indicates the oxidation to CoO to at least up to 7 nm and beyond the XPS probing depth. On further increasing the temperature to 750 K there is no further oxidation was observed at 10^{-6} mbar (Fig. 3.5a); O_2 partial pressure at 10^{-6} mbar and 750 K seems to be insufficient to oxidize CoO to Co_3O_4. We further performed experiments with an increase in pressure from 10^{-6} to 10^{-4} mbar at 750 K (Fig. 3.5). At 10^{-4} mbar at 750 K, CoO gets oxidized to Co_3O_4, beyond XPS probing depth, and typical Co_3O_4 features were observed.

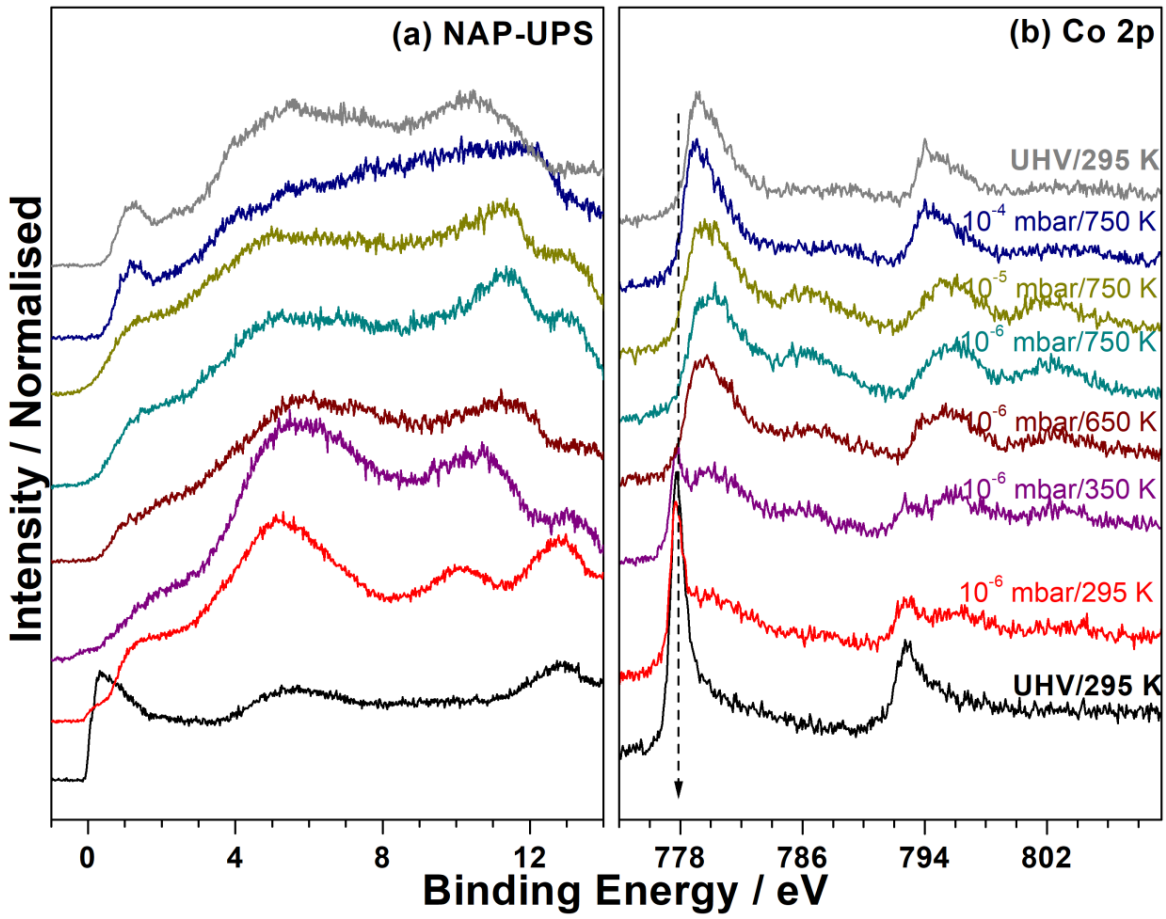

Figure 3.5: NAP-UPS and Co 2p core level results recorded during oxidation of Co metal at different pressure and temperature conditions. 10^{-6} mbar at 750 K data remains the same and exhibit CoO features, even after prolonged exposure for 4 h.

3.2.6. XRD and Raman spectral studies of Co-oxide surfaces

To confirm the spinel structure of Co_3O_4 thin films, they were characterized by ex-situ Raman, UV-Visible spectroscopy and x-ray diffraction (XRD). Fig. 3.6a shows the result obtained from Raman spectrum; features located at 194, 475, 516, 613 and 680 cm^{-1}, correspond to F_{2g}, E_g, F_{2g}, F_{2g} and $1A_{1g}$ Raman active modes of crystalline spinel cobalt oxide, respectively. High intense peak at 194 cm^{-1} and broad peak at 516 cm^{-1} is attributed to oxygen vibration involving E_g (O-Co-O bending), and A_{1g} (O-Co stretching) modes.[40-42] UV-Visible absorption spectrum exhibiting absorption peaks characteristics of Co_3O_4 (Fig. 3.6b) with a band gap of 1.4 eV; absorption spectral results are comparable to the earlier reports.[43,44]

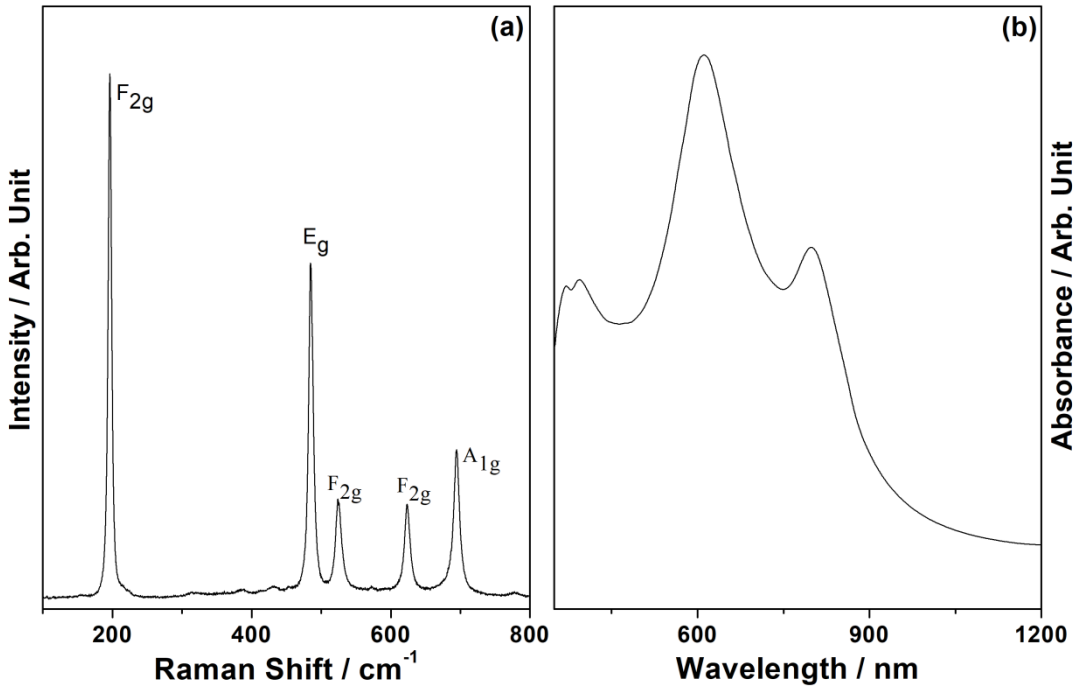

Figure 3.6: (a) Raman spectra (b) UV-Visible absorbance spectra of the *in-situ* prepared Co_3O_4 thin film in NAPPES.

Co-oxide generated on the surface due to Co + O_2 interaction in NAPPES instrument was evaluated by XRD measurement for the structural aspects and the results are shown in Fig. 3.7. XRD results (Fig. 3.7) shows six diffraction peaks located at 2θ = 42, 44.9, 47.9, 62.9, 76.2, 84.6^0. Features at 44.9 and 76.2^0 correspond to (111) and (220) planes, respectively, of cubic structure of the Co-metal. Remaining peaks at 47.9, 84.6 correspond to the (101), (103) plane of cobalt in a hexagonal structure. The peak at 62.9 belongs to the (220) plane of cubic

Co_3O_4 structure. The feature at 42^0 belongs to the (200) plane of the cubic CoO structure.[15] In conclusion, XRD pattern on in-situ prepared Co_3O_4 on Co foil contain dominant Cobalt metal phase from the bulk and significantly intense peak at 62.9 indicating the presence of Co_3O_4 phase predominantly on the surface. It demonstrates the oxidation is restricted to the surface. (Fig. 3.7).

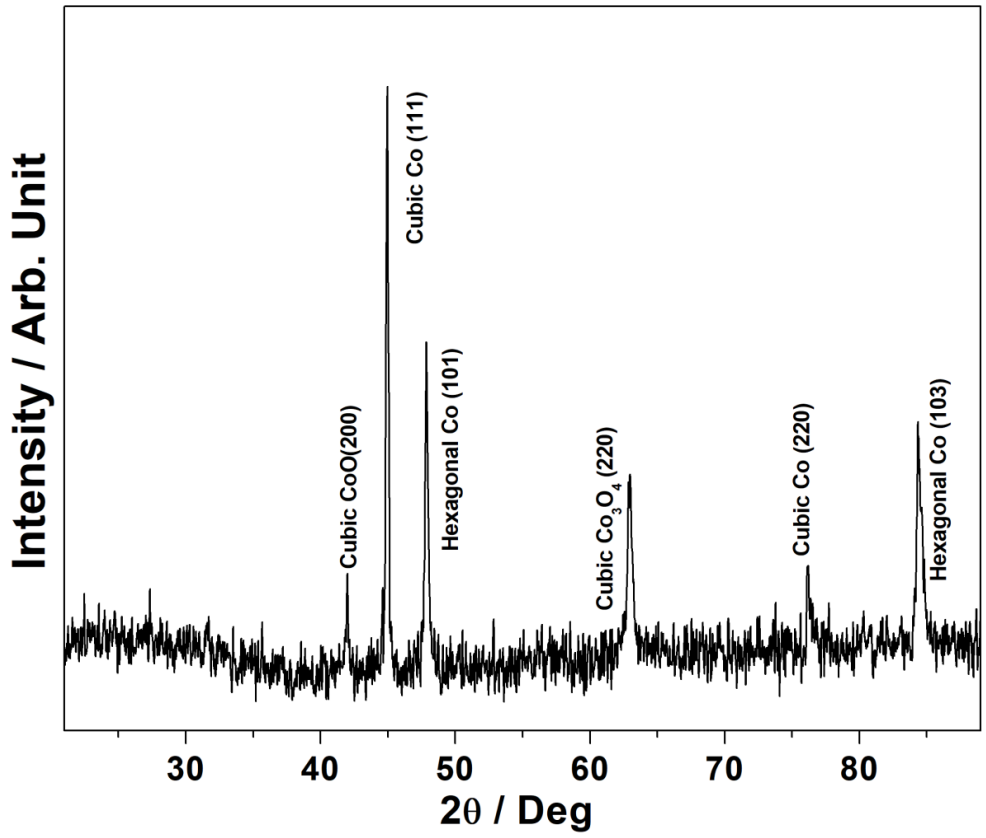

Figure 3.7: XRD pattern recorded for *in-situ* prepared Co_3O_4. It exhibits CoO and Co_3O_4 along with majority of metallic Co, arising from the bulk metal.

3.2.7. Co_3O_4 + H_2 Interaction: Temperature dependent NAP-UPS studies

It is known that CoO and Co_3O_4 can be interconverted by applying suitable redox conditions. However, what are the changes involved in the electronic structure under such conditions is not known, especially under equilibrium conditions in which both oxides co-exists. Reduction of the in-situ generated Co_3O_4 was explored under 0.1 mbar hydrogen pressure at different temperatures and the results are shown in Figs. 3.8 and 3.9 for NAPUPS and NAPXPS, respectively. Initially, there was no change in the VB spectrum of Co_3O_4 observed at 0.1 mbar partial pressure of H_2 at 295 K. Hydrogen vibrational features appeared between 11 and 12 eV. Nonetheless, compared to the reference gas-phase H_2 spectrum, 0.8 eV low BE

shift was observed on Co_3O_4 surface (inset in Fig. 3.8). This shift is attributed to the surface potential exerted by cobalt oxide surfaces. At 400 K, the main VB feature at 5 eV narrowed significantly, with a marginal decrease of the Co^{2+} feature at 3.8 eV (dashed arrow). Further, work function changes on the surface were supported by the shift in the vibrational features of H_2 towards higher BE. Significant broadening and intensity reduction of vibration features indicating a possible surface heterogeneity due to the partial reduction of surface layers. These changes mark the onset of reduction of spinel surface layers. Upon increasing the temperature gradually to 650 K under 0.1 mbar H_2 pressure, 3*d* features (both Co^{3+}, Co^{2+}) of Co_3O_4 completely disappeared as shown in Fig. 3.8. Typical Co^{3+} feature observed at 1 eV disappeared and a new broad feature appears at 1.5 eV, which is characteristic for Co^{2+}. Main VB further narrows down and shifts to 5.5 eV. Indeed, the spectrum recorded at 0.1 mbar H_2 and 650 K is similar to that of the spectrum obtained at 0.1 mbar O_2 at 400 K (Fig. 3.1a).

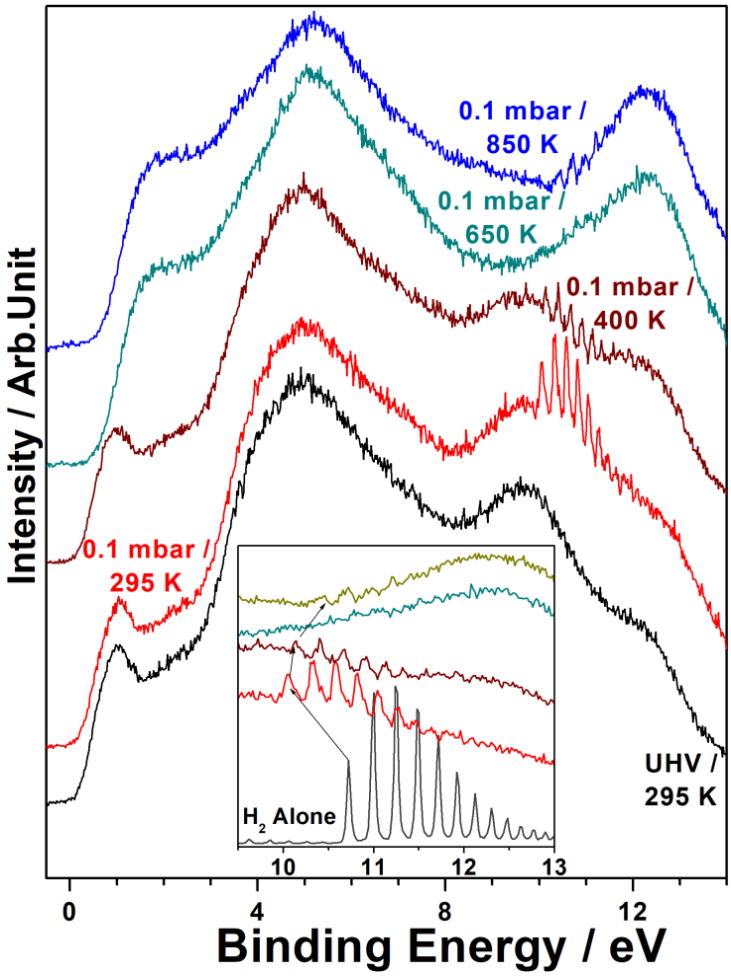

Figure 3.8: (a) NAP-UPS studies on Co_3O_4 reduction to CoO. Changes in H_2 vibrational features are shown in an expanded scale in the inset.

This demonstrates a complete reduction of spinel Co_3O_4 to CoO at 0.1 mbar H_2 at 650 K. It is also evident that Co_3O_4 and CoO can be reversibly obtained by alternating the conditions between 0.1 mbar H_2/650 K and 0.1 mbar O_2 at 400 K, respectively. In addition, there is a possibility of co-existence of CoO and Co_3O_4 by manipulating the above redox conditions; oxidative dehydrogenation reaction is an example for such conditions, where the reactions are carried out in an oxidative atmosphere and hydrogen is in-situ generated.[45-47] No further change in VB features was observed at 850 K and 0.1 mbar H_2 for prolonged exposure for an hour.

3.2.8. Co_3O_4 + H_2 Interaction: temperature dependent NAP-XPS studies:

Formation of CoO is further supported by the changes in the Co 2*p* and O 1*s* spectra shown in Fig. 3.9. On 0.1 mbar H_2 treatment up to 400 K, no change in the Co 2*p* or O 1*s* spectra were observed. However, at 0.1 mbar H_2/650 K, the Co 2*p* spectrum dramatically changed to show Co^{2+} feature with the strong satellite at high BE (784-788 eV). High-intensity satellite peak and marginally broadened main peak in XPS spectrum of Co 2*p* core level are indicative of the paramagnetic nature of CoO. However, on increasing the temperature to 800 K at 0.1 mbar H_2, main lines of Co 2*p* core level sharpened considerably, hinting the possibility of onset of bulk reduction, which is beyond the probing depth of XPS.

Satellite features intensity increased further on prolonged exposure and an intense satellite feature observed indicating the complete reduction to CoO. However, there were no traces of Co metal on the oxide surface was observed, highlighting the requirement of further high H_2 pressure for reduction to metal.

O 1*s* core-level data recorded is shown in Fig. 3.9b. Up on H_2 exposure at 0.1 mbar and up to 400 K, a high-intensity O 1*s* peak was observed at 529.3 eV. This is attributed to the lattice oxygen of Co_3O_4. At 0.1 mbar/650K a gradual shift in the BE to 529.8 eV indicating a change in surface nature from spinel to CoO, where corresponding Co 2*p* result also shows that spinel to CoO conversion.[48] Another O 1*s* feature was also observed at 531 eV is likely due to hydroxide formed on the cobalt oxide surface.[25,9,49] However, this feature is observed with low intensity up to 650 K/0.1 mbar of H_2, and it disappears at 850 K. indicating a possible dissociation of OH species.

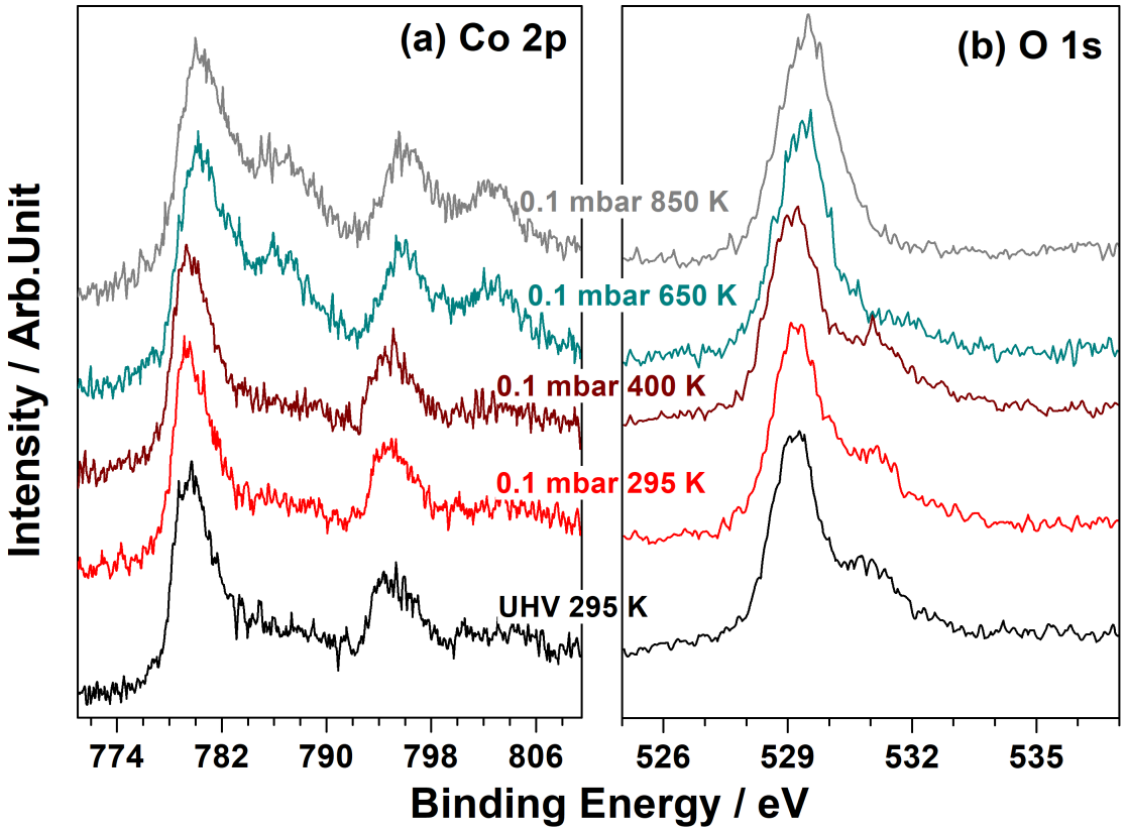

Figure 3.9: *In-situ* NAPPES studies of cobalt 2p and oxygen 1s core level photoemission energy during the reduction from Co_3O_4 to CoO at 0.1 mbar pressure of H_2 with different temperatures.

To understand the electronic structure of Co_3O_4, which contains heterovalent Co^{3+} and Co^{2+} cations, we compared the NAPXVB (NAP x-ray valence band) spectra (Fig. 3.10) with CoO to separate the electronic structure due to different valence states of cobalt ions. The difference was observed by much sharper core level and VB spectra in Co_3O_4. Especially, Co_3O_4 exhibited sharp NAPXVB peak at lower BE, while CoO showed broader peak due to multiple splitting from unpaired 3*d* electrons and *p-d* charge transfer satellite splitting. Comparison of both the spectra revealed that a shift in VB maximum occurs from 1.7 eV for CoO to 1 eV with a more intense peak for Co_3O_4. Lattice oxygen derived states are observed at the binding energy of 5.1 and 6.5 eV for Co_3O_4 and CoO.

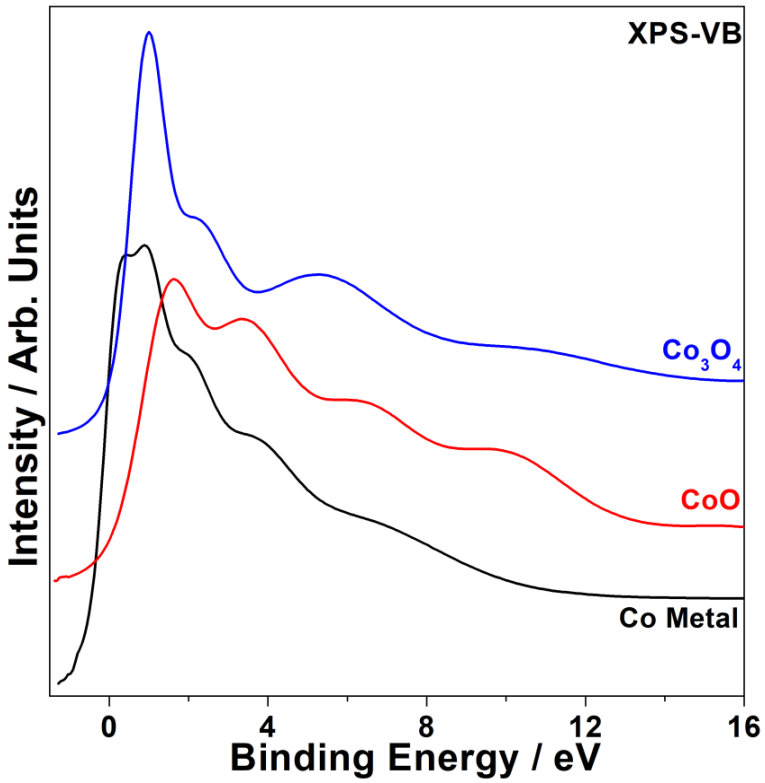

Figure 3.10: Comparison of x-ray valence band spectra of cobalt and its oxides in UHV-RT.

3.2.9. Surface dynamics and work function of Co_3O_4 + H_2 or Co+O_2 interaction

It is demonstrated that due to oxidation of surface in the presence of gaseous environment the work function also changes. Thus, to observe the changes in the work function of cobalt and its oxides, especially under reactive gases, we have chosen O_2 gas as a probe molecule. As shown in Fig 3.11, the oxygen vibrational feature is observed at 7.74 eV (for the highest intense feature in Fig. 3.1c) in the absence of Co or any surface, including sample holder (blank). At 0.01 mbar/295 K, the vibrational features of O_2 shifted to low BE at 7.45 eV, where the mixed phase of Co-metal and CoO co-exist; however, top 2 nm surface layers are fully oxidized to CoO. An increase in temperature to 400 K increases the work function and O_2 vibration feature shifts back to 7.75 eV and it corresponds to the existence of complete CoO phase (at least up to 7 nm, which is the probing depth of XPS). A further increase in temperature to 500 K shifts the O_2 vibrational feature dramatically towards lower BE to 7.2 eV, and it corresponds to the existence of Co_3O_4 phase. There is no change in the BE of vibrational features of oxygen while decreasing the temperature from 500 to 295 K demonstrates the temperature hardly influences vibration features, at least between 500 and 295 K. Of course, there was no change in surface nature and it remained as Co_3O_4. Moreover,

similar observations were made with the gaseous oxygen in O 1*s* spectra from XPS (Fig. 3.2b).

On the other hand, the exact opposite trend is observed during the reduction of Co_3O_4 to CoO under 0.1 mbar H_2 at different temperatures. BE of the highest intense H_2 vibration feature is plotted as a function of temperature and H_2 pressure in Fig. 3.11. Gas-phase H_2 alone shows vibrational feature at 11.3 eV. However it shifts dramatically to 10.3 eV at 295 K on Co_3O_4 surface. Onset of Co_3O_4 to CoO is reflected by a shift to 10.5 eV at 0.1 mbar/650 K. Complete reduction to CoO increases the vibrational feature BE to 10.7 eV. Axnanda et al.[17] calculated the work function of PbS by gaseous oxygen 1s core level shift. Thus, our present work establishes that NAPUPS can give more accurate changes in the work function than XPS due to more surface sensitive (~2 nm), and deals with only valence orbitals of the substrate (cobalt). Moreover, from NAPUPS low photo ionisation cross section containing gases like H_2 are observed; in fact, it is not possible to observe H_2 with XPS and similar trend in changes in work functions are observed by others.[49]

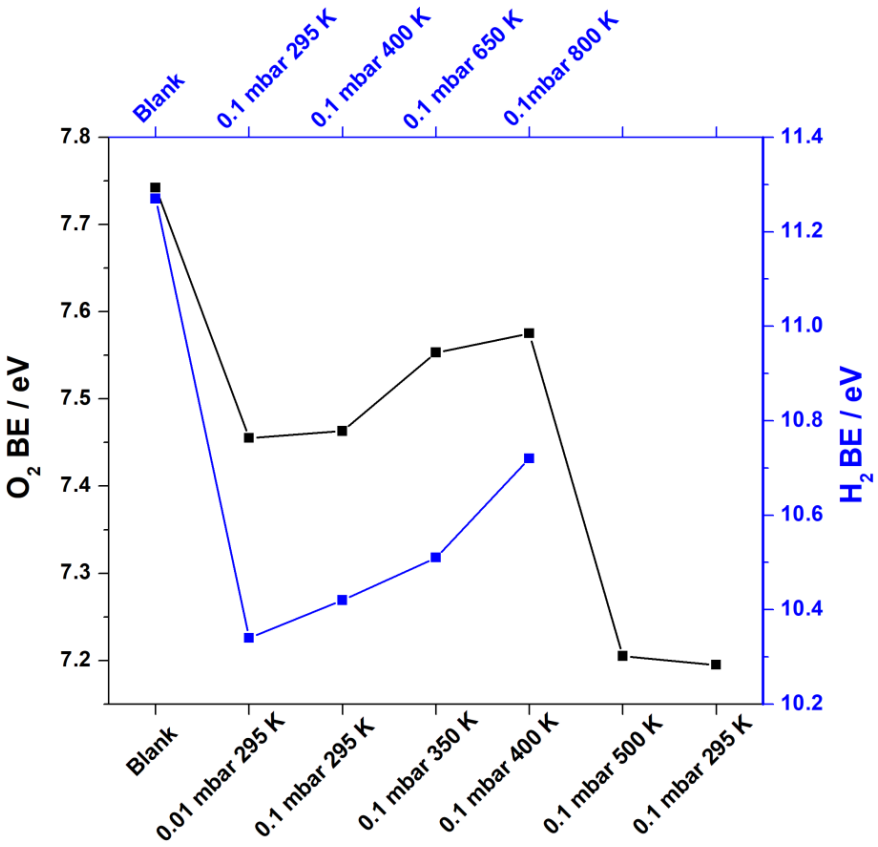

Figure 3.11: Shift in vibrational features of gas-phase oxygen and hydrogen during the oxidation of Co to Co_3O_4 and reduction of Co_3O_4 to CoO, respectively.

The direct evolution of the electronic and valence band structure has addressed three things: (a) changes in surface work function from metallic cobalt to Co_3O_4 via CoO through a shift in the molecular oxygen vibrational features. Reacting gases like oxygen and hydrogen vibrational features changes, which overcomes the limitations of traditional work function measurements under UHV, (b) the changes in the Fermi level features and also (c) Like CoO, Co_3O_4 also exhibits the charge transfer phenomena in valance 3d band structure, it is due to both Co^{3+} and Co^{+2} ion.

3.3. Conclusion

The evolution of the electronic structure of Co foil during oxidation has been probed using both ultra-violet and x-ray photoelectron spectroscopy at near ambient pressures and at high temperatures. Co metal gradually oxidizes to CoO at increasing pressure and between 350 and 400 K, and then to Co_3O_4 at 500 K . The formation of Co_3O_4 has been confirmed by Raman and UV-visible spectroscopy. The oxide layer is restricted to the surface only and confirmed by XRD technique. From NAP-UPS, a clear difference in the VB features and Fermi level of Co and its oxides was observed; this is well corroborated with x-ray VB results. The top of the VB shows a sharp peak at 1 eV, which is assigned to the Co^{3+} octahedral state. Enhancement in the satellite peak is indicating the charge transfer nature of Co_3O_4. The work function changes of CoO under reactive oxidation conditions were observed from the O_2 vibrational features in NAP-UPS, this was clearly supported by the gaseous oxygen 2*p* core level XPS. Further Co_3O_4 is reversible at 0.1 mbar of H_2 and 800 K, and it is reduced to CoO but not to Co metal. This further strongly supports the XPS and UPS finding of oxygen vibrational features on Co_3O_4 and CoO surfaces.

3.4. References

(1) Inoue, A.; Shen, B.; Koshiba, H.; Kato, H.; Yavari, A. R. *Nat. Mater* **2003**, *2*, 661-663.

(2) Qiao, L.; Xiao, H. Y.; Meyer, H. M.; Sun, J. N.; Rouleau, C. M.; Puretzky, A. A.; Geohegan, D. B.; Ivanov, I. N.; Yoon, M.; Weber, W. J.; Biegalski, M. D. *J. Mater. Chem. C.* **2013**, *1*, 4628-4633.

(3) Abbate, M.; Fuggle, J. C.; Fujimori, A.; Tjeng, L. H.; Chen, C. T.; Potze, R.; Sawatzky, G. A.; Eisaki, H.; Uchida, S. *Phys. Rev. B* **1993**, *47*, 16124-16130.

(4) Li, W. Y.; Xu, L. N.; Chen, J. *Adv. Funct Mater.* **2005**, *15*, 851-857.

(5) Melaet, G. r. m.; Ralston, W. T.; Li, C.-S.; Alayoglu, S.; An, K.; Musselwhite, N.; Kalkan, B.; Somorjai, G. A. *J. Am. Chem. Soc.* **2014**, *136*, 2260-2263.

(6) Mattioli, G.; Giannozzi, P.; Amore Bonapasta, A.; Guidoni, L. *J. Am. Chem. Soc.* **2013**, *135*, 15353-15363.

(7) Xie, X.; Li, Y.; Liu, Z.-Q.; Haruta, M.; Shen, W. *Nature* **2009**, *458*, 746-749.

(8) Dubey, A.; Reddy, K. P.; Gopinath, C. S. *ChemistrySelect* **2017**, *2*, 533-536.

(9) Iablokov, V.; Barbosa, R.; Pollefeyt, G.; Van Driessche, I.; Chenakin, S.; Kruse, N. *ACS Catal.* **2015**, *5*, 5714-5718.

(10) Zhang, L.; Zhao, X.; Ma, W.; Wu, M.; Qian, N.; Lu, W. *CrystEngComm* **2013**, *15*, 1389-1396.

(11) Gopinath, C. S.; Roy, K.; Nagarajan, S. *ChemCatChem* **2015**, *7*, 588-594.

(12) Maity, N.; Rajamohanan, P. R.; Ganapathy, S.; Gopinath, C. S.; Bhaduri, S.; Lahiri, G. K. *J. Phys. Chem. C.* **2008**, *112*, 9428-9433.

(13) Murali, C.; Shashidhar, M. S.; Gopinath, C. S. *Tetrahedron* **2007**, *63*, 4149-4155.

(14) Gopinath, C. S. *J. Phys. Chem. B.* **2006**, *110*, 7079-7080.

(15) Jain, R.; Gnanakumar, E. S.; Gopinath, C. S. *ACS Omega* **2017**, *2*, 828-834.

(16) Yeh, J. J.; Lindau, I. *Atomic Data and Nuclear Data Tables* **1985**, *32*, 1-155.

(17) Axnanda, S.; Scheele, M.; Crumlin, E.; Mao, B.; Chang, R.; Rani, S.; Faiz, M.; Wang, S.; Alivisatos, A. P.; Liu, Z. *Nano Lett.* **2013**, *13*, 6176-6182.

(18) De Santis, M.; Buchsbaum, A.; Varga, P.; Schmid, M. *Phys. Rev. B: Condens. Matter.phys.* **2011**, *84*, 125430.

(19) Potoczna-Petru, D.; Kępiński, L. *Catal. Lett.* **2001**, *73*, 41-46.

(20) Martin, M.; Koops, U.; Lakshmi, N. *Solid State Ionics* **2004**, *172*, 357-363.

(21) Yu, T.; Zhu, Y. W.; Xu, X. J.; Shen, Z. X.; Chen, P.; Lim, C. T.; Thong, J. T. L.; Sow, C. H. *Adv. Mater.* **2005**, *17*, 1595-1599.

(22) Chen, J.; Wu, X.; Selloni, A. *Phys. Rev. B* **2011**, *83*, 245204.

(23) Brundle, C.; Chuang, T.; Rice, D. *Surf. Sci.* **1976**, *60*, 286-300.

(24) Bridge, M.; Lambert, R. *Surf. Sci.* **1979**, *82*, 413-424.

(25) Castro, G.; Küppers, J. *Surf. Sci.* **1982**, *123*, 456-470.

(26) Papaefthimiou, V.; Dintzer, T.; Dupuis, V. r.; Tamion, A.; Tournus, F.; Hillion, A.; Teschner, D.; Hävecker, M.; Knop-Gericke, A.; Schlögl, R. *ACS Nano* **2011**, *5*, 2182-2190.

(27) Wu, C. H.; Eren, B.; Bluhm, H.; Salmeron, M. B. *ACS Catal.* **2017**, *7*, 1150-1157.

(28) Walton, A. S.; Fester, J.; Bajdich, M.; Arman, M. A.; Osiecki, J.; Knudsen, J.; Vojvodic, A.; Lauritsen, J. V. *ACS Nano* **2015**, *9*, 2445-2453.

(29) Roy, K.; Gopinath, C. S. *Anal. Chem.* **2014**, *86*, 3683-3687.

(30) Roy, K.; Vinod, C.; Gopinath, C. S. *J. Phys. Chem. C* **2013**, *117*, 4717-4726.

(31) Langell, M.; Anderson, M.; Carson, G.; Peng, L.; Smith, S. *Phys. Rev. B* **1999**, *59*, 4791.

(32) Brookes, N.; Law, D.-L.; Warburton, D.; Wincott, P.; Thornton, G. *J. Phys.: Condens. Matter* **1989**, *1*, 4267.

(33) van Elp, J.; Wieland, J. L.; Eskes, H.; Kuiper, P.; Sawatzky, G. A.; de Groot, F. M. F.; Turner, T. S. *Phys. Rev. B* **1991**, *44*, 6090-6103.

(34) Greiner, M. T.; Helander, M. G.; Tang, W.-M.; Wang, Z.-B.; Qiu, J.; Lu, Z.-H. *Nat. Mater* **2012**, *11*, 76-81.

(35) Shen, Z. X.; Allen, J. W.; Lindberg, P. A. P.; Dessau, D. S.; Wells, B. O.; Borg, A.; Ellis, W.; Kang, J. S.; Oh, S. J.; Lindau, I.; Spicer, W. E. *Phys. Rev. B* **1990**, *42*, 1817-1828.

(36) Kim, K. S. *Phys. Rev. B* **1975**, *11*, 2177-2185.

(37) Kormondy, K. J.; Posadas, A. B.; Slepko, A.; Dhamdhere, A.; Smith, D. J.; Mitchell, K. N.; Willett-Gies, T. I.; Zollner, S.; Marshall, L. G.; Zhou, J.; Demkov, A. A. *J. Appl. Phys.* **2014**, *115*, 243708.

(38) Zaanen, J.; Westra, C.; Sawatzky, G. A. *Phys. Rev. B* **1986**, *33*, 8060-8073.

(39) Park, J.; Ryu, S.; Han, M.-s.; Oh, S. J. *Phys. Rev. B* **1988**, *37*, 10867-18075.

(40) He, X.; Song, X.; Qiao, W.; Li, Z.; Zhang, X.; Yan, S.; Zhong, W.; Du, Y. *J. Phys. Chem. C* **2015**, *119*, 9550-9559.

(41) Wang, X.; Song, L.; Yang, H.; Xing, W.; Lu, H.; Hu, Y. *J. Mater. Chem.* **2012**, *22*, 3426-3431.

(42) Zhang, L.; Zhao, X.; Ma, W.; Wu, M.; Qian, N.; Lu, W. *CrystEngComm* **2013**, *15*, 1389-1396.

(43) Jiang, C.-M.; Baker, L. R.; Lucas, J. M.; Vura-Weis, J.; Alivisatos, A. P.; Leone, S. R. *J. Phys. Chem. C* **2014**, *118*, 22774-22784.

(44) Ngamou, P. H. T.; Bahlawane, N. *Chem. Mater.* **2010**, *22*, 4158-4165.

(45) Sivaranjani, K.; Verma, A.; Gopinath, C. S. *Green Chemistry* **2012**, *14*, 461-471.

(46) Mapa, M.; Sivaranjani, K.; Bhange, D. S.; Saha, B.; Chakraborty, P.; Viswanath, A. K.; Gopinath, C. S. *Chem. Mater.* **2010**, *22*, 565-578.

(47) Venugopal, A. K.; Venugopalan, A. T.; Kaliyappan, P.; Raja, T. *Green Chemistry* **2013**, *15*, 3259-3267.

(48) Mathew, T.; Shiju, N.; Sreekumar, K.; Rao, B. S.; Gopinath, C. S. *J. Catal.* **2002**, *210*, 405-417.

(49) Wu, C. H.; Eren, B.; Bluhm, H.; Salmeron, M. B. *ACS Catal.* **2017**, *2*, 1150-1157.

Chapter-4

Mapping Valence Band and Interface Electronic Structure Changes during Oxidation of Mo to MoO_3 via MoO_2 and MoO_3 Reduction to MoO_2 : A NAPPES Study

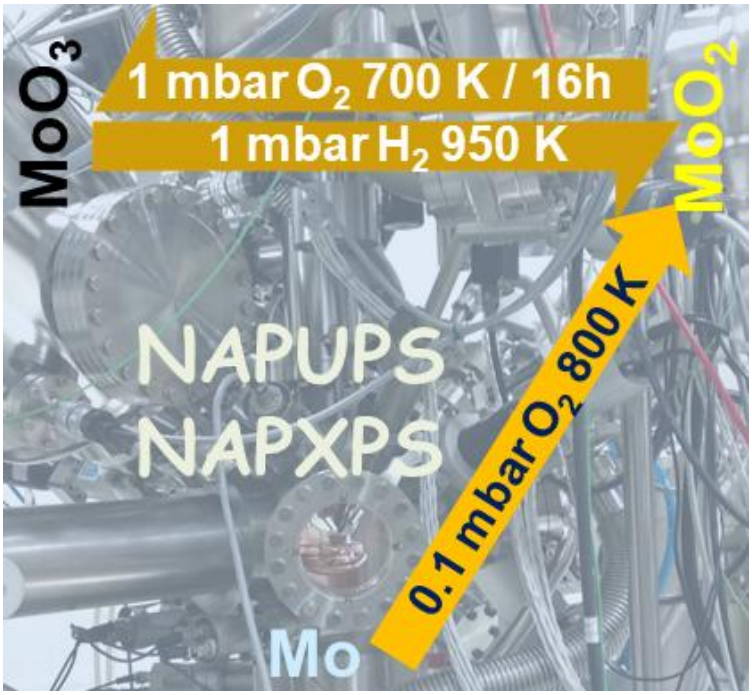

Part of chapter 4 has been published and the details are[2]

[2] **Reddy, K. P.;** Mhamane, N. B.; Ghosalya, M. K.; Gopinath, C. S., Mapping Valence Band and Interface Electronic Structure Changes during Oxidation of Mo to MoO_3 via MoO_2 and MoO_3 Reduction to MoO_2 : A NAPPES Study. *J. Phys. Chem. C.* **2018**, *122*, 23034-23044.

4.1. Introduction

Low dimensional metal oxide thin films have received considerable attention because of their unique multifunctional properties such as, electrical, optical, catalytic and mechanical properties. Among the low dimensional transition metal oxides, molybdenum trioxide (MoO_3) is an important oxide widely used in electronics to energy storage materials.[1-3] Molybdenum forms two oxides, namely, molybdenum dioxide (MoO_2) and molybdenum trioxide (MoO_3). MoO_3 exist in three phases, namely (a) monoclinic, (b) h-MoO_3, and (c) thermodynamically stable α-MoO_3. The α-MoO_3 contains orthorhombic layered structure and the layers are bound to each other by weak van der Waals forces.[4] There are three unique oxygen positions in α-MoO_3 and the catalytic activity of material mainly depends on the sensitivity of the type of oxygen exposed. To identify, understand and explain the significance of different surface species in catalysis, experiments have been performed systematically by oxidising the surface layers of Mo foil into MoO_3 thin film and the reduction of in-situ generated MoO_3 to MoO_2. By varying the conditions of the oxidation/reduction, the nature of the surface oxide or surface nature can be controlled. In α-MoO_3, the Mo^{6+} have a vacant 4*d* shell with a band gap of 2.9 eV; however, oxygen deficiency in α-MoO_3 leads to a mid-gap states close to the conduction band minimum (CBM), making it an n-type semiconductor.[5] It is to be noted that Fermi level lies close to the CBM, which is composed of empty Mo 4*d* states; however the valence band maximum (VBM) consists of O 2*p* states. α-MoO_3, exhibits large ϕ (6.8 eV) with deep-lying CB, and hence acts as an efficient buffer layer for charge transport in organics electronics.[6,7] The efficient transfer of charge between the organic layer and electrical contact can proceed via MoO_3 layer due to appropriate energy levels and ϕ. However, low electrical conductivity of α-MoO_3 limits the wide spread use for various applications.[8] Oxygen vacancies in α-MoO_3 can give electrons to 4d orbitals of the Mo and decrease the crystal field energy/splitting adequately to allow the formation of 4*d* mid gap states, which is responsible for an increase in the conductivity and decrease in the ϕ properties of the material.[9] Hence, studies on the electronic properties of non-stoichiometric MoO_3 are very important for various applications. For charge exchange between solids, the ϕ function is an important factor, as this factor decides the energy needed for adding or removing electron to or from E_F. However charge transfer between solid and gas molecule significantly depends upon the ϕ of solid; hence an understanding of how to tune the ϕ is very important in organic semiconductor devices, photocatalysis, electrochemistry etc.[10-14]

Various approaches has been proposed to produce substantial gap states in these wide band gap semiconductors, such as introduction of dopants to bring donor or acceptor states in various position above the VB.[8,15-17] The non-stoichiometric MoO_{3-x}, rather than stoichiometric MoO_3, was found to be better suited for the charge exchange at the organic semiconductor (OSC)/MoO_3 interfaces, and thus greatly improve the device performance;[18] however, very less information is available on Mo^{5+} at interfaces and its characteristics. Datta et al., has shown the oxygen deficient MoO_3 is highly active for the electrochemical hydrogen evolution reaction than the stoichiometric MoO_3 with low over potential and faster reaction kinetics.[19] Davazoglou et al., succeeded in utilizing oxygen vacancies in WO_3 and MoO_3 films based organic light-emitting diodes and solar cells to improve the performance.[7,8] Kim et al., observed the high charge capacity in $MoO_{3-x.}$[1] Moreover, oxygen vacancies in MoO_3 are catalytically active sites for methane oxidation, reduction of NO, epoxidation of olefins and photo catalytic conversion of isopropyl alcohol to propylene.[20-25] In this chapter, we demonstrate the effective charge transfer during the oxidation from Mo oxidation to MoO_3 through MoO_2 and also observed significant changes in the ϕ, while evolving from Mo to MoO_3.

Most of the transition metal oxides have multiple oxidation states and high oxidation state is vulnerable to reduction, especially at an interface with metal or in general with electron-rich material. In such cases, lower oxidation states at interface are expected to be present.[26] In order to utilize the MoO_3 films, it is important to understand how the electronic structure and ϕ changes with MoO_x stoichiometry. The present work discusses the electronic structures of oxygen-deficient MoO_3, which retains layered orthorhombic structure. The valence band, core level electronic structure and ϕ changes of Mo and its oxides MoO_2, MoO_3, reduced forms of MoO_3 are studied under O_2 and H_2 atmosphere in the mbar pressure regime and elevated temperatures. Vibrational features of O_2 and H_2 is very sensitive to changes in electronic structure and surface compositions and directly reflects the changes in the ϕ.

4.2. Results and discussions

4.2.1. Mo + O_2 Interaction: pressure and temperature dependent NAP-UPS studies

UV valence band spectra of Mo surfaces were recorded as a function of oxygen partial pressure and temperature, and the results obtained are shown in Figure 4.1. The clean

Mo surfaces show Mo 4*d* features from 0 to 3 eV with high density of states (DOS) at Fermi level, as shown in Fig. 4.1b indicative of metallic state. A broad feature observed at 6 eV is attributed to defective sites present on the surface, due to extensive sputter cleaning. Surface defects are mostly associated with unsaturation, and expected to be similar in nature, irrespective of its origin. NAPXPS results from O 1s and C 1s core levels rule out the possibility of any oxide or carbon contamination. Large DOS at Fermi level arises due to the dispersion of Mo 4d, 4p, and 5s orbitals due to the electronic configuration of Mo to be [Kr] $4d^5\ 5s^1$.[27] It is also to be noted that both the outermost orbitals are half-filled and hence highly reactive. Although 5s is the outermost orbital, its binding energy is higher than 4d, due to its diffused character of O-shell and no specific 5s feature was observed.

Oxygen partial pressure was allowed to increase gradually from 10^{-6} to 0.1 mbar through several stages at room temperature. At 10^{-4} mbar O_2 pressure, a decrease in Fermi level intensity indicates the interaction of molecular oxygen with the Mo surface. Change in the Fermi level intensity together with a new distinct feature at 4 eV indicative of the oxygen chemisorption on Mo surface. On increasing the pressure to 0.1 mbar, vibrational features of gas-phase O_2 is observed at 7.6 eV. Even at 0.1 mbar pressure, E_F intensity was observed and it is comparable to that of at 10^{-4} mbar. This indicates the chemisorption is strictly restricted to surface layers and without any diffusion of oxygen atoms into sub-surface layers. Compared to the narrow and well-resolved features observed for pure O_2 gas-phase spectrum (shown in the Fig. 4.2), a large broadening was observed on Mo-surface hints the presence of at least two or more sites on the surface. Similar broadened vibration features was recently observed on Si-oxidation with O_2 by Ghosalya et al.[28] A brief note on the gas phase spectra of reactant molecules and its interaction with the Co-surface is reported in our earlier work.[29]

Upon further oxidation by increasing the temperature, while keeping the pressure constant at 0.1 mbar, interesting changes are observed. Some of the representative results are shown in Fig 4.1. On increasing the temperature gradually to 600 K, E_F intensity at 0 eV decreased substantially along with a decrease in the intensity of the feature at 2 eV and it appeared as broad peak (Fig. 4.1b).

Simultaneously, a clear shift in the O_2 vibrational feature to lower binding energy (6.8 eV) was observed suggesting an increase in the ϕ due to surface oxidation. At 800 K, we observed two distinct peaks at 0.5 and 1.6 eV below the Fermi level indicating the oxidation of metallic Mo to MoO_2 form. These two features are very typical for MoO_2 due to electrons

present in the 4*d* orbitals of Mo^{4+}.[30] Features at 0.5 and 1.6 eV features are attributed to the well screened (Mo $4d^2\underline{L}$; $\underline{L}$ indicates a hole on oxygen ligand due to charge transfer) and unscreened Mo^{4+} (Mo d^1) final states of MoO_2, respectively.

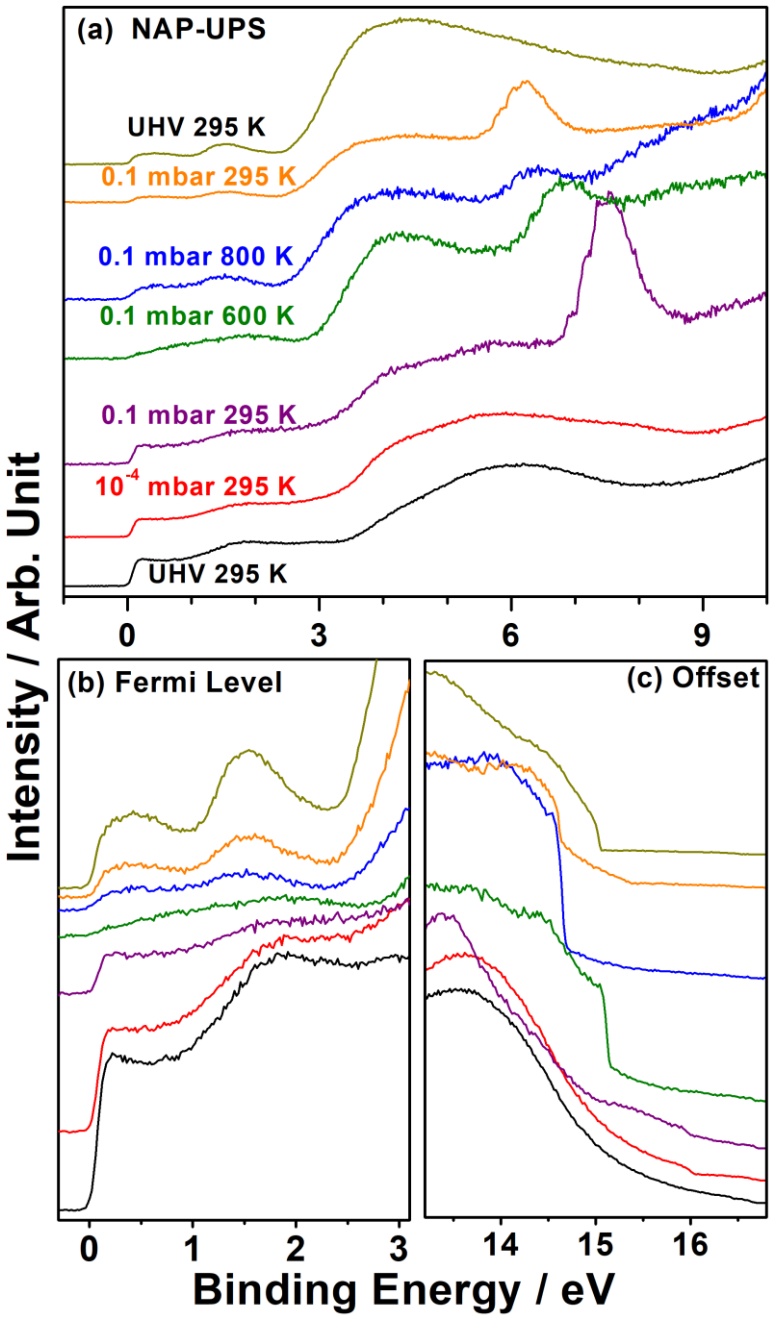

Figure 4.1: (a) NAPUPS spectra recorded as a function of O_2 pressure and temperature for the oxidation of metallic Mo to MoO_x. Enlarged view of (b) near E_F, and (c) the offset spectra are shown for finer changes.

As MoO_2 ϕ is more than Mo metal a further increase in ϕ and a decrease in the binding energy of vibrational features are expected. The distinct hump observed at 6 eV in low

pressure and temperature conditions disappear at 800 K; this is attributed to the predominant formation of MoO_2 on the surface. Further increase in temperature to 900 K as well as increase in O_2 pressure to 1 mbar does not change the spectral features significantly. Nonetheless a prolonged heating at 1 mbar pressure at 700 K, results in further oxidation to MoO_3. NAPUPS offset spectra are shown in Fig. 4.1c. A systematic change in the ϕ is observed from metallic Mo to MoO_2. This also supports the conclusion derived from gas-phase vibrational features shift. Pure O_2 gas-phase vibrational features at 0.1 mbar and deconvoluted vibrational features on Mo surface at various temperatures are shown in Fig. 4.2.

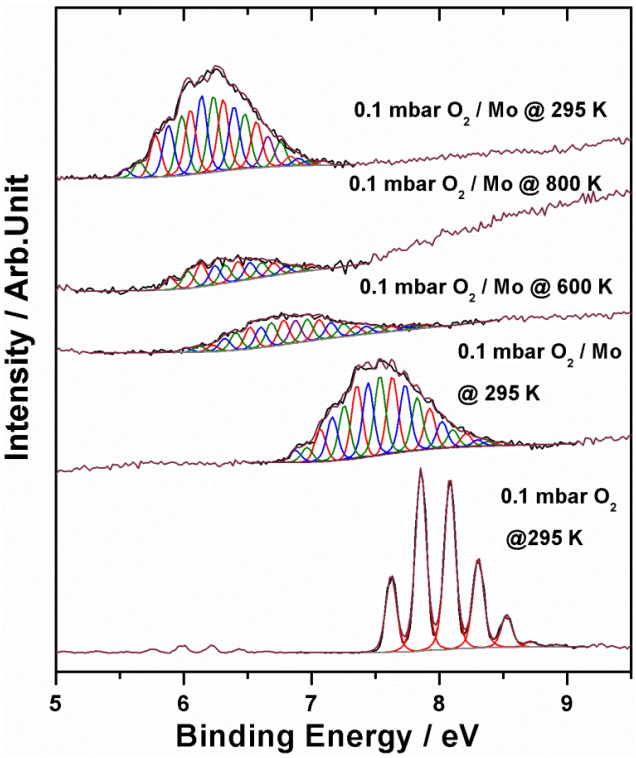

Figure 4.2: Oxygen gas vibrational features shown in Fig. 4.1 are deconvoluted for the identification of various sites present under NAP-UPS measurement conditions. Pure gas-phase O_2 vibrational features are shown for reference.

A deconvolution procedure applied by taking pure gas phase spectra as reference; FWHM and energy difference between adjacent peaks was maintained for all fitted features, as that of reference spectrum. At 0.1 mbar/295 K, there are three types of oxygen vibrational features observed indicates that three types of Mo species are present on the surface. After increasing the temperature to 600 K, the highly broadened vibration feature was shifted to lower BE; however there are no changes in the number of peaks. Similar type of fitting

observed under the remaining conditions, except for gradual decrease in the BE of vibrational features. In addition, change in the BE of vibrational features underscores the change in the nature of the surface sites too, in a dynamic manner under measurement conditions. Above observation demonstrates the catalyst surfaces are different under reactive conditions compared to fresh catalyst.

4.2.2. Mo + O_2 Interaction: time dependent NAP-UPS studies at 1 mbar and 700 K

Oxidation of MoO_2 to MoO_3 is a kinetically slow process and it requires around 16 h to completely oxidize surface layers of MoO_2 to MoO_3 at 1 mbar O_2 pressure and 700 K. NAPUPS spectra were recorded periodically to explore the evolution of the interface electronic structure and to measure the changes in ϕ; the results obtained are shown in Figure 4.3a, 4.3b and 4.3c. After every two hours of oxygen treatment at 700 K and 1 mbar pressure, spectra were recorded at UHV/295 K and compared in Fig. 4.3a. After treatment at 800 K at 0.1 mbar O_2 pressure, NAPUPS spectrum recorded at UHV/295 K shows distinct peaks at 0.5 and 1.6 eV; this observation indicates the Mo^{4+} species due to MoO_2 present on the surface. This is the same spectrum as that of a spectrum (brown trace) shown in Fig. 4.1a. Shen et al., has shown the metallic states observed by the introduction of the oxygen vacancies in MoO_2 or MoO_3.[31] After first 2 h O_2 treatment at 1 mbar and 700 K, spectrum was recorded at UHV/295 K. Intensity of the peaks at 0.5 and 1.6 eV decreases, indicating that there is a decrease in the Mo^{4+} content on the surface. It has been experimentally observed that α-MoO_3 is an oxygen-deficient material. This gives rise to n-type semiconducting behaviour due to the presence of two electrons available per oxygen vacancy site and they are associated with nearby Mo-ions. The signature of this is the reduction of Mo^{6+} into Mo^{5+} and Mo^{4+}. After 4 h O_2 treatment at 700 K, a further decrease in the intensity of Mo^{4+} feature was observed. After exposure of O_2 for a total of 6 h, only one broad peak was observed at 1.1 eV instead of two peaks. This is attributed to the formation Mo^{5+} at the surface and interface of MoO_3 and MoO_2. Further increase in the total exposure time to 12 h decreases the intensity of the peak at 1.1 eV; further, 0.2 eV shift in the valence band maxima towards the higher BE was observed. Shift to the higher BE is attributed to the increase in the energy gap between the Femi level to the valence band of MoO_3 due to the increase in the thickness of the MoO_3 layers on the surface. Additional oxygen treatment to a total of 16 h did not change the ϕ function further; intensity of the peak at 1.1 eV remained the same, indicating the complete oxidation to MoO_3 on the surface. This can be explained by assuming the formation of MoO_3,

in which molybdenum is in Mo^{6+} oxidation state and then there are no electrons in the Mo 4*d* orbitals. Thus MoO_3 valence band consist a high intensity peak at 4.2 eV, which is due to the occupied O 2p orbital and the valence band onset (VB_{onset}) is at 2.7 eV below the E_F. Near E_F features are enlarged and plotted in the inset of Fig. 4.3b to show the fine changes due to oxidation of Mo^{4+} to Mo^{5+} and Mo^{6+}. A broad feature observed after 4 h O_2 treatment, compared to MoO_2 features, unambiguously identifies the co-existence of Mo^{4+} and Mo^{5+}. Mo^{5+} content increased after 6 h treatment, followed by further oxidation to MoO_3 at higher O_2 treatment times. Observation of Mo^{5+} content and stabilization of the same on the surface is very important, as it affects the material performance for many electronic applications, such as optoelectronics, sensors. It is also to be noted that 1.1 eV feature was remain observed even after 12 and 16 h O_2 treatment. This is attributed to the mid-gap states between VB and E_F; similar observation was reported in the literature for α-MoO_3.[30]

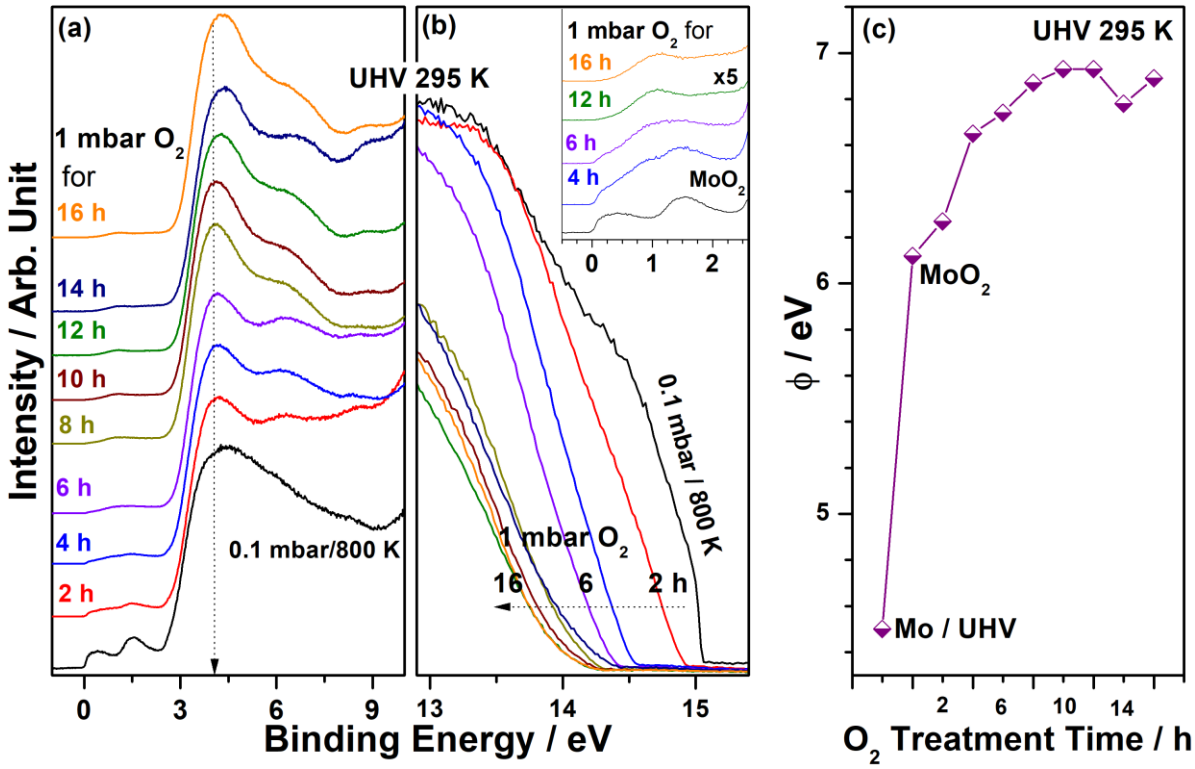

Figure 4.3: (a) Time dependent evolution of Mo oxidation from MoO_2 to MoO_{2+x} at 1 mbar/700 K; however NAPUPS spectra recorded at UHV/295 K. First spectrum shown in black colour trace is recorded at 0.1 mbar O_2 at 800 K, which is the same spectrum given in Fig. 1a. (b) Enlarged views of the offset in electron emission to measure the ϕ changes, and (c) the ϕ changes observed during Mo oxidation to MoO_3. x-axis corresponds to 700 K/1

mbar O_2 treatment time in h. Inset in panel (b) is the enlarged view of near Fermi level features of panel (a); except MoO_2, other spectral features are multiplied by a factor of 5.

The changes in the secondary electron cut off with increasing MoO_3 layers is plotted in Fig. 4.3b. A shift in the secondary electron cut off towards lower BE was observed indicating an increase in the ϕ up to 10 h treatment. At least 0.6 eV shift in the ϕ was observed from the initial surface layers (after 2 h treatment) to complete MoO_3 ($\geq$10 h treatment). Fig. 4.3c shows the systematic ϕ changes from Mo metal at 295 K/UHV to MoO_3, after several hours of O_2 treatment at 1 mbar/700 K. It was also found that ϕ depends on the extent of MoO_3 formation. ϕ tends to increase with more MoO_3 on the surface; after about 8 h treatment and above, ϕ remains constant. This indicates an increase in the thickness of MoO_3 layers >8 h O_2 treatment at 1 mbar/700 K. Initially at UHV/295 K, Mo metal exhibits a ϕ of 4.5 eV, which is in agreement with the value reported (4.4 eV) in the literature.[15] A large increase in the ϕ to 6.2 eV was observed on the formation of MoO_2 layers at 0.1 mbar O_2 at 700-800 K. Thereafter due to prolonged oxidation at 1 mbar/700 K, ϕ increases to 6.9 eV for MoO_3 and this final ϕ is the same as that of earlier reports.[15,32]

4.2.3. Mo + O_2 Interaction: pressure and temperature dependent NAP-XPS studies

Core level spectra were also recorded along with the NAPUPS and the results basically support conclusions derived from NAPUPS. Figures 4.4a and 4.4b shows the Mo 3*d* and O 1*s* spectra, respectively, at different oxygen pressures and temperatures. First spectrum recorded at UHV/295 K shows the typical spin-orbit doublets for metallic Mo $3d_{5/2}$ and $3d_{3/2}$ core levels at binding energies 227.9 and 231.1 eV, respectively. Surprisingly, no change in the Mo 3*d* spectrum was observed for an increase in the O_2 pressure to 0.1 mbar. A good change observed in NAPUPS spectrum under the same condition (Fig. 4.1a) is attributed to the low probing depth of UPS; since XPS probing depth is much larger (8-9 nm),[33] surface-only information is averaged out. However, at 600 K/0.1 mbar O_2 shows the onset of surface oxidation; metal core levels shows broadened and asymmetric features along with a low intensity and broad feature at high BE (235 eV). An increase in temperature to 800 K/0.1 mbar pressure dramatically changed the surface nature. Metallic Mo feature decreased substantially in intensity; however, intense features are observed for Mo^{4+} (appeared at 229.1 eV) along with significant amount of Mo^{6+} (232.5 eV).

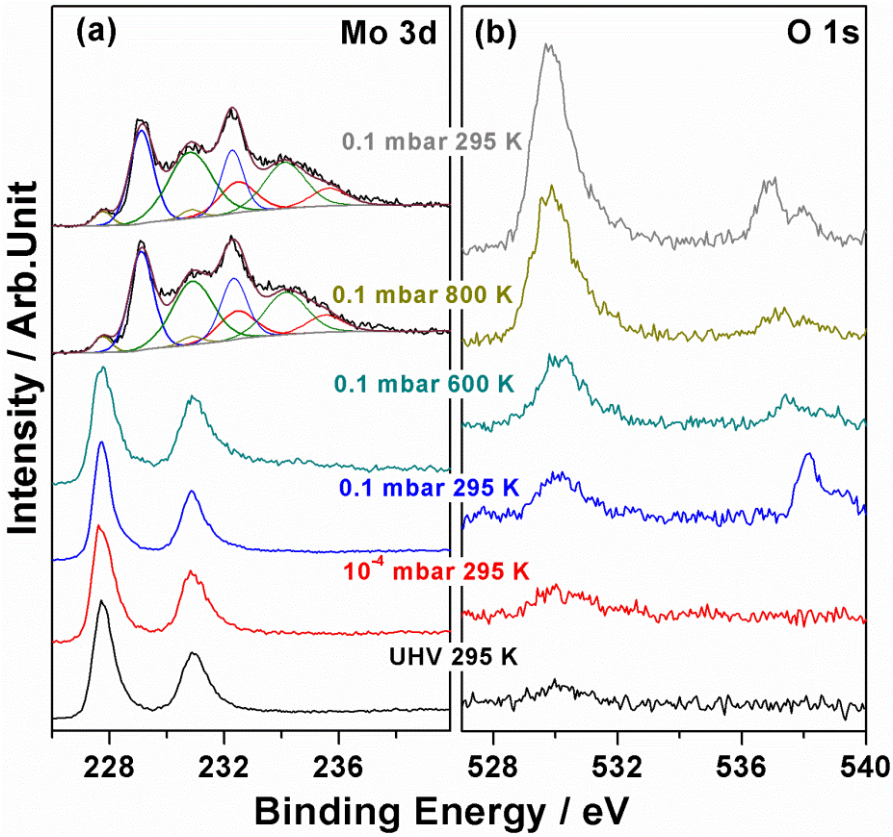

Figure 4.4: NAPXPS spectra recorded for (a) Mo 3d, and (b) O 1s core levels during Mo oxidation from metal to MoO_x as a function of pressure and temperature.

Last two spectra were deconvoluted to show the presence of various Mo oxidation states, especially Mo^{5+}. Even after O_2 treatment at 0.1 mbar/800 K, a small percentage (4.3 %) of metallic Mo was observed; this reiterates the sluggish oxidation, likely due to slow diffusion of oxygen atoms into the subsurface layers. Although the onset of bulk oxidation occurs, it is well within the probing depth of NAPXPS. Above treatment increased the extent of Mo^{4+} oxidation (38.4 %) predominantly at the cost of metallic Mo. This observation hints the oxidation of Mo-metal to MoO_2 in the first step followed by oxidation to MoO_3 after prolonged O_2 treatment. Mo^{6+} content increased to 15.7%. Interestingly Mo^{5+} content observed is relatively high (41.6 %) than other oxidation states. It may be possible that Mo^{5+} on the surface can be oxidized easily to Mo^{6+} but not at the subsurfaces due to its equilibrium with MoO_3 and MoO_2 layers. According to the Mo-O phase diagram, MoO_3 cannot be in equilibrium with Mo or MoO_2, rather O:Mo ratio changes at higher depths; this leads to different MoO_x layers stacked, starting from highest oxidized (MoO_3) on the surface to lower (MoO_2) in the bulk with Mo_2O_5 in between.[34] A very slow oxidation kinetics may be expected

due to high ϕ difference (~2.5 eV; Fig. 4.3c) between Mo metal to MoO_3. A ϕ difference of 0.8 eV observed between MoO_2 and MoO_3 (Fig. 4.3c) also underscores the direct oxidation of Mo^{4+} to Mo^{6+} is difficult and underscores the necessity of intermediate (Mo^{5+}) oxidation state. Greiner et al.[35] observed that, at the metal-oxide interface, metal contacts can reduce the MoO_3 due to charge transfer from the metals E_F into the conduction band of the MoO_3. Nevertheless, small but definite metallic feature observed, after the last treatment, underscores the oxidation is within the XPS probing depth of 8-9 nm. NAPUPS shows complete oxidation to MoO_3 in shorter time is due to low probing depth of 1-2 nm. It is likely that MoO_3 is preferentially formed on the surface followed by MoO_2 layers with metallic Mo still present at the subsurface layers and bulk.

O 1s core level spectra were also recorded during oxidation. As shown in Fig. 4.4b, no oxygen feature was observed at UHV/295 K, reiterates the surface purity of Mo foil. Then oxygen pressure was gradually increased from 10^{-6} mbar to 0.1 mbar at 295 K temperature. Even at a pressure 10^{-6} mbar, a broad and low intensity O 1s peak was observed at 530 eV; intensity of this feature increased with pressure and temperature. O 1s core level peak is attributed to the lattice oxygen of MoO_x. A doublet for O 1s core level feature for gas-phase oxygen was observed at 538-539 eV at a pressure of 0.1 mbar. It is very interesting to observe the shift in BE of this feature with increasing severity of the treatment (in terms of temperature and pressure). BE of this feature gradually decreases to 536.7-537.5 eV after an extended treatment at 1 mbar/700 K. BE shift reiterates the change in ϕs, and it is in good correspondence with the changes observed in NAPUPS.[36] It is also to be noted that the lattice oxygen feature at 530±0.2 eV largely unchanged and remain observed at the same BE, while the ϕ and gas-phase O 1s features displays changes with each treatment.

4.2.4. Mo + O_2 Interaction: time dependent NAP-XPS studies at 1 mbar and 700 K

Core level NAPXPS data recorded during prolonged oxidation at different time intervals and representative results are given in Fig. 4.5. Progressive oxidation was observed in several stages. Mo foil oxidizes to distinct Mo^{6+} (29.8 %) after treatment at 1 mbar O_2 pressure at 700 K for 2 h, along with Mo^{4+} (29.3) and Mo^{5+} (37.9) peaks. Small amount of Mo-metal (3%) is still present and corresponding Mo $3d_{5/2}$ peak was observed at 227.9 eV, suggesting the oxidation has not propagated beyond the XPS probing depth of 8-9 nm. On increasing the treatment time to 4 h, the Mo^{4+} content is decreased to 22 %; however, this is compensated with an increase in Mo^{6+} content to 39.6 %, but Mo^{5+} is retained largely. From

the area of the V and VI oxidation states, it can be discerned that very few layers are oxidized to higher oxidations states.

Oxidation Conditions	**Mo (0)**	**Mo (4+)**	**Mo (5+)**	**Mo (6+)**
0.1 mbar 800 K	4.3	38.4	41.6	15.7
UHV 295 K	3.8	34.7	45	16.5
1 mbar/2 h	3.0	29.3	37.9	29.8
1 mbar/4 h	2.4	22	36	39.6
1 mbar/8 h	1.5	10.2	22.8	65.5
1 mbar/12 h	0	3.3	17.6	79.1
1 mbar/16 h	0	0	8	92

Table 4.1: Summary of the Mo metal and its oxide percentages at various stages of oxidation.

An additional treatment of Mo-surface to 8 h lead to a decrease in the percentage of Mo^{4+} to 10.2 and Mo^{5+} to 22.8, while Mo^{6+} increased significantly to 65.6. Decrease in Mo^{5+} can be discerned by two observations: (1) a progressive decrease in the intensity of the feature around 232 eV. (2) Onset of a deep energy valley between spin-orbit doublets of Mo^{6+}, which is not observed below 8 h treatment. These two points signify that more Mo^{5+} was present at the interface; however, due to continuous oxidation at 1 mbar/700 K, thickness of the MoO_3 layers increases at the expense of lower oxidation states. Metallic Mo completely disappears and marginal amount of MoO_2 present after 12 h O_2 treatment at 700 K/1 mbar. Indeed, Mo-oxidation to the highest oxidation state (MoO_3) occurs systematically from MoO_2 through Mo^{5+}. This indicates the intermediate layers between MoO_3 and MoO_2 is likely to be Mo^{5+} with oxygen vacancy sites, which is the driving force for oxidation to MoO_3.

After 12 h treatment, the area of the Mo^{6+} increased substantially to 79.1 %, while the Mo^{4+} and Mo^{5+} peaks show marginal (3.3 %) and low intensity (17.6 %). Asymmetric broadening of Mo^{6+} spin-orbit doublets on the low BE side demonstrates the presence of Mo^{5+}. After 16 h treatment, Mo^{5+} content (8 %) on the surface decreased due to an increase in the thickness of MoO_3 and a sharp Mo^{6+} features are observed. With increasing MoO_3 thickness, the regular Mo^{6+} state becomes dominant and the relative content of Mo^{5+} state decreases, indicating that Mo^{5+} mostly exists at the interface due to the electron transfer from the MoO_2 to MoO_3 in the interface region. When the MoO_3 thickness increases more than 5 nm, the Mo 3d core-level spectrum is dominated by the Mo^{6+} feature (92 %).

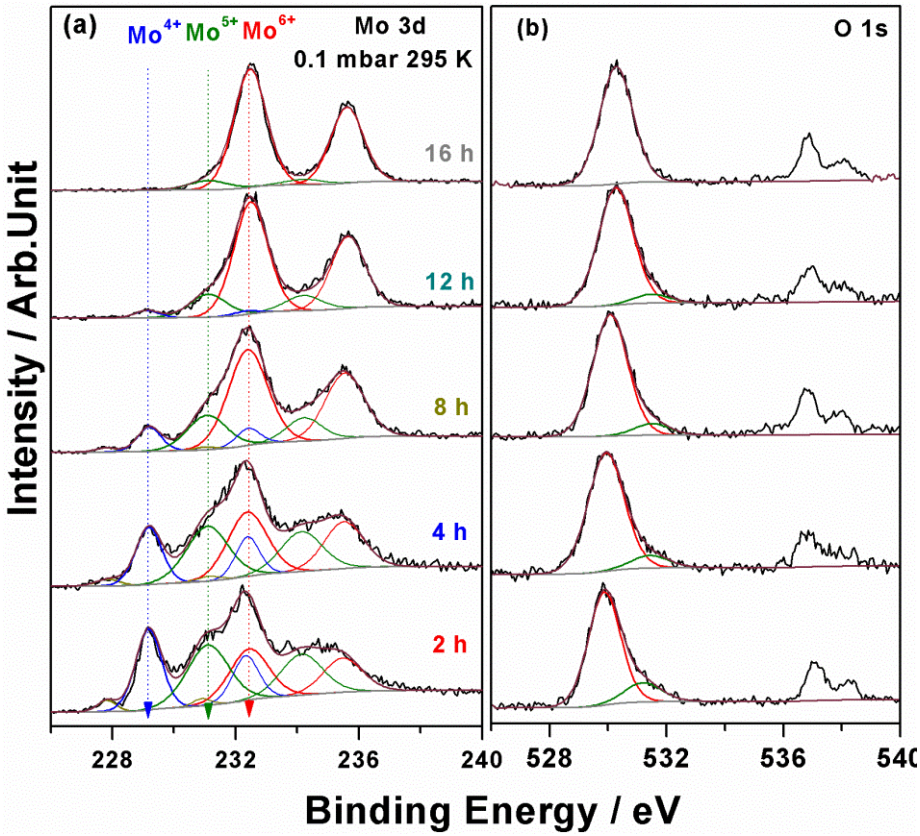

Figure 4.5: NAPXPS spectra obtained as a function of oxygen treatment time from a) Mo 3d and b) O 1s core levels on prolonged oxygen treatment from predominant MoO_2 to MoO_3.

A gradual decrease in Mo^{4+} content followed by Mo^{5+} with increasing treatment time underscores the oxygen insertion occurs from the top layers to the bottom layers as shown in table Table. 4.1. Very likely, diffusion of oxygen atoms could be a rate limiting factor for the bulk oxidation. Under the present experimental conditions, long hours of oxygen treatment time is required for the oxidation of Mo^{5+} at the interface hints that Mo^{5+} could be more stable and simply cannot be considered as a typical intermediate. Fast oxidation kinetics of Mo^{5+} should lead to more Mo^{6+}, which is not the case. It may be possible that Mo^{5+} on surface can be oxidized easily, but not at the interface in the sub-surfaces and sandwiched between MoO_3 and MoO_2 layers. Partly this could be due to slow diffusion of oxygen atoms into the deeper layers. Oxygen vacancies are known to diffuse from bulk to the surface layers in ceria and hence fast oxidation kinetics occurs; however, it is the reverse with MoO_x and oxygen have to diffuse for oxidation.[37,38] This suggests that MoO_x may not be used as oxygen storage material.

O 1s core level spectra are shown in Figure 4.5b. Upon O_2 exposure at 1 mbar and 700 K for 2 h, a high intense, but asymmetric, O 1s peak was observed at 529.9 eV. This is

attributed to the lattice oxygen of MoO_x along with a peak at 531.3 eV; latter feature is likely due to the oxygen associated with defect or vacancy sites present on the surface. However, the latter feature is observed with low intensity and gradually decreased with increasing O_2 treatment time. Doublet for gas phase oxygen was observed at 537 and 538.3 eV. With increasing exposure time to 16 h, a symmetric feature evolves and observed at 530.3 eV due to MoO_3 lattice oxygen. Defect oxygen content gradually decreases and disappears after 16 h treatment. Doublet features for gas-phase oxygen is broadened and shifted to lower BE between 4 and 12 h treatment. This observation hints the heterogeneity of the surface layers, especially due to various oxidation states within the XPS probing depth. Sharp feature observed after 16 h treatment underscores the surface with predominant MoO_3 content. It is also to be mentioned that the energy gap between O 1s feature of the lattice oxygen and gas-phase oxygen decreases from 7.4 to 6.9 eV, after 2 and 16 h treatment, respectively. Change in BE of the gas-phase and lattice oxygen demonstrates a changes in the electronic nature of the surface; possibly the band-bending between different oxidation states changes to predominant MoO_3 band. Unlike Mo 3d core levels, oxygen bound to different oxidation states of Mo seem to appear at the same BE. This indicates the nature of Mo-O remains similar, irrespective of Mo oxidation state.

X-ray valence band spectra were also recorded with Al Kα photons and the results are shown in Figure 4.6. This is to ensure the assignments made for earlier results are correct and reconfirm the energy positions of O 2p and Mo 4d orbitals. It is to be mentioned that photoionization cross section of Mo 4d (0.0046 Mb) and O 2p (0.00024 Mb) orbitals are twenty times different with Al Kα photon, while the same with He-I is just two times different.[39] This factor allows to identify energy of different orbitals and their contribution precisely to the VB.[40,41] Intense and broad VB features observed for metallic Mo between 1-6 eV at UHV/295 K is attributed to the Mo 4d and 5s orbitals.[42] Corresponding metallic Mo 3d core level features are observed in XPS. After exposure to oxygen at 0.1 mbar/700 K, FWHM of Mo 4d features decreases and a broad and intense O 2p band was observed between 4-10 eV. Comparison of the energy of metallic Mo 4d and O 2p band hints a good overlap in energy of those orbitals and signifies the covalent hybridization between them. Large intensity observed at 1-3 eV is due to the large probing depth of XPS-VB due to high kinetic energy associated with VB electrons; however, the oxidation is limited to surface layers. Mo 3d core level shows predominant Mo^{4+} features with minor Mo, Mo^{5+} and Mo^{6+} features (Fig. 4.4). On further oxidation at 1 mbar pressure and 700 K for 4, 8, 16 h, a systematic changes

was observed. Mo 4d feature observed due to a mixture of Mo, Mo^{4+} and Mo^{5+} up to 8 h treatment in VB and this feature decreased in intensity with increased severity of treatment. However, Mo 4d feature disappeared after 16 h treatment. Intensity reduction of Mo 4d feature from 4 to 8 h treatment indicates increasing oxidation of Mo^{4+} and Mo^{5+} to Mo^{6+}. No Mo 4d feature was observed after 16 h treatment suggests the complete oxidation of surface layers, at least within the XPS probing depth. The ratio of O 2p/ Mo 4d (Fig. 4.6a) feature keeps increasing with increasing treatment time reiterates a gradual oxidation from surface to bulk layers. No Mo 4d feature appears after 16 h treatment in the VB and it is mainly made up of O 2p states in the range of 4-10 eV.

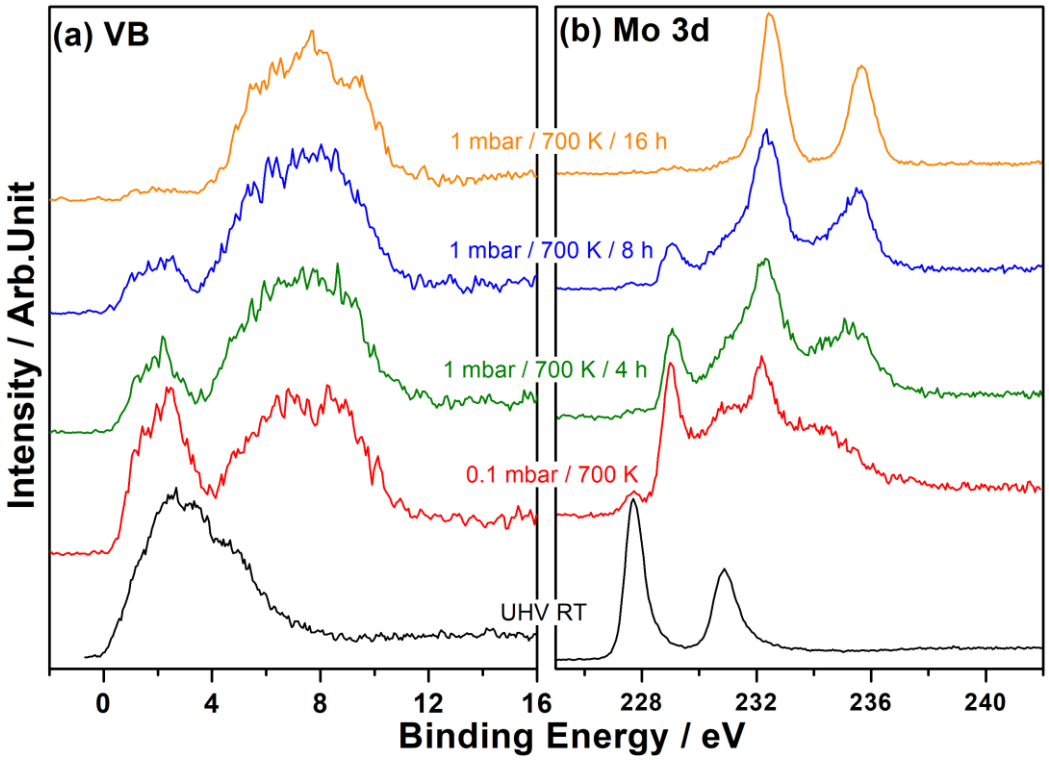

Figure 4.6: (a) XPS-VB and (b) Mo 3d core level studies of Mo oxidation from metal to MoO_x under different conditions. All spectra were recorded at UHV/RT, after the treatment mentioned in the figure.

4.2.5. MoO_3 + H_2 Interaction: pressure and temperature dependent NAP-UPS studies

It is well known that MoO_3 and MoO_2 can be interconverted; but what is not known are the changes in the electronic structure during reduction with hydrogen and the role of Mo^{5+}. In-situ generated MoO_3 was subjected to reduction at different hydrogen pressures and temperatures and the NAPUPS results recorded are shown in Figure 4.8. UPS spectrum

recorded at UHV/295 K shows VB maxima at 2.7 eV, along with three distinct features at 4.5, 6.5 and 8.8 eV. To know these features, we have carried out the time dependent sputtering experiment on the in-situ generated MoO_3 film (corresponding to 16 h spectrum shown in Fig. 4.3a) and the result obtained from NAPUPS, XPS spectra are shown in Figure 4.7. After five minutes of sputtering, NAPUPS result (see Fig. 4.7a) shows highly broadened features at 4.5, 6.5 and 8.8 eV; however, the doublet observed near E_F is very typical for the formation of predominant MoO_2. It is to be noted that in MoO_2 only one type of oxygen exists and one can expect the disappearance of these three features. Those expected changes reflect along with Mo^{5+} in the XPS spectra (Fig. 4.7b). There are three non-equivalent O-sites are present in α-MoO_3; singly, doubly and triply coordinated oxygen, indicates the oxidation of Mo led to α-MoO_3 in the present study.[2,5] Even at 10^{-4} mbar H_2 pressure at 295 K, intensity enhancement was observed between 0-2 eV together with small intensity increase in the O feature at 6.5 eV. This might be due to adsorption of H_2 on that particular type of oxygen.

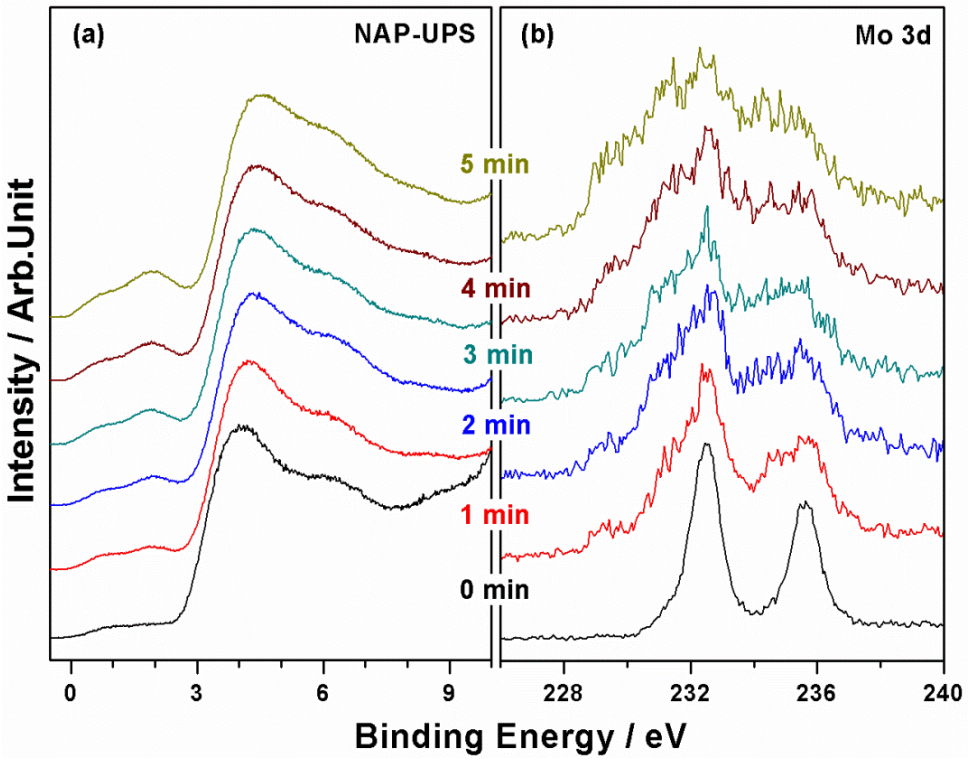

Figure 4.7: (a) UVPES, and (b) Mo 3d core level spectra recorded after sputtering of MoO_3 surfaces at RT for different time intervals.

Hydrogen pressure was gradually increased to 0.1 mbar pressure at 295 K and the spectrum was recorded. At 0.1 mbar pressure, narrow H_2 vibrational features were observed

at 10.2 eV hinting the surface homogeneity. Hydrogen vibrational features from pure H_2 appeared between 10.7 and 13 eV. However, compared to the reference gas-phase H_2 spectrum, a 1.1 eV low BE shift was observed for H_2 on the MoO_3 surface. This shift is attributed to the surface potential exerted by MoO_3 surfaces. However observation of all features of hydrogen, and without any broadening, suggest the surface is fully homogeneous in character. A careful analysis of the results obtained at increasing H_2 pressure at 295 K shows the disappearance of the feature at 8.8 eV and intensity enhancement observed with 6.5 eV feature. Further a change in ϕ (1.1 eV) is evident from the UPS cut-off and suggests a change in the nature of surface, even at 295 K, which is quite surprising.

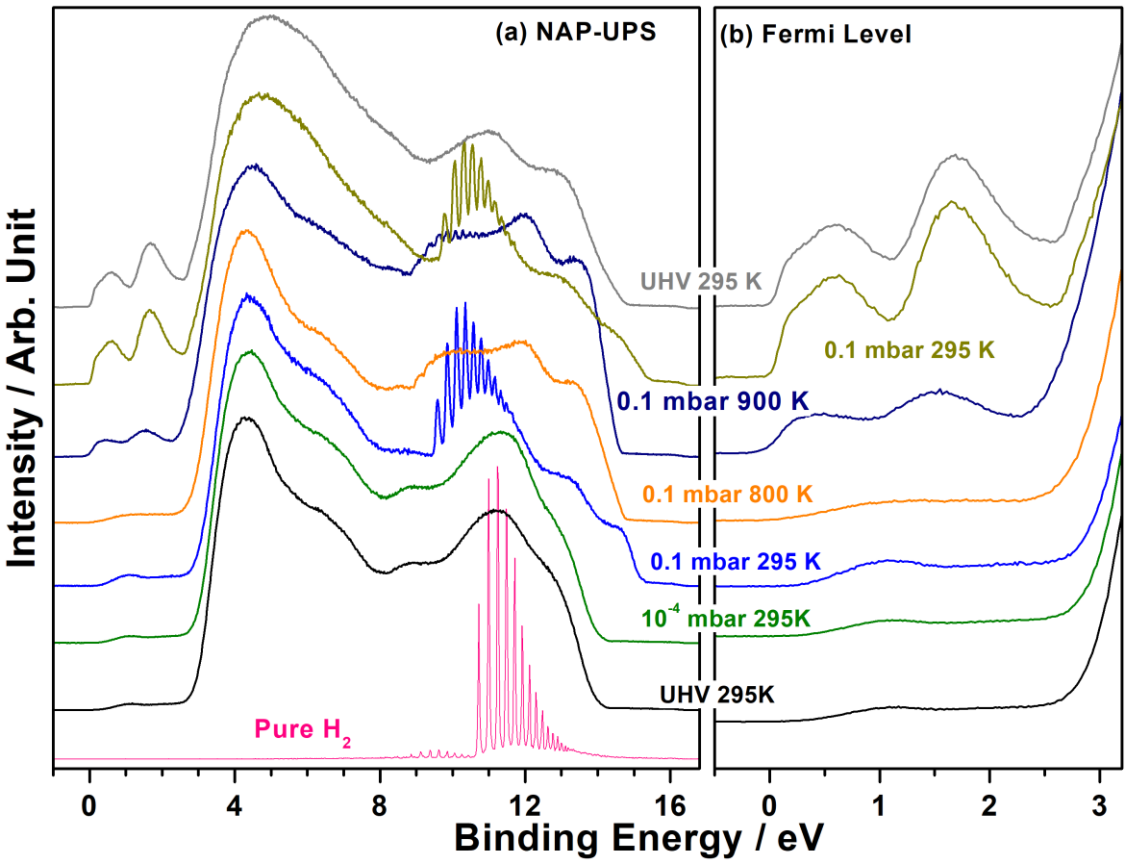

Figure 4.8: a) NAPUPS spectra recorded during the reduction of MoO_3 carried out with different H_2 pressure and temperatures. (b) Enlarged fermi level features are shown.

On incresing the temperature gradually to 800 K/0.1 mbar H_2, a decrease in the intensity of the vibrational features observed and it is attributed to thermal broadening as well as surface heterogeneity. It is to be mentioned that the H_2 gas was pre-heated to the measurement temperature by passing through heated gas-doser;[43,44] this helps to minimize the temperature fluctuations on the surfae. An onset of partial reduction of MoO_3 is evident from

the features observed between 0-2 eV. On increasing the temperature to 900 K, two distinct features are observed at 0.6 and 1.6 eV due to the formation of MoO_2. Further increase in Mo 4d features was observed at 950 K (result not shown). At the same time, O 2p features observed at 6.5 and 8.8 eV at lower temperatures disappered due to complete reduction of α-MoO_3 layered structure to MoO_2. Complete reduction of surface layers to MoO_2 is further supported by the observation of narrow vibration features of H_2. Features observed at 1.1 eV is attributed to the singly occupied electrons in the Mo 4d orbital of MoO_{3-x}. After H_2 treatment at 0.1 mbar/950 K, features observed at 0.6 and 1.6 eV are due to the well screened (Mo $4d^2\underline{L}$) and unscreened Mo^{4+} final state (Mo d^1) of MoO_2, respectively.[45] Shift in the singly occupied electron binding energy from 1.1 (MoO_{3-x}) to 1.6 eV (MoO_2) can be expected due to change in geometry as well as the nature of Mo-O bond.

Offset values of the NAPUPS shows the decrease in the ϕ from MoO_3 to MoO_{3-x} due to reduction. The ϕ of MoO_3 is observed to be 6.9 eV; however, after reduction at UHV/295 K ϕ decreases to 6.1 eV. Even when the pressure was increased to 1 mbar H_2 at 900 K and kept for 6 hours, no further reduction (to metal) was observed and only MoO_2 features were observed. The intensity of the features at 0.6 and 1.6 eV increased further and decreased in the ϕ of the sample observed. It is also to be noted that VB broadened with increasing H_2 pressure and temperature.

Pure H_2 vibrational features observed for H_2 on MoO_3 surface at 0.1 mbar and various temperatures are shown in Fig. 4.9. The peak fitting have been carried out by taking pure gas phase spectra as a reference. When we compare with pure H_2 gas vibrational features, there are some changes observed in it on MoO_3 surface at 0.1 mbar/295 K. Vibrational features was shifted to lower binding energy, and a marginal increase in FWHM was observed; however peak symmetry is retained. Further increase in temperature to 800 K lead to a large decrease in the intensity of vibrational features with a marginal change in BE; this is due to highly heterogeneous nature of the surface (data not shown). At 900 K, vibration features were shifted to lower binding energy; however, each peak split into two peaks, which indicates that two different types of species are present on the surface. On cooling to 295 K, vibrational features are resolved, shifted to higher binding energy, and indicating the homogeneity of the surface.

4.2.6. Mo + H_2 Interaction: pressure and temperature dependent NAP-XPS studies

Mo 3d and O 1s core level spectra were also recorded during H_2 treatment along with the NAPUPS and the results obtained are shown in Fig. 4.10. With increasing pressure from UHV to 0.1 mbar at 295 K, no significant change was observed; however, a small amount of Mo^{5+} was observed at 231.0 eV. On incresing the temperature gradually to 800 K at 0.1 mbar, small quantity of Mo^{4+} was observed at 229.1 eV, which suggests the onset of reduction. Simultaneoulsy, a significant increase in Mo^{5+} was also observed. Further increase in temperature to 900 K lead to an increase in Mo^{4+} and Mo^{5+} content, and a significant decrease in the intensity of Mo^{6+} was observed. On further increasing the pressure to 1 mbar at 900 K for 6 h, all three oxidation states (4+, 5+ and 6+) are observed; however, no metal feature was observed.

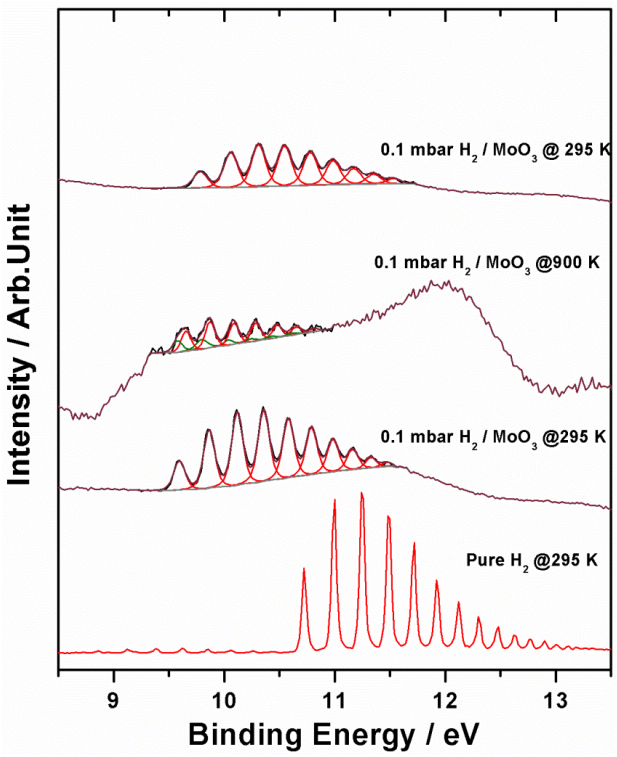

Figure 4.9: Deconvolution carried out for hydrogen gas vibrational features recorded at 0.1 mbar pressure for pure H_2 and H_2 on MoO_3 surface at different temperatures.

This spectrum resembles to that of Fig. 4.4a (top trace) recorded under oxidizing conditions, except for metallic Mo. Mo^{5+} and Mo^{6+} features were not observed in Fig. 4.8 due to low probing depth of UPS. This reiterates that the reduction also proceeds from the top to the subsurface and bottom layers. However, by manipulating the pressure and temperature, it is

possible to achieve the desired combination of oxidation states of Mo on the surface. By retaining Mo^{5+} on the surface and interfaces, electrochemical and catalytic activity can be tuned to required activity and/or selectivity. More work needs to be carried out in this direction. Except for a minor line broadening and shift to low BE by 0.3 eV, no other changes are observed with O 1s core level.

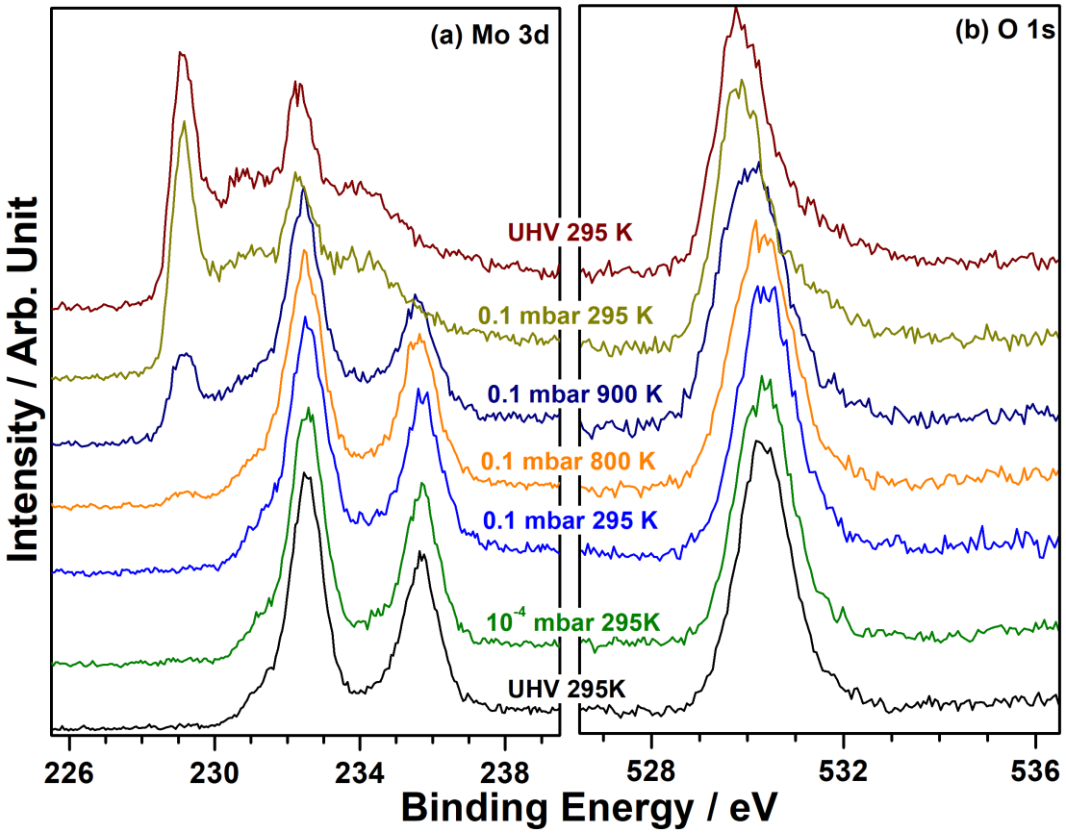

Figure 4.10: NAPXPS spectra of a) Mo 3d b) O 1s during in-situ MoO_3 reduction.

4.2.7. Surface work function changes from Mo to MoO_3

To study the changes in the ϕ of MoO_x during the oxidation of Mo, especially under reactive conditions, we have chosen oxygen gas as a probe molecule to measure the changes in the ϕ (Figure. 4.11). Initial spectrum of O_2 gas-phase (without Mo and sample holder) features are taken as a reference and change in the ϕ is measured with reference to the above. At the same time, we measured the ϕ of MoO_x at different stages of oxidation as described earlier from the offset value of NAPUPS spectrum at UHV 295 K and the results are plotted in Fig. 4.11.

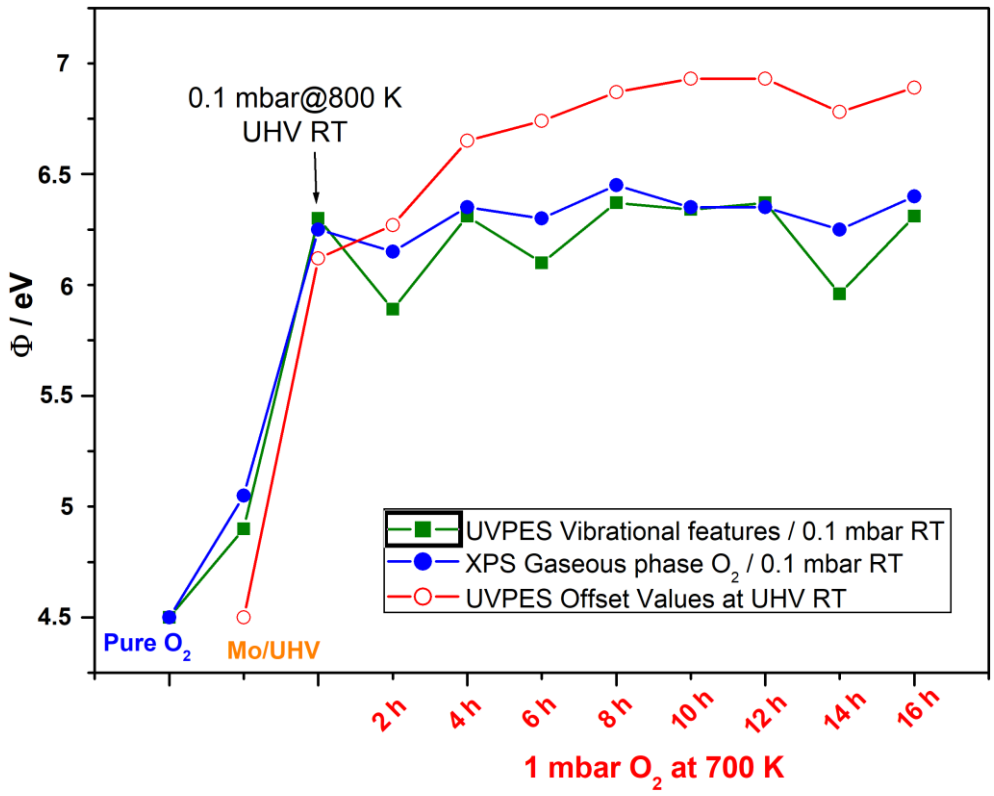

Figure 4.11: Change in work function during oxidation from Mo metal to MoO_3 at different stages of oxidation at RT.

Generally, there is a good correspondence between all three methods of ϕ measurements and the difference was found to be within 0.5 eV. This difference may be due to changes in the surface dipole of Mo in 0.1 mbar O_2 environment, whereas some of the ϕ values obtained from the spectra were recorded at UHV. ϕ measured from UVPES offset values (red trace in Fig. 4.11) shows the most correct values and they are in good correspondence with literature reports.[30] An interesting observation is the change in ϕ during the transition of MoO_2 to MoO_3, which occurs during 1 mbar O_2 treatment at 700 K in the first six hours (red trace in Fig. 4.11). In fact, the charge transfer and dipole formation at the interface leads to a significant difference in ϕ values. Further the resolution of UVPES and XPS also contributes to the difference to a significant extent. Our earlier studies also reflect such changes for different systems, such as Ag, Si, Cu, Co_3O_4, Pd, and Ceria-zirconia.[28,29,41,44,46-48]

4.3. Conclusion

In summary, we have examined the $Mo/MoO_2/Mo_2O_5/MoO_3$ interfaces using NAPUPS and NAPXPS methods by controlled oxidation of the Mo foil at near ambient pressures (1 mbar) and temperatures (up to 900 K). A large increase in the ϕ (2.4 eV) was

observed from Mo metal to MoO_3 with valence band offset spectrum; very similar changes in the ϕ was obtained with the vibrational features of gas phase oxygen in both NAPUPS and with NAPXPS O 1s spectrum. Initially at the interface of MoO_2/MoO_3 during oxidation of Mo foil, Mo^{5+} feature was observed below the Fermi level (1.1 eV) of NAPUPS spectrum and its intensity decreased while increasing the extent of the MoO_3 formation. At the same time, considerable increase in the ϕ (0.6 eV) was observed with increasing extent of MoO_3 layer formation. This is well supported by the x-ray valence band as well as with NAPXPS. By controlling the thickness, it is possible to tune the conductivity and can alter the ϕ of the α-MoO_3; information derived from the present study is likely to be used for broad range of applications, such as optoelectronics.

Reduction of MoO_3 to MoO_2 in H_2 was also measured with NAPUPS and NAPXPS. Reversible changes observed between MoO_2 oxidation in O_2 and MoO_3 reduction in H_2 underscores the propagation of oxidation and reduction occurs from top to bottom layers. An important observation is the significant stability of Mo^{5+} oxidation state found at the surfaces and interfaces of MoO_2 and MoO_3 under oxidation and reduction conditions, respectively. Stability of the Mo^{5+} makes it as a special species, since bulk Mo_2O_5 is not known. Progressive changes in ϕ observed from MoO_2 and MoO_3 (and the reverse) is attributed to the role of Mo^{5+} at the interfaces. Even small amount of Mo^{5+} in the compounds would change the conductivity due to the Mo $4d^1$ electronic configuration; $4d^1$ electronic state occurs close to the conduction band minimum and E_F, and lead to an additional/impurity state, depending on the concentration. Mo^{5+} is expected to bring special features, such as redox, catalytic, electrochemical functions, which is yet to be exploited fully. By manipulating the reaction (redox) conditions, Mo^{5+} state can be made available for many applications such as optoelectronic devices, sensors. More work in this direction is desired.

4.4. References

(1) Kim, H.-S.; Cook, J. B.; Lin, H.; Ko, Jesse S.; Tolbert, Sarah H.; Ozolins, V.; Dunn, B. *Nat. Mater.* **2016**, *16*, 454-460.

(2) de Castro, I. A.; Datta, R. S.; Ou, J. Z.; Castellanos-Gomez, A.; Sriram, S.; Daeneke, T.; Kalantar-Zadeh, K. *Adv. mater.* **2017**, *29*. *No*.1701619.

(3) Bin, Y.; Liang, H.; Jing, Z.; Xiang, G.; Jiabin, W.; Yongliang, C.; Xu, X.; Bo, W.; Yat, L.; Jun, Z. *Adv. Mater.* **2016**, *28*, 6353-6358.

(4) Scanlon, D. O.; Watson, G. W.; Payne, D. J.; Atkinson, G. R.; Egdell, R. G.; Law, D. S. L. *J. Phys. Chem. C.* **2010**, *114*, 4636-4645.

(5) Guo, Y.; Robertson, J. *Appl. Phys. Lett.* **2014**, *105*, *No.* 222110.

(6) Kröger, M.; Hamwi, S.; Meyer, J.; Riedl, T.; Kowalsky, W.; Kahn, A. *Appl. Phys. Lett.* **2009**, *95*, *No*.123301.

(7) F. Cauduro, A. L.; dos Reis, R.; Chen, G.; Schmid, A. K.; Méthivier, C.; Rubahn, H.-G.; Bossard-Giannesini, L.; Cruguel, H.; Witkowski, N.; Madsen, M. *ACS. Appl. Mater. Interfaces* **2017**, *9*, 7717-7724.

(8) Vasilopoulou, M.; Douvas, A. M.; Georgiadou, D. G.; Palilis, L. C.; Kennou, S.; Sygellou, L.; Soultati, A.; Kostis, I.; Papadimitropoulos, G.; Davazoglou, D.; Argitis, P. *J. Am. Chem. Soc.* **2012**, *134*, 16178-16187.

(9) Peelaers, H.; Chabinyc, M. L.; Van de Walle, C. G. *Chem. Mater.* **2017**, *29*, 2563-2567.

(10) Preethi, L. K.; Mathews, T.; Nand, M.; Jha, S. N.; Gopinath, C. S.; Dash, S. *Appl. Catal., B* **2017**, *218*, 9-19.

(11) K., P. K.; S., G. C. *ChemCatChem* **2016**, *8*, 3294-3311.

(12) Patra, K. K.; Bhuskute, B. D.; Gopinath, C. S. *Sci. Rep.* **2017**, *7*, *No.*6515.

(13) Patra, K. K.; Gopinath, C. S. *J. Phys. Chem. C* **2018**, *122*, 1206-1214.

(14) Qadir, K.; Joo, S. H.; Mun, B. S.; Butcher, D. R.; Renzas, J. R.; Aksoy, F.; Liu, Z.; Somorjai, G. A.; Park, J. Y. *Nano Lett.* **2012**, *12*, 5761-5768.

(15) Greiner, M. T.; Chai, L.; Helander, M. G.; Tang, W.-M.; Lu, Z.-H. *Adv. Funct. Mater.* **2012**, *22*, 4557-4568.

(16) Butler, K. T.; Crespo-Otero, R.; Buckeridge, J.; Scanlon, D. O.; Bovill, E.; Lidzey, D.; Walsh, A. *Appl. Phys. Lett.* **2015**, *107*, *No.*231605.

(17) Rajambal, S.; Sivaranjani, K.; Gopinath, C. S. *J. Chem. Sci.* **2015**, *127*, 33-47.

(18) Liu, L.; Zhang, W.; Guo, P.; Wang, K.; Wang, J.; Qian, H.; Kurash, I.; Wang, C.-H.; ; Xu, F. *Phys. Chem. Chem. Phys.* **2015**, *17*, 3463-3469.

(19) Datta, R. S.; Haque, F.; Mohiuddin, M.; Carey, B. J.; Syed, N.; Zavabeti, A.; Zhang, B.; Khan, H.; Berean, K. J.; Ou, J. Z.; Mahmood, N.; Daeneke, T.; Kalantar-zadeh, K. *J. Mater. Chem. A.* **2017**, *5*, 24223-24231.

(20) Smith, M. R.; Ozkan, U. S. *J. Catal.* **1993**, *141*, 124-139.

(21) Remediakis, I. N.; Kaxiras, E.; Chen, M.; Friend, C. M. *J. Chem. Phys.* **2003**, *118*, *No.*6046.

(22) Gao, J.; Zheng, Y.; Jehng, J.-M.; Tang, Y.; Wachs, I. E.; Podkolzin, S. G. *Science* **2015**, *348*, 686-690.

(23) Kuwahara, Y.; Furuichi, N.; Seki, H.; Yamashita, H. *J. Mater. Chem. A.* **2017**, *5*, 18518-18526.

(24) Bai, H.; Yi, W.; Li, J.; Xi, G.; Li, Y.; Yang, H.; Liu, J. *J. Mater. Chem. A.* **2016**, *4*, 1566-1571.

(25) Dubey, A.; Kolekar, S. K.; Gopinath, C. S. *ChemCatChem* **2016**, *8*, 3650-3656.

(26) Silversmit, G.; Depla, D.; Poelman, H.; Marin, G. B.; De Gryse, R. *J. Electron Spectrosc Relat. Phenom.* **2004**, *135*, 167-175.

(27) Indlekofer, G.; Oelhafen, P.; Krieg, J.; Lapka, R.; M. Gubler, U.; J. Güntherodt, H.; L. Moruzzi, V.; R. Khan, H.; Lüders, K. *Phys. B: Condens. Matter* **1985**, *58*, 293-297.

(28) Ghosalya, M. K.; Jain, R.; Reddy, K. P.; Gopinath, C. S. *J. Phys. Chem. C.* **2018**, *122*, 4331-4338.

(29) Reddy, K. P.; Jain, R.; Ghosalya, M. K.; Gopinath, C. S. *J. Phys. Chem. C.* **2017**, *121*, 21472-21481.

(30) Greiner, M. T.; Helander, M. G.; Tang, W.-M.; Wang, Z.-B.; Qiu, J.; Lu, Z.-H. *Nat. Mater.* **2012**, *11*, 76-81.

(31) Shen, J.; Lee, H.; Valentí, R.; Jeschke, H. O. *Phys. Rev. B.* **2012**, *86*, *No.*195119.

(32) Du, Y.; Peng, H. Y.; Mao, H.; Jin, K. X.; Wang, H.; Li, F.; Gao, X. Y.; Chen, W.; Wu, T. *ACS Appl. Mater. Interfaces* **2015**, *7*, 11309-11314.

(33) Gholap, S. G.; Badiger, M. V.; Gopinath, C. S. *J. Phys. Chem. B.* **2005**, *109*, 13941-13947.

(34) Brewer, L.; Lamoreaux, R. H. *Bull. Alloy Phase Diagrams* **1980**, *1*, 85.

(35) T., G. M.; Lily, C.; G., H. M.; Wing-Man, T.; Zheng-Hong, L. *Adv. Funct. Mater.* **2013**, *23*, 215-226.

(36) Axnanda, S.; Scheele, M.; Crumlin, E.; Mao, B.; Chang, R.; Rani, S.; Faiz, M.; Wang, S.; Alivisatos, A. P.; Liu, Z. *Nano Lett.* **2013**, *13*, 6176-6182.

(37) Anjani, D.; K., K. S.; S., G. C. *ChemCatChem* **2016**, *8*, 2296-2301.

(38) Dubey, A.; Kolekar, S. K.; Gnanakumar, E. S.; Roy, K.; Vinod, C. P.; Gopinath, C. S. *Catal., Struct. React.* **2016**, *2*, 1-12.

(39) Yeh, J. J.; Lindau, I. *At. Data and Nucl. Data Tables* **1985**, *32*, 1-155.

(40) Mathew, T.; Shiju, N. R.; Sreekumar, K.; Rao, B. S.; Gopinath, C. S. *J. Catal.* **2002**, *210*, 405-417.

(41) Ghosalya, M. K.; Reddy, K. P.; Jain, R.; Roy, K.; Gopinath, C. S. *J. Chem. Sci.* **2018**, *130*, 6091-6100.

(42) Werfel, F.; Minni, E. *J. Phys. C: Solid State Phys.* **1983**, *16*, 6091.

(43) Roy, K.; Vinod, C.; Gopinath, C. S. *J. Phys. Chem. C* **2013**, *117*, 4717.

(44) Roy, K.; Gopinath, C. S. *Anal. Chem.* **2014**, *86*, 3683.

(45) Stoeberl, V.; Abbate, M.; Alves, L. M. S.; dos Santos, C. A. M.; Mossanek, R. J. O. *J. Alloys Compound.* **2017**, *691*, 138-143.

(46) Jain, R.; Dubey, A.; Ghosalya, M. K.; Gopinath, C. S. *Catal. Sci. Technol.* **2016**, *6*, 1746-1756.

(47) S., G. C.; Kanak, R.; Sankaranarayanan, N. *ChemCatChem* **2015**, *7*, 588-594.

(48) Jain, R.; Reddy, K. P.; Ghosalya, M. K.; Gopinath, C. S. *J. Phys. Chem. C.* **2017**, *121*, 20296-20305.

Chapter-5

Molybdenum Carbide Catalyst for the Reduction of CO_2 to CO: Surface Science Aspects by NAPPES and Catalysis Studies.

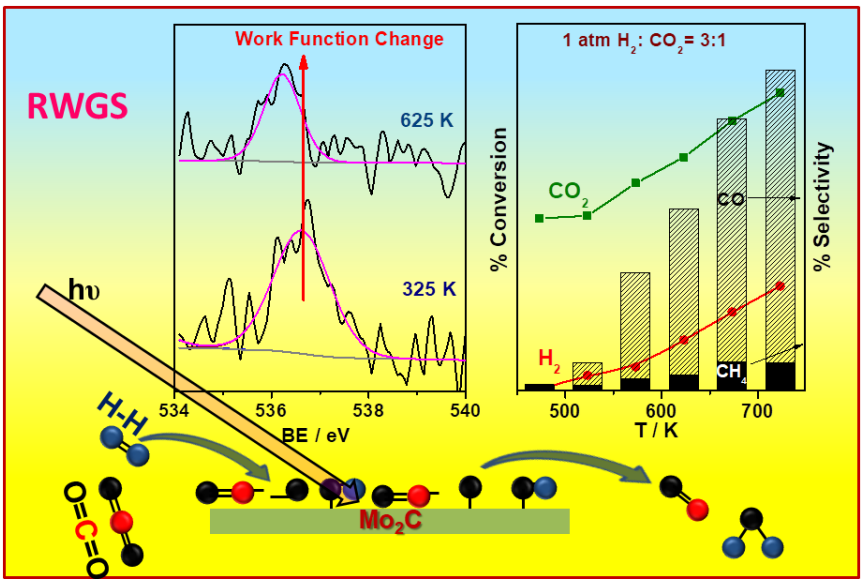

Part of this work has been submitted.[3]

[3]**Reddy, K. P.;** Dama, S.; Mhamane, N.B.; Ghosalya, M. K.; Chilukuri, S.; Gopinath, C. S., Molybdenum Carbide Catalyst for the Reduction of CO_2 to CO: Surface Science Aspects by NAPPES and Catalysis Studies. (Manuscript Submitted.).

5.1. Introduction

Ideal combustion of 12-16 g of any fossil fuel (coal, oil and natural gas) leads to energy and a minimum of 44 g of carbon dioxide (CO_2), which is added to atmosphere. It is high time that we, including politicians and bureaucrats, need to think on how to minimize the addition of CO_2 to atmosphere. Indeed, CO_2 is a greenhouse gas released into the atmosphere by burning fossil fuels from various applications and a prime source for global warming and ocean acidification etc.[1] Paris climate pact 2015 insists on efforts to reverse the present situation to mitigate global warming by whatever possible means. Nonetheless, CO_2 concentration in atmosphere is continuously increasing along with ever increasing global energy demand. Hence there is an urgent need for the mitigation of CO_2 in the atmosphere by capture and storage or conversion into commodity chemicals. Carbon neutral concept is one of the important points to recycle the CO_2 by its activation and generate a useful feedstock. However, CO_2 is a stable molecule and non-combustible in nature; but, it is an appealing and sustainable C1 feedstock for the production of value added chemicals. The hydrogenation of CO_2 to alcohol or other hydrocarbons is an imperative approach; however the direct conversion to value added products is difficult, especially at industrial scale due to high thermodynamic stability of CO_2 over the possible products.[2] The symmetric and linear geometry of the CO_2 molecule with its C=O bonds makes it thermodynamically stable.[3] In order to activate the CO_2, a suitable catalyst with an active site for CO_2 adsorption and an ample amount of energy are required. This leads to weakening of C=O bonds in CO_2 and becomes susceptible to react with other reactants. Some of the reported CO_2 activation involves high pressure, which makes it energy intensive and hence ambient pressure route is anticipated by industries.

The conversion of CO_2 into fuels and chemicals has been intensely pursued for renewable and sustainable green energy. Among those, one preferred approach is CO_2 reduction to CO by employing H_2 as a reducing agent via reverse water gas shift reaction (RWGS) (Eq. 1); CO obtained can be used with H_2 in Fisher-Tropsch process or syngas to methanol synthesis.[4,5] Currently, it is assumed that H_2 would come from renewable resources, such as solar energy; employing the H_2 produced from reforming of fossil fuel is indeed counter-productive and meaningless.

$$CO_2 + H_2 \longrightarrow CO + H_2O \qquad \text{(Eq. 5.1)}$$

Generally it is accepted that CO_2 hydrogenation requires dual functional catalyst, for CO_2 and H_2 dissociation. As of now, an active metal, bimetal or alloy of the following metals (Ru, Ni, Cu, Pd and Pt) supported on an oxide (eg. SiO_2, Al_2O_3, TiO_2, CeO_2) are the commonly used catalyst for CO_2 hydrogenation. However, due to their complexity and cost, aforementioned systems limit their employability in the industries.[6-9]

In searching for an active, selective and low cost catalyst, transition metal carbides has shown special attention due to stability; carbides are also highly resistant to sintering, and poisons, such as sulphur.[10] In addition, similar electronic structure of carbides and noble metals makes metal carbides as a potential substitute for noble metal catalysts for a wide variety of reactions like reforming,[11-13] hydrogenation,[14] hydrodeoxygenation,[15] water gas shift reactions.[16-24] Liu and Rodriguez explain the modification of exposed metal-ion sites on the surface of metal carbide and compared with metal for CO and S adsorption.[25] Aforementioned properties affect the adsorption strengths and subsequent activity of the reactants. Among those metal carbides, molybdenum carbide (Mo_2C) exhibit remarkable catalytic activity due to its unique d band electronic structure, which show very similar to the Pt group metals. Porosoff et al. compared CO_2 hydrogenation reaction (1:2 CO_2:H_2) with transition metal carbides at 573 K and 1 atm pressure (TiC, ZrC, NbC, TaC, Mo_2C, WC) and they noted that Mo_2C shows more CO_2 conversion (4.6 %) and high selectivity towards CO.[26] From literature, it is known that CO_2 strongly binds to the surface of Mo_2C and decomposition begins >550 K to CO and O; decomposed oxygen oxidises the Mo_2C to MoOx.[27] However, partial activation of CO_2 was observed even at 300 K on the surface of Mo_2C and CO and O-species are observed in XPS studies.[28] In-situ XPS and XANES studies show the oxycarbide is an active phase for CO_2 hydrogenation to CO.[29] In spite of that, there is no consensus about the role of carbide/oxycarbide in the activity for CO_2 hydrogenation to CO. Theoretical studies reveal the highly exothermic and dissociated state of CO_2 (CO + O) on Mo_2C surface.[30] However, understanding the mechanism and catalyst surface structure under in-situ reaction conditions are always critical for further improving the activity and selectivity of the catalyst. In the present chapter, we have evaluated the CO_2 hydrogenation reaction with H_2 by near-ambient pressure x-ray photoelectron spectroscopy (NAPXPS). Mo_2C catalyst was generated in-situ by carburization of metallic Mo foil and employed for NAPXPS studies with mass spectrometry. In addition to the above mechanistic study, we extended our studies to powder Mo_2C catalysts in ambient pressure catalytic reactor under technically relevant conditions.

5.2. Results and discussion

5.2.1. Structure and morphology

XRD analysis of the as synthesized as well as spent catalysts (reaction carried out at 723 K with 1:3 CO_2:H_2 for 12 h) was performed to verify the stability of β-Mo_2C with hexagonal close packing (HCP) crystal structure (JCPDS 65-8766). XRD results obtained are shown in Figure 5.1a. As shown in Fig. 5.1a, diffraction peaks at 34.5, 38, 39.4, 52.4, 61.8, 69.6, 74.8 and 75.7 corresponds to (100), (002), (101), (102), (110), (103), (112) and (201) facets of β-Mo_2C.[31] Additional diffraction peak at 26^o in the spent catalyst is due to the formation of small amount of oxide phase after the reaction. Raman spectral recorded for fresh and spent catalyst is shown in Fig. 5.1b. First of all, there are no Raman bands observed between 1300 to 1600 cm^{-1} (e.g. D and G bands) indicating absence of graphitic carbon deposition on the surface. The remaining peaks at 816 and 992 cm^- corresponds to stretching vibration of Mo-C-Mo and Mo-C bonds.[32] Formation of graphitic carbon layers are expected to decrease the catalytic activity, as they block the active sites on the surface. Nonetheless, steady state catalytic activity observed for several hours suggests the active sites are fully available for the reaction without any hindrance. Raman analysis of the fresh and spent (Fig. 5.1b) catalysts suggests that Mo_2C phase is intact after reaction.[33]

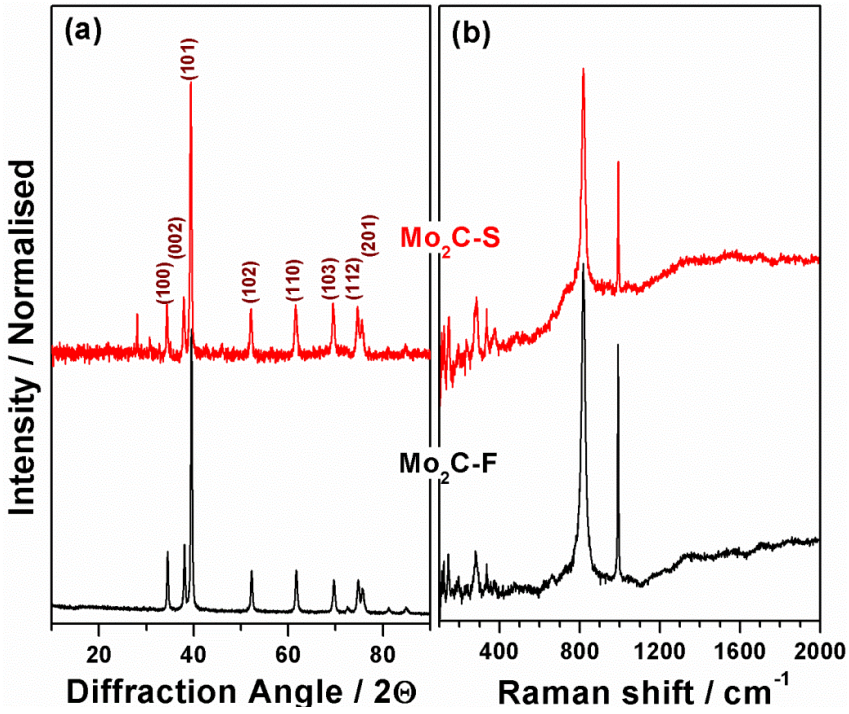

Figure 5.1: (a) XRD and (b) Raman spectra's of as synthesized fresh and spent samples.

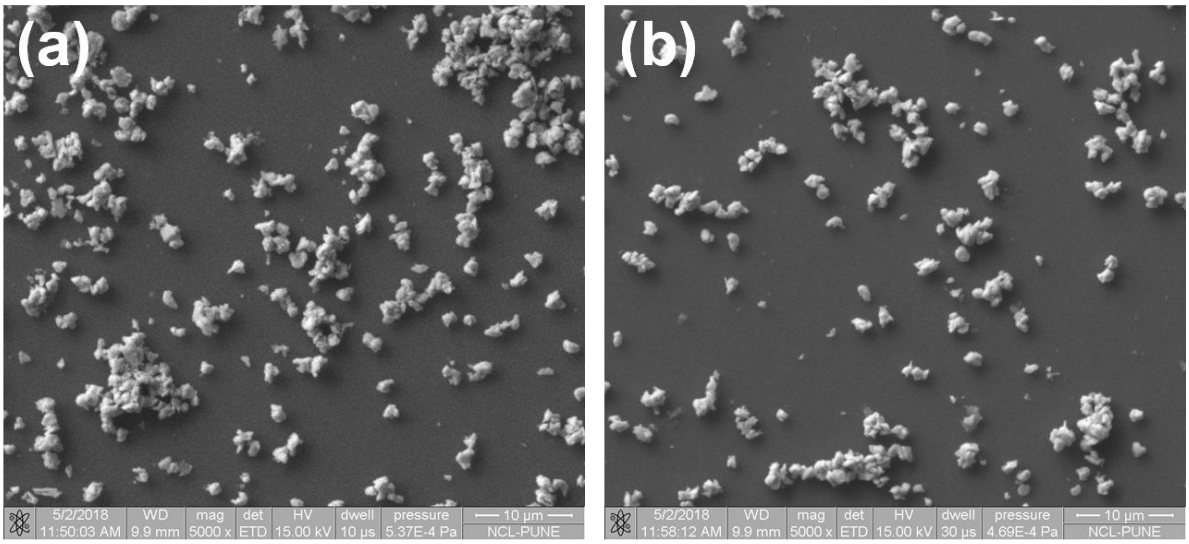

Figure 5.2: Scanning electron microscopy (SEM) images of synthesized Mo_2C powder catalyst a) Before b) After reaction CO_2 hydrogenation reaction.

Particle size and morphology of the catalyst was analysed by SEM and the results are shown in Fig. 5.2. Similar particle size (~2 µm) was observed for fresh and spent catalysts with no particular morphology. This indicates that the texture of the catalyst is retained after reaction.

5.2.2. XPS

The XPS analysis of fresh and spent catalysts was carried out; results obtained for Mo 3d, C 1s core levels and x-ray valence band spectra are shown in Fig. 5.3. It is to be underscored that CO_2 reduction experiments were carried out after activation in H_2 + CH_4 mixture and the fresh catalyst analysed for characterisation studies are without this pre-treatment. Mo 3d spectra show asymmetric features with three sets of peaks. Peak fitting was carried out with Mo 3d spectra to know the different species on the Mo_2C surface (Fig. 5.3a). Three type of species are present on the surface at binding energy (BE) 228 and 231.1, 229 and 232.1, and 232.5 and 235.6 eV assigned to Mo $3d_{5/2}$ and Mo $3d_{3/2}$ spin orbit coupled components of Mo^{2+}, Mo^{4+}, Mo^{6+}, respectively. Mo 3d peak at 228 eV (231.1 eV; red traces) is attributed to the carbide formation; carbide feature shows an increased intensity on spent catalyst. Another set of peak appears at 232.5 eV (235.6; blue traces) and it is attributed to Mo^{6+}, however, this feature shows a decrease in intensity on the spent catalyst. A marginal increase in Mo^{4+} oxidation state was observed after reaction and it appears at 229 eV (232.1;

olive green traces). Both features due to Mo^{4+} and Mo^{6+} are attributed to surface degradation by atmospheric components, like oxygen, water. Indeed, both components are observed to be significantly lower in intensity on spent catalyst, than the fresh catalyst, indicating the spent catalyst is resistive to degradation.

Figure 5.3b shows the C 1s spectra with a prominent peak at 282.8 eV (red), corresponding to carbide feature. However, spent catalyst shows high intensity carbide feature and another broad feature at around 286 eV; later feature is attributed to the carbon associated with oxygen, such as formaldehyde (purple). Increase in carbide feature on spent catalyst affirms the majority of Mo_2C is intact. The remaining peak observed at 284.5 (green) and 287.7 eV (blue) are attributed to carbon and carbonate features, respectively.

X-ray valence band (XVB) spectral results of both fresh and spent catalysts of Mo_2C are shown in Figure 5.3c. Reference XVB spectra recorded for Mo_2C and MoO_3 are also shown in Fig. 5.3c, for comparison purposes. In the valence band spectra, features at the BE between 0-4 eV arises from the Mo 4d bands and 4-8 eV region arises due to C and/or O 2p orbitals.[34] However, presence of intense valence band features at both regions 0-4 and 4-8 eV is attributed to the contribution from Mo 4d and C 2p of Mo_2C. Relative intensity of the Mo 4d increased due to more carbide formation from fresh to spent catalyst, which helps in the activation of CO_2 and H_2. Contribution from O 2p cannot be ruled out due to some amount of MoO_2 and MoO_3. However, typical features[34] of MoO_2 or MoO_3 is not observed in Fig. 5.3c indicating the amount of such phases are minimum on the surface and within the probing depth. This is further supported by two orders of magnitude smaller photoionization cross section (σ) of C 2p (10^{-5} Mb) than O 2p (2.4×10^{-3} Mb) with AlKα photons, which lead to nearly comparable intensity for spent catalyst due to predominant Mo_2C formation.[35,36] Two order of larger magnitude of σ for O 2p lead to large intensity in XVB for fresh catalyst due to oxide (and carbide) species on the surface.

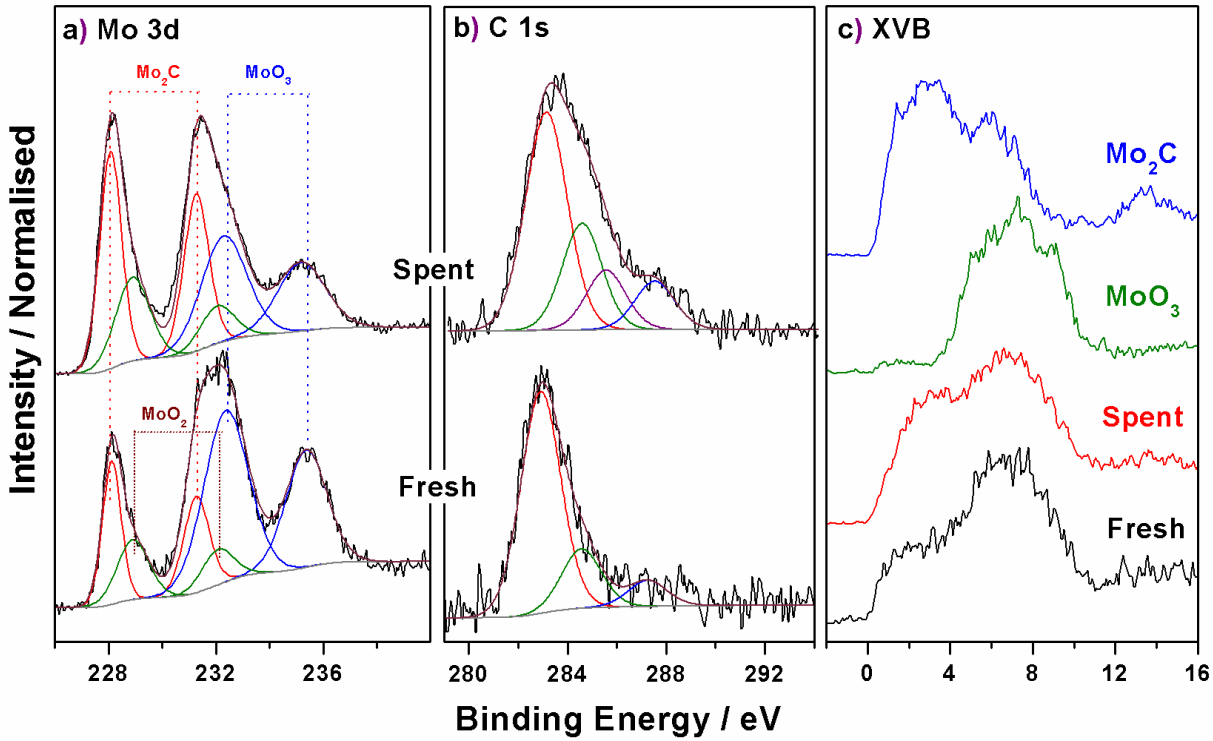

Figure 5.3: XPS spectra of β-Mo_2C powder before (fresh) and after reaction (spent) a) Mo 3d b) C 1s, c) x-ray valence band.

5.2.3. TPD and TPR studies

In order to explain the basicity, CO_2-temperature programmed desorption (CO_2-TPD) spectra of the fresh Mo_2C sample was performed and the result is given in Figure 5.4a. It shows three features at different temperatures. The CO_2 desorption peaks centred at 573, 663, 853 K are attributed to weak, medium and strong basic sites present on the Mo_2C surface, which are helpful in adsorption of CO_2 on the surface. Among all desorption peaks, narrow and high intensity peak observed at 663 K, and significant part of basicity is contributed by these basic sites. In general, adsorption of CO_2 is difficult on many catalyst surfaces due to symmetric and linear geometry of the CO_2 molecule.[3] However, the exceptional basicity of the Mo_2C surface can absorb Lewis acidic nature CO_2 on the basic sites of Mo_2C surface. It is also to be mentioned that the RWGS reaction maximum occurs between 673 and 723 K (discussed later), and directly indicating the role of basic sites in the CO_2 activation.

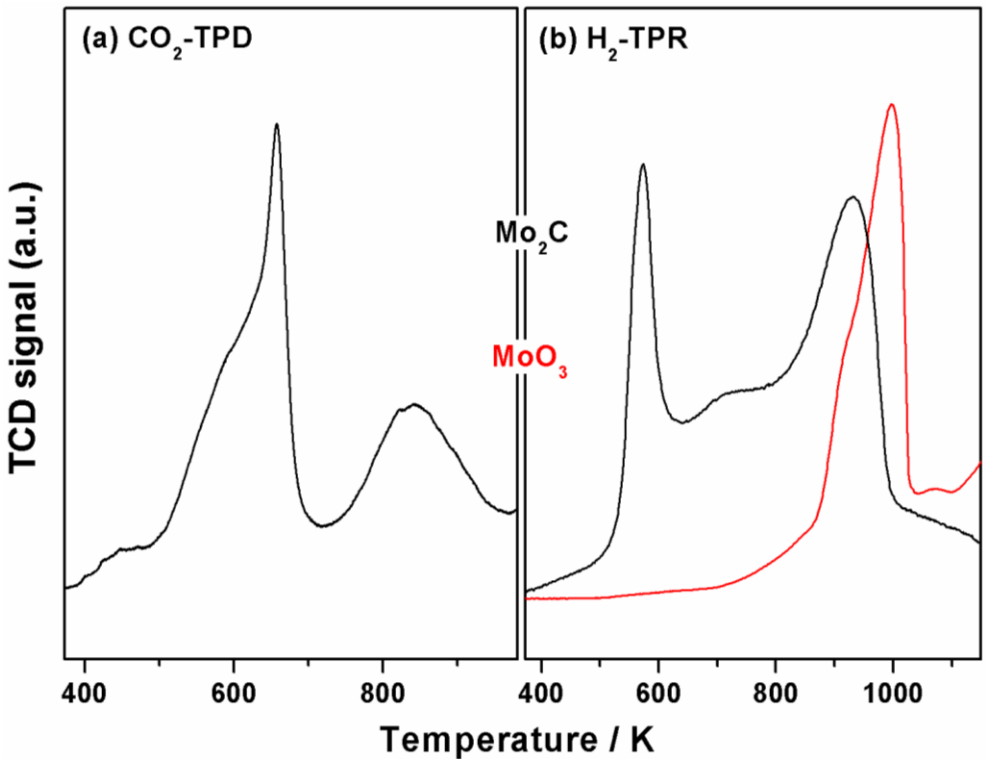

Figure 5.4: (a) CO_2-Temperature programmed desorption (CO_2-TPD) and (b) H_2-Temperature programmed reduction (H_2-TPR) of β-Mo_2C and compared with MoO_3.

H_2-TPR profiles for the carburized (Mo_2C) and oxide (MoO_3) catalysts are shown in Fig. 5.4b. Mo_2C catalyst exhibited two main H_2 consumption peaks centred at about 573 and 923 K respectively. The low temperature narrow reduction peak observed at 573 K is assigned to the reduction of surface molybdenum oxycarbide. Wang et al. also observed a similar reduction feature at 543 K for molybdenum oxycarbide. Another peak observed around 923 K results from the reduction of molybdenum carbides to metallic Mo. Moreover, it can also be ascribed to the reduction of Mo_2C species.[37] Only one broad and high temperature reduction feature was observed with MoO_3. The high temperature reduction peak, around 998 K, corresponds to the reduction of MoO_3 to Mo-metal. It is to be noted that the high temperature peak observed for MoO_3 is at significantly high temperature (998 K) than that of Mo_2C (923 K), which allows the distinction between them. Some contribution of oxide in Mo_2C cannot be ruled out and an overlap between the two features attests this point. The high temperature peak, corresponding to the reduction of MoO_3 to metallic Mo species, is observed at higher temperature compared to Mo_2C. This result points out that the carburization process resulted in carbide species, which also exhibit metallic character. H_2 species are dissociated easily and spills over on carbide surface, which makes the reduction

of Mo_2C easy, compared to pure MoO_3. The broad peak observed at 700 K may be due to reduction of different MoO_x species present on the surface.[38]

A comparison of TPR and TPD results shown in Fig. 5.4 for Mo_2C directly shows all the three features in both techniques appear around the same temperature maximums and within ±50 K. This underscores the possible synergy between basicity and reduction with maximum CO_2 activation observed around 673 K. Supply of hydrogen atoms at the point of CO_2 activation is crucial to achieve higher catalytic activity, and we believe Mo_2C meets this particular requirement. However, more in-situ experiments, such as IR, may be performed to ascertain this aspect.

5.2.4. Catalytic activity of RWGS reaction

The RWGS on β-Mo_2C was performed in fixed bed catalytic reactor at atmospheric pressure between 473 and 723 K with different CO_2:H_2 ratios (1:3, 1:7), at gas hourly space velocity (GHSV) of 20000 h^{-1}. The catalytic activity is found to increase with temperature and the results obtained are shown in Fig. 5.5a and 5.5b for CO_2:H_2 ratios of 1:3 and 1:7, respectively. In RWGS reaction, CO is a desired product as it can be directly utilized in the Fischer–Tropsch or methanol synthesis, while CH_4 is an undesirable product because of its abundance and difficulties in transportation. However, CH_4 is a thermodynamically preferred product as compared to CO in typical CO_2 hydrogenation process.[39] It is also to be mentioned that for each molecule of CO_2 to methane formation ($CO_2 + 4H_2 \rightarrow CH_4 + 2H_2O$), four molecules of hydrogen is consumed. Considering the cost and fuel value of hydrogen, it is worthless to make methane through this route. Although RWGS reaction is thermodynamically feasible, but it is a kinetically hindered reaction.

The CO_2 conversion generally increases with increasing reaction temperatures; in the case of 3:1 (H_2:CO_2) ratio (Fig. 5.5a) with Mo_2C catalyst, it increases from 34 % at 473 K to 57 % at 723 K. The activity towards RWGS is substantially improved in the presence of the carburized catalyst and selectivity of CO reaches to 61 %. In the case of higher H_2:CO_2 ratio (7:1), CO_2 conversion increased from 25 % at 473 K to 65 % at 723 K, whereas the CH_4 selectivity also increased with increasing H_2 content. At high H_2:CO_2 ratio, rate of methanation process also increases as predicted by equilibrium thermodynamics. Selectivity towards unwanted methane gradually increased from low to high temperature as well as with H_2-rich ratio from 1:3 to 1:7 (5 to 9 %) at 723 K. Nearly 3-4 times increase in CO selectivity

was observed when the temperature increased from 523 to 573 K (Fig. 5.5a and 5.5b) underscoring the synergy effect mentioned in the earlier section. From the detailed physico-chemical and electronic structural characterization, it is clear that, carburization results in increased basicity, i.e. the CO_2 absorption ability of this catalyst, and simultaneously increases the metallic character of Mo_2C (discussed later) which enhances the H_2 activation. In comparison with different ratios, CO_2:H_2 ratio with 1:7 shows the highest conversion (68 %) of CO_2, over 1:3 ratio (60 %), while H_2 conversion is high in the case of 1:3 (21.5 %). It is interesting to underscore that the stoichiometric amount of CO_2 and H_2 is adsorbed at high temperatures; 60 % CO_2 and 20 % H_2 conversion from 3:1 (H_2:CO_2) corresponds to 1:1 stoichiometric amount of adsorbed CO_2 and H_2. This ideal adsorbed surface composition leads to the maximum reactivity with selectivity. Significantly large amount of adsorbed H_2 with 7:1 H_2:CO_2 composition leads to hydrogen enriched surfaces and hence the composition of surface adsorbed species turns to be around 2:1 (H_2:CO_2). This leads to more methane. Inclusive of all these points, Mo_2C catalyst surface with 1:3 ratio show the economically attractive catalytic activity for the CO_2 hydrogenation to CO.

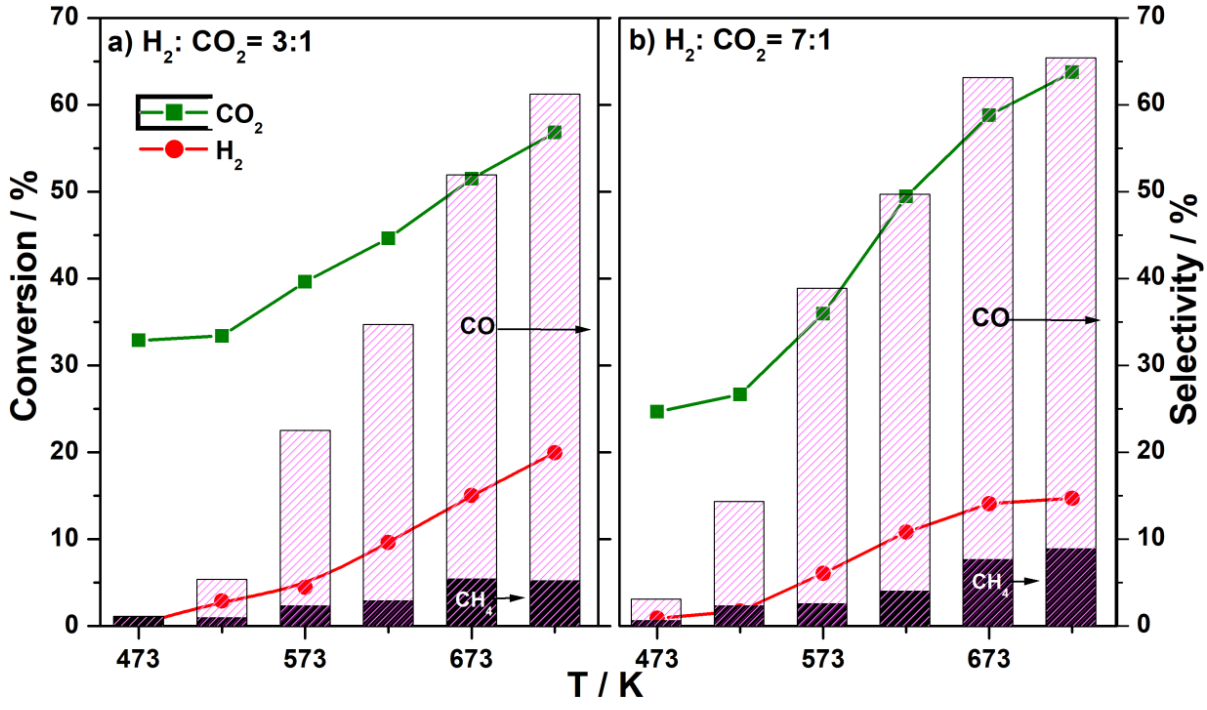

Figure 5.5: CO_2 hydrogenation on the Mo_2C catalyst at different temperatures with different ratio of reactants. GHSV was maintained at 20000 / h.

5.2.5. Time on stream studies

Sustainability of the Mo_2C catalyst was evaluated to explore the stability aspects. We have carried out the time on stream (TOS) studies with Mo_2C catalyst for the CO_2 hydrogenation reaction with 1:3 ratio of CO_2:H_2 at different temperatures (623 and 723 K) for 12 h and the results obtained are shown in Fig. 5.6. At 623 K, CO_2 conversion is observed to be 44 % with 34 % CO selectivity (Fig. 5.6a); it is important to note that the activity and selectivity is stable for a period of 12 h. In addition, the conversion of H_2 is also

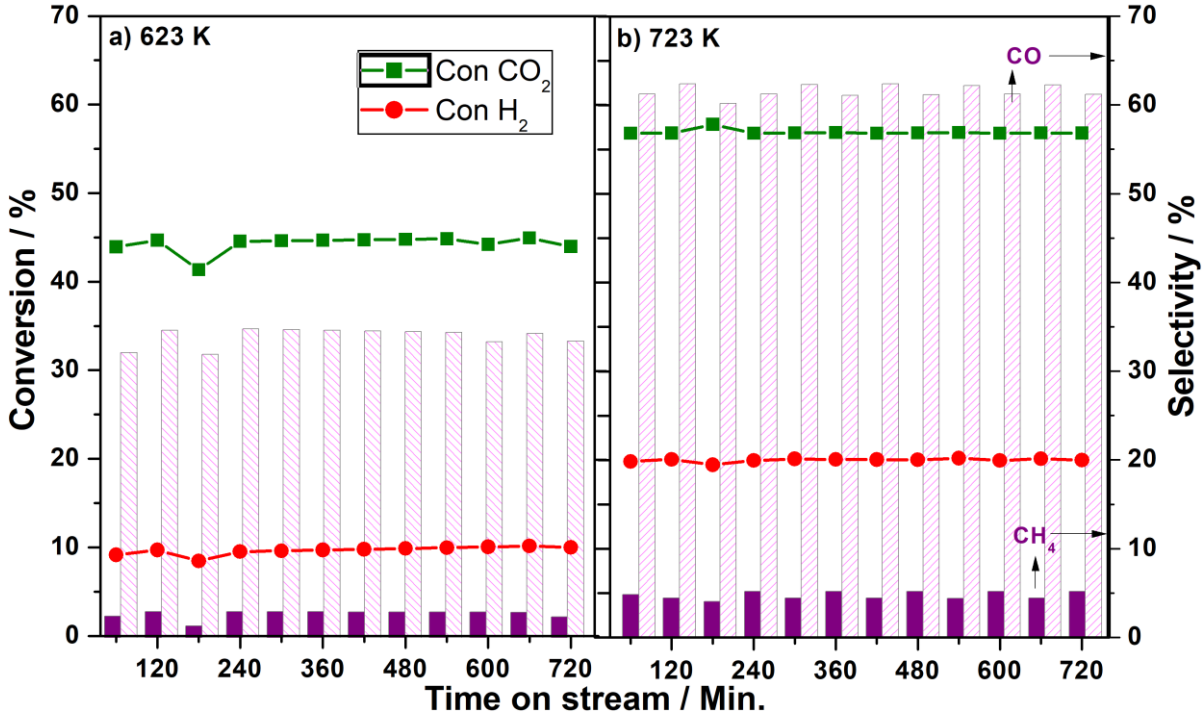

Figure 5.6: Time on stream studies on Mo_2C for CO_2 hydrogenation with 1:3 ratio of CO_2:H_2 at temperatures (a) 623 K and (b) 723 K.

observed to be constant (10 %) for the entire period of 12 h. Small but constant (2.5 %) methane formation was observed. On other hand, CO_2 conversion to CO was observed to be 56 % with 65 % selectivity (Fig. 5.6b) at 723 K under same reaction conditions. From the present time on stream study, it is clear that Mo_2C catalyst is highly active and stable under CO_2 hydrogenation reaction conditions. However, a much longer TOS study is suggested to evaluate the applicability of the Mo_2C catalyst.

5.2.6. In-situ XPS studies

The mechanistic investigation of CO_2 hydrogenation on the in-situ generated Mo_2C on Mo-metal foil has been explored with NAPPES at 0.1 mbar pressure as a function of reactants ratio (CO_2:H_2) and temperature. Carburization aspects of Mo-foil to Mo_2C with ethylene are recorded with NAPPES and the results are shown in Figure 5.7.

5.2.7. In-situ preparation of Mo_2C on Mo-foil

Mo-foil was introduced into the NAPPES chamber and subjected to extensive sputter cleaning. Sputter cleaned Mo-surface shows only Mo and metallic features, without any other impurities. Carburization process started at high temperatures and Mo-spectra was recorded at 700 K in UHV. A small amount of carbon and oxygen segregation from the subsurfaces occurs on heating (Fig. 5.7; bottom most black traces); otherwise there are no other impurities observed. Subsequently, Mo-foil was exposed to a controlled amount of ethylene and NAPPES spectra were recorded simultaneously to follow the changes in spectral pattern of Mo to Mo_2C. The UV valence band (NAPUPS) and core level XPS spectra of the Mo foil was recorded as function of ethylene exposure time at two different temperatures and the results are shown in Fig. 5.7. At UHV 700 K (and at room temperature), intense Fermi level (E_F) was observed at BE = 0 eV, indicating the metallic nature of the Mo. The clean Mo surface show Mo 4d features from 0 to 3 eV with high density of states (DOS) at E_F. A broad feature at around 6 eV is attributed to defect sites present on the surface due to extensive sputtering while cleaning the Mo-foil.

Ethylene was introduced in the NAPPES analysis chamber and its partial pressure was gradually increased to 10^{-5} mbar while the Mo-foil was kept at 700 K. Ethylene exposure was continued at 700 K and the spectra were recorded in-situ in the first few minutes (red color traces in Fig. 5.7). A significant enhancement in the intensity of the band at 1.8 eV was observed. C 1s, O 1s core levels recorded under the same conditions show barely any changes on the surface; however, Mo 3d level shows a minor BE shift by 0.3 eV. However, same E_F feature is observed without any significant change. On continuing ethylene exposure between 15 (blue traces) and 45 min. (green traces), some more changes are observed and they are listed below. While E_F feature was maintained in the VB, features at 4 and 6 eV merged to become a single broad feature (Fig. 5.7a). The feature observed at 1.8 eV disappeared. Mo 3d

core levels shifted to higher BE by 0.2 eV. Importantly, O 1s feature disappeared and C 1s core level show a typical carbide feature.

On continuing with ethylene exposure either at 700 K or at 1025 K at 10^{-5} mbar pressure of ethylene for 60 min., no significant changes in any of the core levels and valence band was observed. NAPPES spectra were recorded at 700 K at 10^{-5} mbar ethylene. C 1s core level shows well-developed features, fitted with three components. Feature at 282.8 eV is attributed to carbide and other two features (284-285 eV) are attributed to adsorbed ethylene and its fragments on the surface. No O 1s feature was observed and Mo 3d shifted to 228 eV supporting the formation of Mo_2C. On continuing the ethylene dosing under the above conditions for up to 45 min. at 1025 K did not bring any other changes, except carburization extending to more number of subsurface layers. Notably, retaining the Fermi level intensity reflects the metallic nature of Mo_2C.

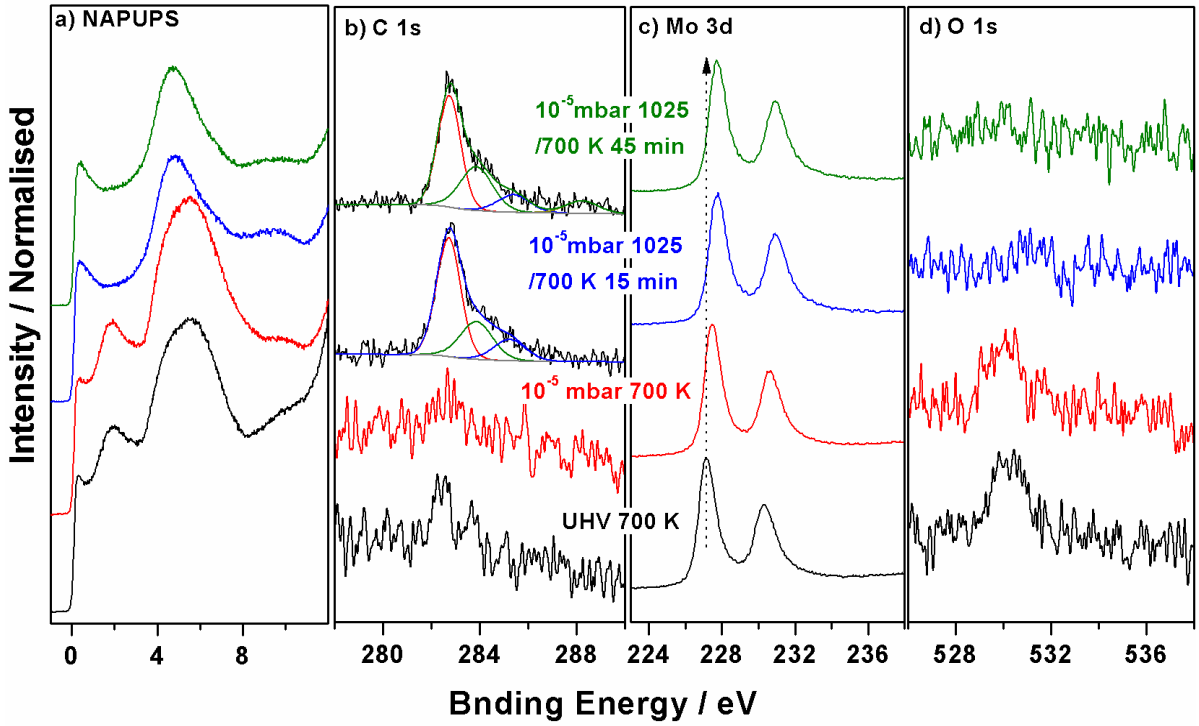

Figure 5.7. a) NAPUPS, b) C 1s, c) Mo 3d, d) O 1s spectra of Mo foil during carburization from Mo metal to Mo_2C at 700 K and 0.1 mbar pressure of ethylene.

5.2.8. Ex-situ Raman and EDX analysis of Mo_2C

X-ray diffraction of Mo metal and Mo_2C generated in NAPPES was recorded and the result is shown in (Figure 5.8). XRD patterns of both appear to be similar, and there are no

changes observed; this attests the fact that Mo_2C formation is restricted to the surface layers and not to the bulk layers.[40]

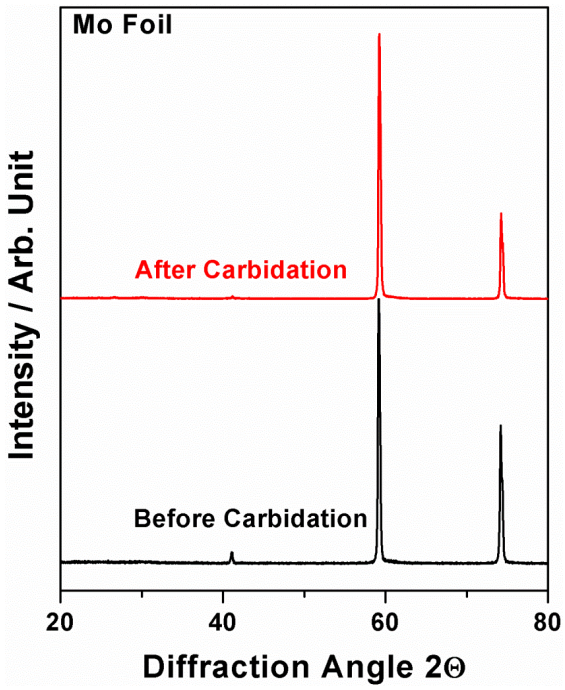

Figure 5.8: XRD spectra of Mo foil before and after carburization process.

Energy-dispersive x-ray (EDX) spectral analysis was carried out to further confirm the formation of Mo_2C and results obtained are shown in Figure. 5.9. With increase in the electron source energy, analysis depth also increases and this helps to ascertain the depth of Mo_2C layers formation. Electron source at 5 kV potential shows more carbon and Mo 3d peaks. Further analysis has been carried out at higher electron source potential at 10 kV; carbon intensity decreased very much and at the same time increase in the intensity of the Mo peak was observed. On increasing the source energy to 15 and 20 kV, further decrease in C intensity was observed. Intensity ratio of Mo/C increases with increasing applied potential fully support the formation of Mo_2C is restricted to the surface layers.

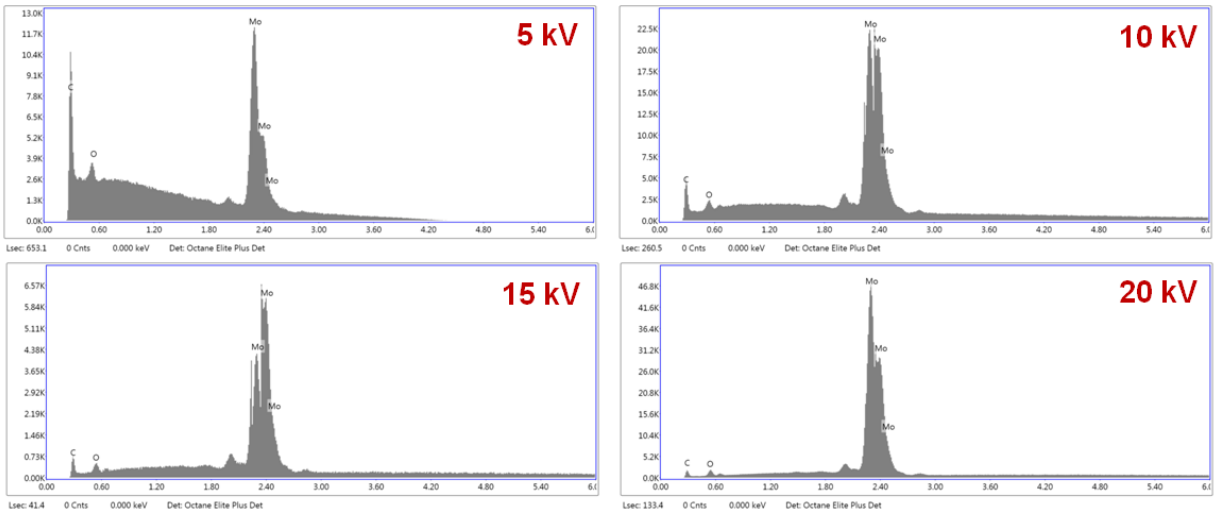

Figure 5.9: SEM-EDX analysis of as prepared Mo_2C foil with different electron energy source.

5.2.9. In-situ CO_2 hydrogenation on Mo_2C foil

Mo_2C generated in-situ was employed for CO_2 reduction reaction with H_2 in NAPPES and spectra were recorded simultaneously. Figure 5.10 shows the C 1s spectra of Mo_2C at different reactants, namely, a) CO_2 alone, b) 1:3 CO_2:H_2, and c) 1:7 CO_2:H_2 ratio at a working pressure 0.1 mbar as a function of temperatures from 325 to 625 K. Initially, broad and multiple features of C 1s spectra observed were deconvoluted to identify the types of different components present on the Mo_2C surface. In the C 1s spectra, peaks at 282.8 (red), 283.9 eV (olive green) assigned to carbide, oxycarbide respectively.[41] In addition to that, peak appearing at 285 (blue) is attributed to the surface carbon, possibly available due to ethylene fragments. A broad and low intensity feature observed at 292.5 eV in Fig. 5.10a is due to gas-phase CO_2. This feature is not observed under reaction conditions with CO_2+H_2 mixtures (Fig. 5.10b and 5.10c) due to low partial pressure of CO_2. The bottom most (UHV 295 K) spectrum in all panels of Fig. 5.10 is for Mo_2C and shows presence of carbide, oxycarbide and some carbon from ethylene fragments on the surface. Even after dosing 0.1 mbar pressure of reactants CO_2 and H_2 with different CO_2:H_2 ratios at 295 K, there was no noticeable change was observed on the surface of Mo_2C. Further, gradual increase in the temperature up to 625 K did not bring much change in the carbide, oxycarbide peak and no other intermediates were observed in all cases. No peak at 288.5 eV due to adsorbed CO_2 was observed hinting a possible direct dissociation of CO_2 on adsorption.[42] Above observations indicates that dissociative adsorption of CO_2 taking place on the Mo_2C surface into CO

species followed by desorption of CO; oxygen from CO_2 dissociation reacts with H_2 to form H_2O molecules and its subsequent desorption. Formation of CO and H_2O during the reaction in both ratios was observed with mass spectrometer, which was attached to NAPPES (Fig: 5. 14).

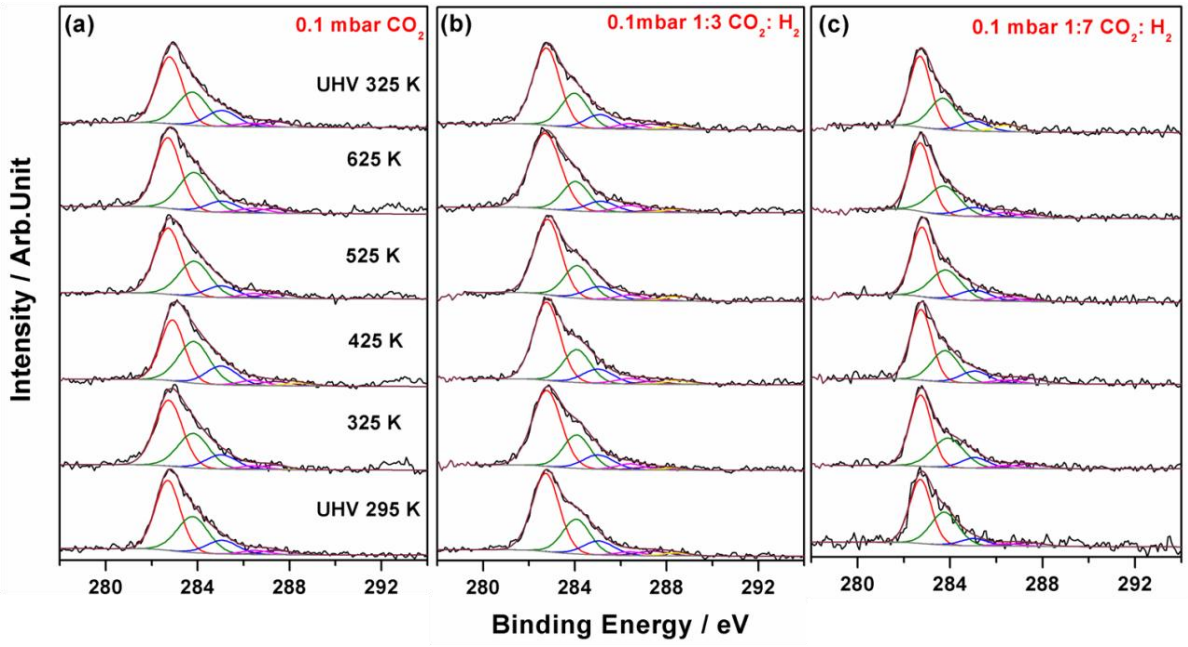

Figure 5.10: *In-situ* XPS studies of CO_2 hydrogenation on Mo_2C with different ratios of C 1s spectra a) pure CO_2, b) CO_2:H_2 1:3, and c) CO_2:H_2 1:7 at various temperatures. The bottom most trace is the reference C 1s spectrum recorded on Mo_2C in UHV condition at 295 K.

There are no apparent changes observed in the Mo 3d spectra, recorded under same conditions as that of Fig. 5.10, indicating the chemical nature of the Mo remains the same under reaction conditions with CO_2 or CO_2+H_2 exposure (Figures 5.11 and 5.12). However, a careful analysis of the results reveals a narrowing of Mo 3d peaks with 1:7 composition of CO_2:H_2, compared to 1:3 (CO_2:H_2) or pure CO_2. This lead to a narrow features of Mo 3d peaks and a large depth of valley between Mo 3d spin-orbit components with 1:7 composition, compared to the other two cases. A deconvolution shown in Fig. 5.11 for the spectra recorded at 625 K reveals significant minor components at high BE 228.6 (olive green) and 229.1 eV (blue) for oxycarbide, oxide features in the first two cases; however, oxycarbide and oxide is very low in intensity with 1:7 ratio. Very likely the large amount of H_2 present in the 1:7 CO_2:H_2 ratio removes the dissociated O from CO_2 and hence the oxycarbide/oxide amount is found to be very small.

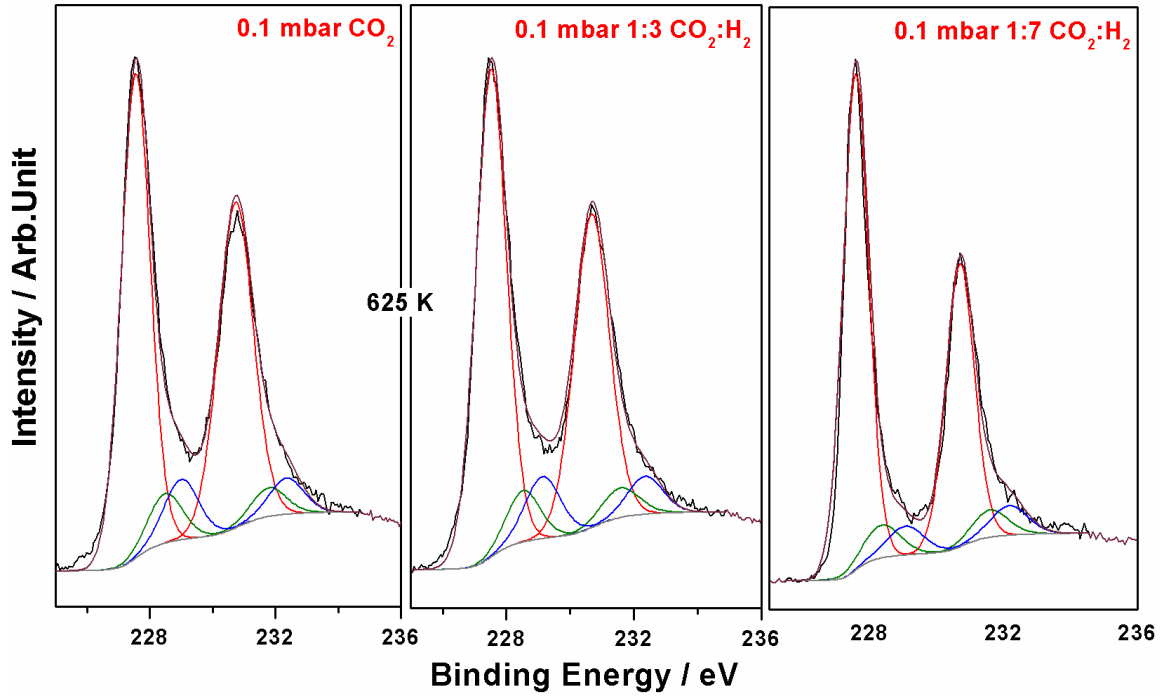

Figure 5.11: Mo 3d spectra of CO_2 hydrogenation on Mo_2C foil with different ratios a) Alone CO_2 b) CO_2:H_2 1:3 and c) CO_2:H_2 1:7 at 623 K.

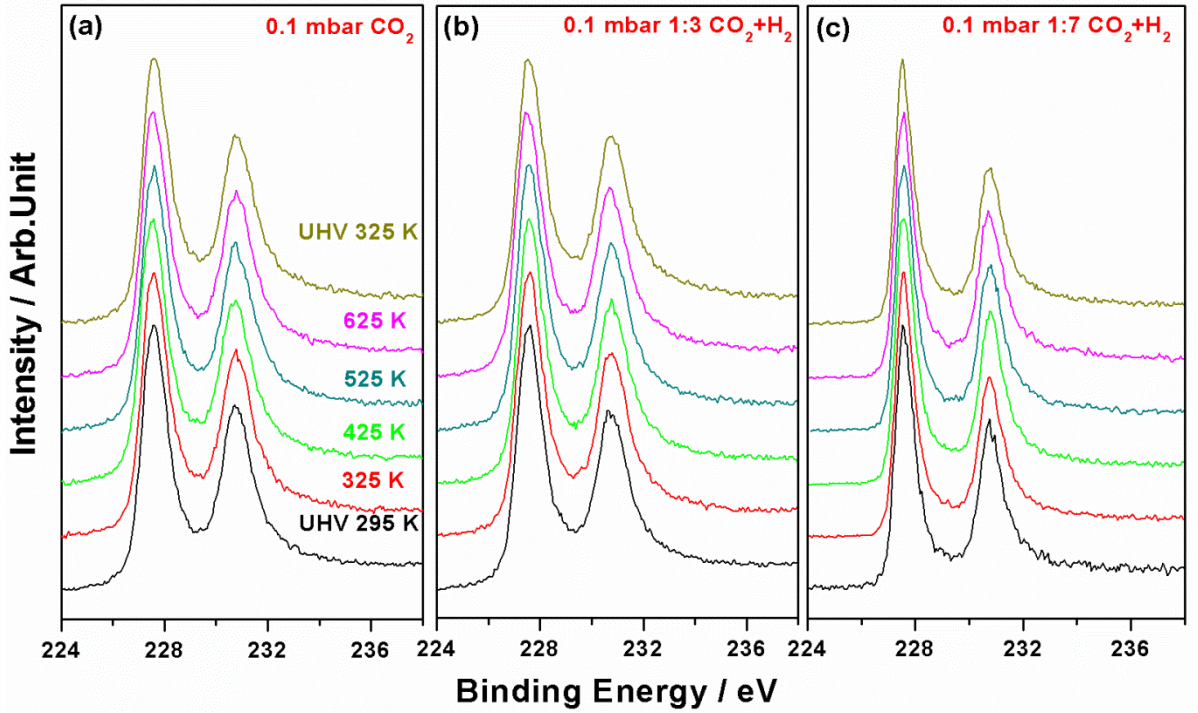

Figure 5.12: Mo 3d spectra of CO_2 hydrogenation on Mo_2C foil with different ratios a) Alone CO_2 b) CO_2:H_2 1:3 and c) CO_2:H_2 1:7 at various temperatures.

The O 1s spectra of Mo_2C recorded in all the conditions (CO_2 alone, 1:3 and 1:7 ratio of CO_2:H_2) at 0.1 mbar, as that of Fig. 5.10, and the results are shown in Figure 5.13. Initially, broad and multiple features of O 1s spectra were deconvoluted to identify the types of oxygen species present on the surface. In the O 1s spectra, peaks at 529.6 (red), 531.1 (olive green), 532.9 eV (blue) assigned to oxide, oxycarbide and hydroxyl species, respectively. A broad and high intensity feature observed at 536 eV in Fig. 5.13a, 5.13b is due to gas-phase CO_2. This feature is not observed with 1:7 CO_2:H_2 (Fig. 5.13c) reaction mixture due to low partial pressure of CO_2. An initial UHV 295 K spectrum of Mo_2C in the all conditions shows the presence of oxide, oxycarbide on the surface. While dosing with 0.1 mbar pressure of CO_2 from 295 to 625 K, no significant change in the O 1s (oxide and oxycarbide features) was observed, since there is hardly any reaction, after initial adsorption/dissociation of CO_2. Gas-phase CO_2 feature was observed till the pressure was maintained at 0.1 mbar. In addition to oxide and oxycarbide features, hydroxyl species was observed at 532.9 eV in the presence of CO_2+H_2 (1:3 and 1:7) conditions (Fig. 5.13b and 5.13c). However, hydroxyl species is unstable at high temperatures and desorbs as water molecule. An interesting observation made is the shift in the BE of gas-phase CO_2 feature to lower BE at high temperatures, while the oxide and oxycarbide features are observed at the same BE. This underscores the change in the work function of the surface under reaction/measurement conditions.[43,44] In case of CO_2 alone at 0.1 mbar, no change in the gas phase CO_2 feature BE (536 eV) was observed from 295 to 623 K; however in the case 1:3 ratio (CO_2: H_2), BE decreased from 536 to 535.6 eV attesting the dynamic change in the work function occurring under reaction conditions.[45-47] It is also to be noted that O 1s spectra are broad with 1:3 of CO_2:H_2 (Fig. 5.13b), compared to other two conditions shown in Fig. 5.13a and 5.13c. As the hydroxyl species begins to disappear at high temperatures, surface work function also changes concurrently. From above observations, it is clear that due to dissociative adsorption of CO_2 on the surface lead to CO and O species, followed by desorption of CO. Oxygen atoms available on the surface reacts either with H_2 to form H_2O or reacts with Mo_2C to form oxycarbide. Latter oxycarbide is observed under all conditions with 1:3 ratio and indicating its role in catalysis. However, large amount of hydrogen available in 1:7 composition leads to a gradual decrease in the oxycarbide feature at high temperatures. Formation of H_2O during the reaction with both ratios was observed in mass spectral results (Fig: 5.14).

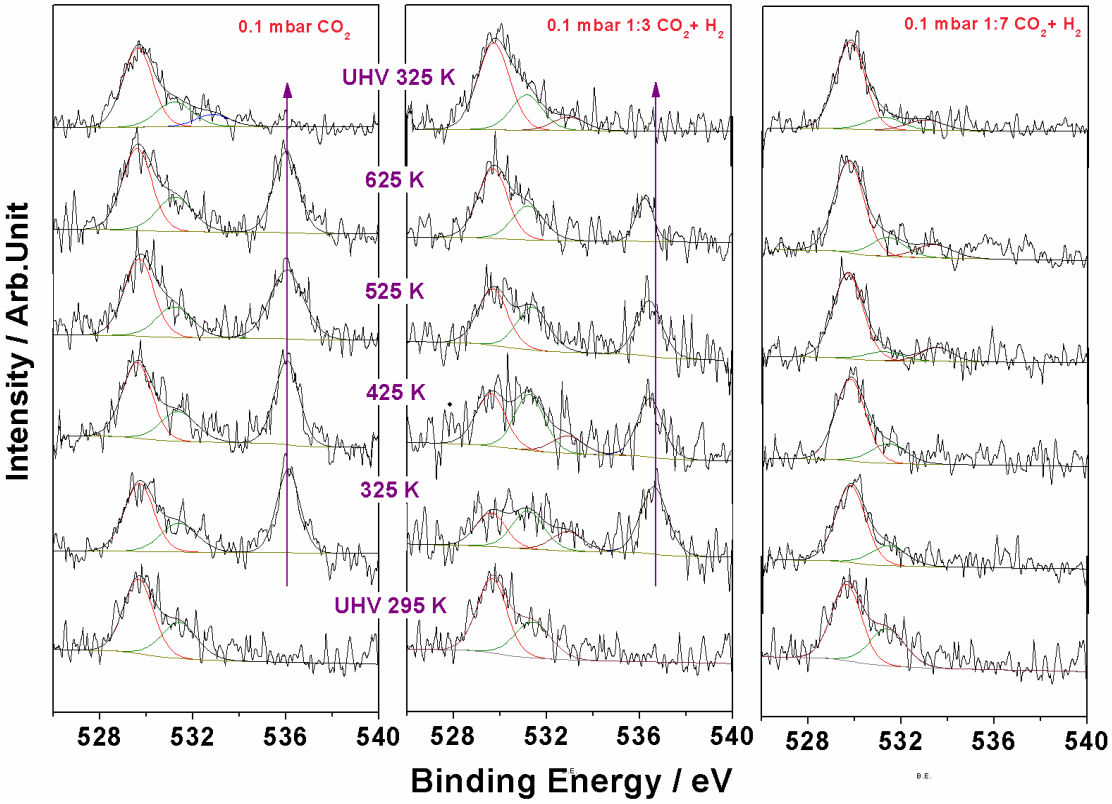

Figure 5.13: O 1s spectra of CO_2 hydrogenation on Mo_2C foil with different ratios a) Alone CO_2 b) CO_2:H_2 1:3 and c) CO_2:H_2 1:7 at various temperatures.

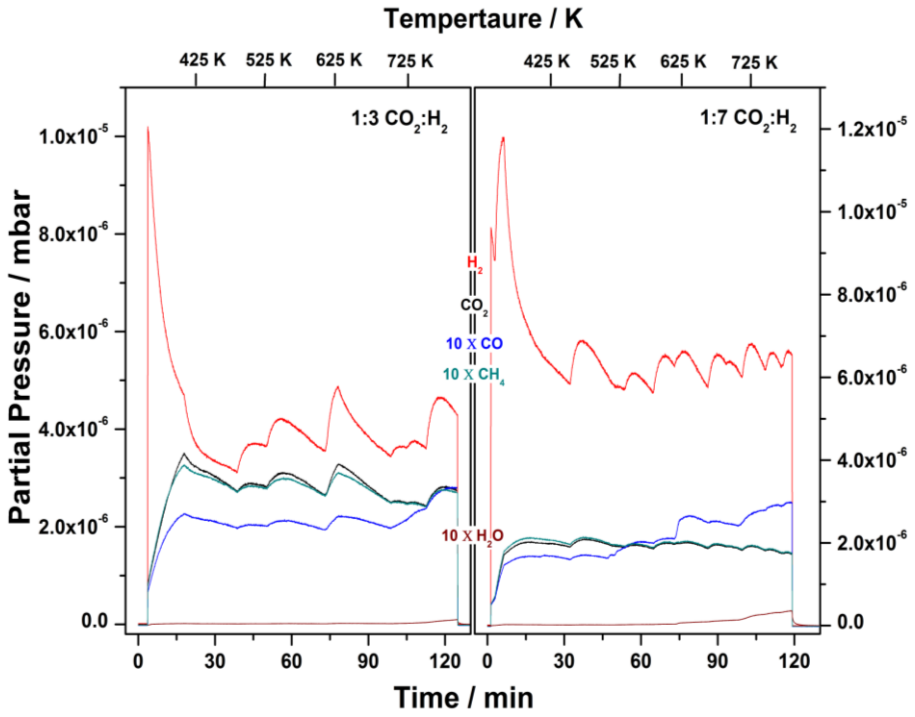

Figure 5.14: Mass spectrometry analysis of CO_2 hydrogenation on Mo_2C foil with different ratios of CO_2:H_2 (1:3) and CO_2:H_2 (1:7) at various temperatures. It is to be noted that CO_2,

CO and CH_4 shows very similar intensity pattern, mainly due to secondary fragments (CO for CO_2) or same mass species bur originating from different sources (16 O from CO_2 and CO, and CH_4). Hence it is difficult to ascertain the reaction details from this data alone. However, more CO generation is observed with 1:7 compositions at high temperatures. Fluctuations in the intensity pattern are due to opening of leak valve to maintain the same pressure during reaction measurements.

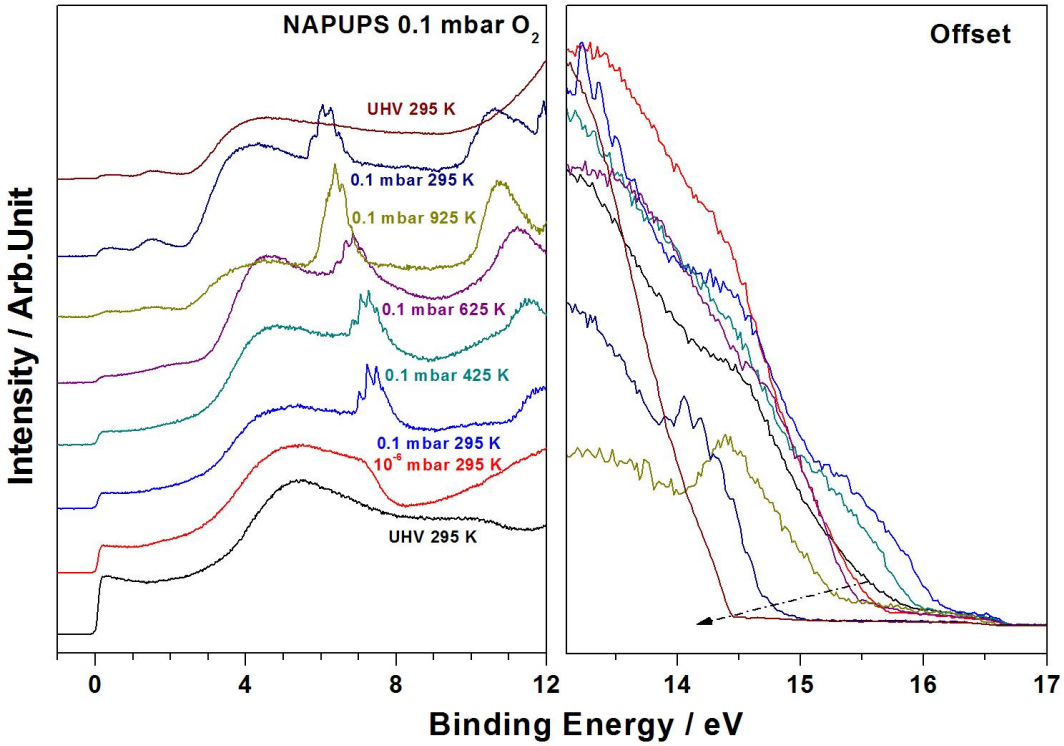

Figure 5.15: NAPUPS spectra of Mo_2C foil oxidation at 0.1 mbar O_2 with various temperatures.

Oxidation of Mo_2C has been carried out to ensure the stability of the as prepared Mo_2C foil in 0.1 mbar pressure of pure O_2 as a function of temperature and simultaneously NAPXPS and UV valence band also recorded. Figure 5.15 and 5.16 shows the UV valence band and XPS spectra (recorded for O 1s, C 1s and Mo 3d core levels) of Mo_2C. Typical carbide feature is retained up to 625 K, and there after oxide formation begins gradually. As we discussed earlier section, Initial features UV valence band and XPS spectra of Mo_2C retained up to 625 K. At 925 K carbide features are disappeared completely and molybdenum oxide formed. Further details about UV valence band and XPS features of Mo metal, its oxides given in 4 chapter. This information also supports the carbon from Mo_2C is not consumed for CO generation.

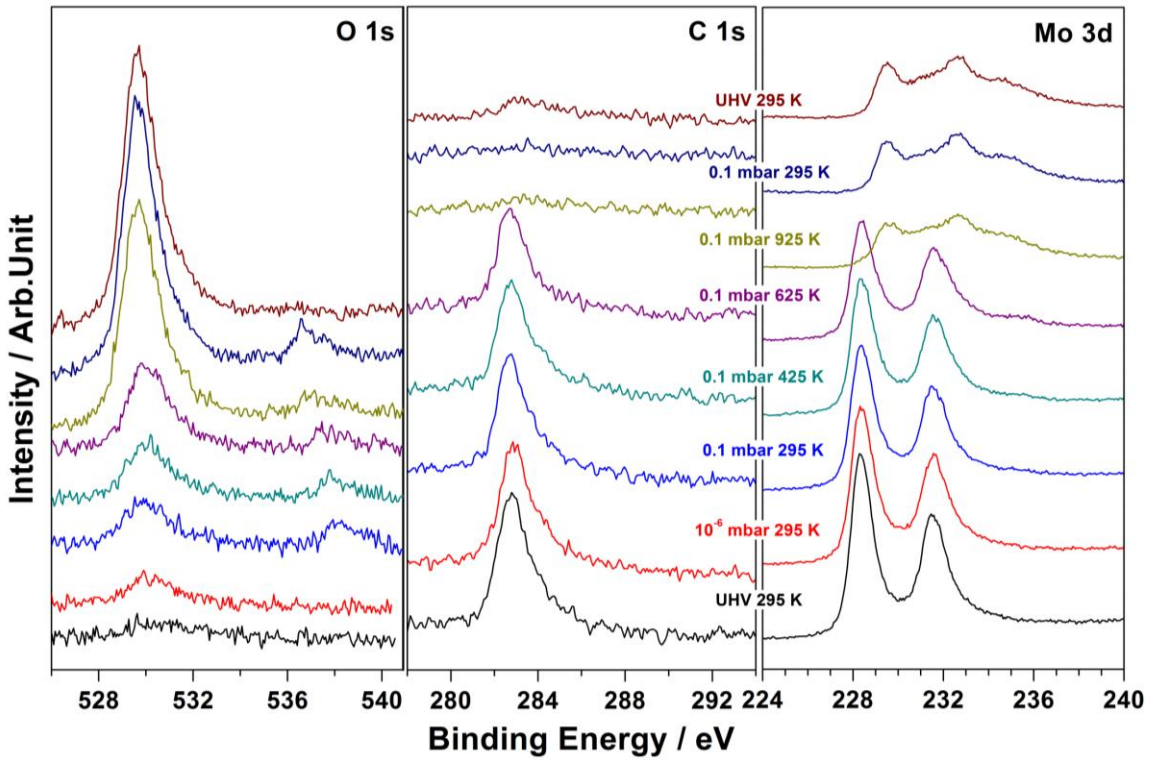

Figure 5.16: NAPXPS spectra of Mo_2C foil oxidation at 0.1 mbar O_2 with various temperatures.

In general, metal oxides are being used as a support for the catalytically active metals, on which CO_2 activation experiments are carried out. CO_2 activation also depends on the basicity and reducibility of the support. By stabilizing the right reducibility one can enhance the adsorption and activation of CO_2. These can be commonly achieved by making the oxide-oxide or oxide-metal interfaces. However, metal oxide-carbide interface also can induce the electronic structural changes which lead to the high CO_2 adsorption-dissociation capacity. H_2-TPR of Mo_2C has shown the reduction peak (Figure. 5.4b) at 573 K due to the reduction of oxycarbide. From the CO_2-TPD spectrum, it is evident that the rich basic sites on the surface are helpful in the adsorption of CO_2 with high activity and selectivity. In-situ XPS studies has shown that there was no intermediates species in the C 1s spectra indicating the dissociative adsorption of CO_2 taking place on the surface and desorb CO as product. However, molecular H_2 is activated on the surface due to high density of states at the E_F, which is confirmed with valence band spectrum. The activated hydrogen reacts with oxygen (due to CO_2 dissociation) on the surface to form water and regenerate the active sites on the surface. As a result, Mo_2C acts as a dual functional catalyst to activate both CO_2 and H_2.

5.3. Conclusion

In summary, we have synthesized Mo_2C by direct carburization of Mo precursor, and Mo_2C formation is characterized by relevant analytical methods. Our findings show the Mo_2C is an active, selective and stable catalyst for CO_2 hydrogenation to CO with H_2. NAPPES analysis on in-situ prepared Mo_2C foil shows carbide, oxycarbide as well as some oxide present on the surface under in-situ reaction conditions. It is to be underscored that Mo_2C is able to dissociate both C=O, H-H bonds and acts as dual functional catalyst. Oxycarbide formation observed under in-situ reaction conditions underscore its role as an intermediate and likely enhances the reaction rate; however, this aspect needs to be confirmed. Although some oxide is also observed, independent experiments with molybdenum oxide shows no activity. CO_2-TPD results show the surface has rich basic sites, which helps in the adsorption of Lewis acidic CO_2. Metallic character of carbide confirmed by valence band spectrum makes the activation of reactant molecules easier. Further, NAPPES studies reveal the dissociative adsorption of CO_2 on the surface of Mo_2C. Activity studies measured in a fixed bed reactor with powder Mo_2C catalyst show that Mo_2C catalyst with CO_2:H_2 ratio of 1:3 is highly active (58 % conversion) and selective towards carbon monoxide (62 %) at 723 K and at 1 atm pressure. In contrast to the energy intensive CO_2 conversion to methanol at very high pressures (100-400 bars), present work at atmospheric pressure is lucrative from the industrial point of view. In addition to that, Mo_2C can be synthesized from low cost, easily abundant elements than noble metals makes Mo_2C is a promising catalyst for hydrogenation reactions.

Synergy observed between basicity and redox nature of Mo_2C around 700 K correlates very well with high catalytic activity observed at the same temperature range. It is also to be highlighted that the work function of the catalyst under in-situ reaction condition changes by 0.5 eV and influencing the electronic nature of the catalyst surface.[47,48] In contrast to the semiconducting nature of majority of oxide-based catalysts, metallic nature of Mo_2C surface with high electron density at Fermi level is an interesting and important aspect. Work function changes under reaction condition insist the electron transfer and strong gas-solid interaction. This fully supports the nature of catalyst surface is, at least, significantly different from the fresh or activated catalyst surface. Much more in-situ studies are required to understand the catalyst under working conditions.

5.4. References

(1) M., D. A. D.; Berend, S.; R., L. J. *Angew. Chemie. Int. Ed.* **2010,** *49*, 6058-6082.

(2) Mikkelsen, M.; Jorgensen, M.; Krebs, F. C. *Energy. Environ. Sci.* **2010,** *3*, 43-81.

(3) Song, C. *Catal. Today* **2006,** *115*, 2-32.

(4) Kaiser, P.; Unde, R. B.; Kern, C.; Jess, A. *Chem. Ing. Tech.* **2013,** *85*, 489-499.

(5) Chen, C.-S.; Cheng, W.-H.; Lin, S.-S. *Appl. Catal. A* **2003,** *238*, 55-67.

(6) Eren, B.; Weatherup, R. S.; Liakakos, N.; Somorjai, G. A.; Salmeron, M. *J. Am. Chem. Soc.* **2016,** *138*, 8207-8211.

(7) van den Berg, R.; Prieto, G.; Korpershoek, G.; van der Wal, L. I.; van Bunningen, A. J.; Lægsgaard-Jørgensen, S.; de Jongh, P. E.; de Jong, K. P. *Nat. Commun.* **2016,** *7*, 13057.

(8) Sebastian, K.; Christian, C.; Georg, M. P.; Ib, C.; Jens, S. *Angew. Chem. Int. Ed.* **2014,** *53*, 5941-5945.

(9) Daza, Y. A.; Kuhn, J. N. *RSC Adv.* **2016,** *6*, 49675-49691.

(10) Li, Z.; Choi, J.-S.; Wang, H.; Lepore, A. W.; Connatser, R. M.; Lewis, S. A.; Meyer, H. M.; Santosa, D. M.; Zacher, A. H. *Energy Fuels* **2017,** *31*, 9585-9594.

(11) Velu, S.; Satoh, N.; Gopinath, C. S.; Suzuki, K. *Catal. Lett.* **2002,** *82*, 145-152.

(12) Maity, P.; Gopinath, C. S.; Bhaduri, S.; Lahiri, G. K. *Green Chemistry* **2009,** *11*, 554-561.

(13) Maity, N.; Rajamohanan, P. R.; Ganapathy, S.; Gopinath, C. S.; Bhaduri, S.; Lahiri, G. K. *J. Phys. Chem. C.* **2008,** *112*, 9428-9433.

(14) Gnanamani, M. K.; Hamdeh, H. H.; Shafer, W. D.; Hopps, S. D.; Davis, B. H. *Appl. Catal., A* **2018,** *564*, 243-249.

(15) Murugappan, K.; Anderson, E. M.; Teschner, D.; Jones, T. E.; Skorupska, K.; Román-Leshkov, Y. *Nat. Catal.* **2018**, 1, 960-967.

(16) Levy, R. B.; Boudart, M. *Science* **1973,** *181*, 547-549.

(17) Claridge, J. B.; York, A. P. E.; Brungs, A. J.; Marquez-Alvarez, C.; Sloan, J.; Tsang, S. C.; Green, M. L. H. *J. Catal.* **1998,** *180*, 85-100.

(18) Chen, Y.; Choi, S.; Thompson, L. T. *J. Catal.* **2016,** *343*, 147-156.

(19) Yao, S.; Zhang, X.; Zhou, W.; Gao, R.; Xu, W.; Ye, Y.; Lin, L.; Wen, X.; Liu, P.; Chen, B.; Crumlin, E.; Guo, J.; Zuo, Z.; Li, W.; Xie, J.; Lu, L.; Kiely, C. J.; Gu, L.; Shi, C.; Rodriguez, J. A.; Ma, D. *Science* **2017,** *357*, 389-393.

(20) Kunkel, C.; Vines, F.; Illas, F. *Energy Environ. Sci.* **2016,** *9*, 141-144.

(21) Velu, S.; Suzuki, K.; Vijayaraj, M.; Barman, S.; Gopinath, C. S. *Appl. Catal., B.* **2005,** *55*, 287-299..

(22) Velu, S.; Suzuki, K.; Gopinath, C. S. *J. Phys. Chem. B.* **2002,** *106*, 12737-12746.

(23) Subramanian, V.; Gnanakumar, E. S.; Jeong, D.-W.; Han, W.-B.; Gopinath, C. S.; Roh, H.-S. *Chem. Commun.* **2013,** *49*, 11257-11259.

(24) Mathew, T.; Sivaranjani, K.; Gnanakumar, E. S.; Yamada, Y.; Kobayashi, T.; Gopinath, C. S. *J. Mater. Chem.* **2012,** *22*, 13484-13493.

(25) Liu, P.; Rodriguez, J. A. *J. Chem. Phys.* **2004,** *120*, 5414-5423.

(26) Porosoff, M. D.; Kattel, S.; Li, W.; Liu, P.; Chen, J. G. *Chem. Commun.* **2015,** *51*, 6988-6991.

(27) Solymosi, F.; Oszkó, A.; Bánsági, T.; Tolmacsov, P. *J. Phys. Chem. B.* **2002,** *106*, 9613-9618.

(28) Posada-Perez, S.; Vines, F.; Ramirez, P. J.; Vidal, A. B.; Rodriguez, J. A.; Illas, F. *Phys. Chem. Chem. Phys.* **2014,** *16*, 14912-14921.

(29) D., P. M.; Xiaofang, Y.; Anibal, B. J.; G., C. J. *Angew. Chem. Int. Ed.* **2014,** *53*, 6705-6709.

(30) D., P. M.; W., B. J.; Xi, P.; Giannis, M.; D., W. H. *ChemSusChem* **2017,** *10*, 2408-2415.

(31) Lin, Z.; Wan, W.; Yao, S.; Chen, J. G. *Appl. Catal., B* **2018,** *233*, 160-166.

(32) Frauwallner, M.-L.; López-Linares, F.; Lara-Romero, J.; Scott, C. E.; Ali, V.; Hernández, E.; Pereira-Almao, P. *Appl. Catal., A* **2011,** *394*, 62-70.

(33) Pan, L. F.; Li, Y. H.; Yang, S.; Liu, P. F.; Yu, M. Q.; Yang, H. G. *Chem. Commun.* **2014,** *50*, 13135-13137.

(34) Reddy, K. P.; Mhamane, N. B.; Ghosalya, M. K.; Gopinath, C. S. *J. Phys. Chem. C.* **2018,** *122*, 23034-23044.

(35) Yeh, J. J.; Lindau, I. *Atomic Data and Nuclear Data Tables* **1985**, *32*, 1-155.

(36) Sugihara, M.; Ozawa, K.; Edamoto, K.; Otani, S. *Solid State Commun.* **2001,** *121*, 1-5.

(37) Wang, G.; Schaidle, J. A.; Katz, M. B.; Li, Y.; Pan, X.; Thompson, L. T. *J. Catal.* **2013,** *304*, 92-99.

(38) Malaibari, Z. O.; Croiset, E.; Amin, A.; Epling, W. *Appl. Catal., A* **2015,** *490*, 80-92.

(39) Gao, J.; Wang, Y.; Ping, Y.; Hu, D.; Xu, G.; Gu, F.; Su, F. *RSC Adv.* **2012,** *2*, 2358-2368.

(40) Wang, Z.-Q.; Zhang, Z.-B.; Zhang, M.-H. *Dalton Trans.* **2011,** *40*, 1098-1104..

(41) Deng, X.; Verdaguer, A.; Herranz, T.; Weis, C.; Bluhm, H.; Salmeron, M. *Langmuir* **2008,** *24*, 9474-9478..

(42) Jain, R.; Reddy, K. P.; Ghosalya, M. K.; Gopinath, C. S. *J. Phys. Chem. C.* **2017,** *121*, 20296-20305.

(43) Reddy, K. P.; Jain, R.; Ghosalya, M. K.; Gopinath, C. S. *J. Phys. Chem. C.* **2017,** *121*, 21472-21481.

(44) Axnanda, S.; Scheele, M.; Crumlin, E.; Mao, B.; Chang, R.; Rani, S.; Faiz, M.; Wang, S.; Alivisatos, A. P.; Liu, Z. *Nano Lett.* **2013**, *13*, 6176-6182.

(45) Ghosalya, M. K.; Jain, R.; Reddy, K. P.; Gopinath, C. S. *J. Phys. Chem. C.* **2018**, *122*, 4331.

(46) Ghosalya, M. K.; Reddy, K. P.; Jain, R.; Roy, K.; Gopinath, C. S. *J. Chem. Sci.* **2018**, *130*, 30.

(47) Gopinath, C. S.; Roy, K.; Nagarajan, S. *ChemCatChem* **2015**, *7*, 588.

(48) Burange, A. S.; Shukla, R.; Tyagi, A. K.; Gopinath, C. S. *ChemistrySelect* **2016**, *1*, 2673.

Chapter-6

Conclusions and future outlook

This chapter summarizes the present thesis work and possible future implications drawn based on the work. In the present thesis, an attempt has been made to explore the surfaces at near ambient conditions, in terms of pressure, and in a wide temperature regime with NAPPES technique to address the phenomenon called 'gas-solid' interaction, which is the fundamental aspect and very important in many research areas, like, catalysis, sensors, nanomaterials and electrochemistry. We tried to explain the surface work function changes, reaction mechanism and active state of the surfaces under ambient conditions and its utilization to unravel the events that occur under real working conditions. How the electronic structure evolves from one to another under oxidizing and/or reducing conditions has been explored in details, especially with valence band electronic structure.

To meet the rapidly growing population and global energy demands, how surface science can contribute and its essential role in the designing the active and selective catalyst were described in **Chapter 1.** In addition to that, an emphasis is given on how surfaces being controlled by many parameters, such as bonding strength of reactants, intermediates, co-adsorbates, impurities, surface morphology and products. Since industrial catalytic reactions occurs at ambient pressure or high pressure with complex catalyst surfaces and often active state of surface present exclusively under relevant conditions, it is essential to explore them under operando conditions. Hence, Information which obtained from conventional surface techniques under ideal conditions, we may not able to correlate surface science information to the real world catalysis data. To address this pressure and material gap, we gave an emphasis on existing in-situ surface sensitive techniques, and among those how NAPPES is important for studying catalysis under those conditions. A survey on literature related to NAPPES studies of gas-solid interaction and surface chemistry of CO_2 provided a significant output on the surface electronic structure and catalyst nature. It also helped in establishing the fundamental correlation between the catalyst performance and possible mechanism. The recent development in surface science and development of NAPPES gives us an excellent opportunity to study the real surfaces under real world catalysis conditions (or close to that)

and opens a new and vital chapter in the area of surface science by bridging the existing pressure gap and material gap.

Chapter 2 discusses about principle, instrumentation, near ambient pressure compatible design and performance aspect of NAPPES. In addition to that we gave an emphasis on gas phase vibrational features and its importance in finding the work function changes of any catalyst surfaces under oxidative, reductive and reaction conditions. Further we discussed about various metal surfaces (Co, Mo) sputtering conditions and synthesis of Mo_2C, CoO, Co_3O_4. Mo_2C powder catalyst was also prepared for evaluating in catalytic reactor at ambient pressure. Thorough characterisation of materials by various analytical techniques viz., XRD, SEM, TPR, TPD, EDX was made, and its working principles discussed briefly.

Chapter 3 discussed about the electronic structure evolution of Co to CoO, Co_3O_4 and their inter-convertibility. An attempt has been made to explore the electronic structure of Co foil during oxidation using both ultraviolet and x-ray photoelectron spectroscopy at near ambient pressures and at high temperatures. The oxidation states of Co in CoO and Co_3O_4 are very sensitive and these structures have very close thermodynamic stability. However, the electronic structure and reducibility/oxidizability of these oxides are the critical factors in determining the physical and chemical properties, such as magnetism, sensors, and catalysis. Basic understanding of the reduction of Co_3O_4, oxidation of CoO to spinel, and any intermediate species is likely to be helpful in the development of better catalyst with improved properties. Some of the important parameters, such as changes in E_F and ϕ, were determined under relevant conditions by NAPPES. Co metal gradually oxidizes to CoO at increasing pressure and between 350 and 400 K, and then to Co_3O_4 at 500 K. The oxide layers are restricted to the surface. From NAP-UPS, a clear difference in the VB features and the Fermi level of Co and its oxides was observed; this is well corroborated with XPS-VB results. Enhancement in the satellite peak is indicating the charge transfer nature of Co_3O_4. Co_3O_4 to CoO reduction and vice versa is fully possible within the evaluated conditions. A reversible changes in the work function were also observed from both O_2 and H_2 vibrational features in NAP-UPS. These findings underscore the relevance of NAPPES to surface dependent phenomena and it is very likely that future studies will exploit more on these lines.

Tuning the surface energetics, especially ϕ of the materials, is of great deal of interest for a wide range of surface and interface based devices and applications. Molybdenum trioxide (MoO_3) is an important oxide widely used in electronics to energy storage materials. It has

been observed that non-stoichiometric MoO_{3-x}, rather than stoichiometric MoO_3, was found to be better suited for the electronics to energy storage materials thus greatly improving the device performance; however, very less information is available on Mo^{5+} at interfaces and its characteristics. In the **chapter 4**, we have examined the $Mo/MoO_2/Mo_2O_5/MoO_3$ interfaces using NAPUPS and NAPXPS methods by controlled oxidation of the Mo foil at near-ambient pressures (up to 1 mbar) and temperatures (up to 900 K). A large increase in ϕ (2.4 eV) was observed from the Mo metal to MoO_3 with the valence band offset and NAPXPS O 1s spectra. A clear change in Mo^{5+} content was observed during the oxidation of MoO_2 to MoO_3 or the reduction of MoO_3 to MoO_2, near E_F. At the same time, a considerable increase in ϕ (0.6 eV) was observed with increasing extent of MoO_3 layer formation. By controlling the thickness, it is possible to tune the conductivity and can alter the ϕ of the α-MoO_3; information derived from the present study is likely to be used for a broad range of applications, such as optoelectronics. An important observation is the significant stability of the Mo^{5+} oxidation state found at the surfaces and interfaces of MoO_2 and MoO_3 under oxidizing and reduction conditions, respectively. Stability of Mo^{5+} makes it as a special species, since bulk Mo_2O_5 is not known. Progressive changes in ϕ observed from MoO_2 and MoO_3 (and the reverse) is attributed to the role of Mo^{5+} at the interfaces. Even small amounts of Mo^{5+} in the compounds would change the conductivity due to the Mo $4d^1$ electronic configuration; the $4d^1$ electronic state occurs close to the conduction band minimum and E_F, and lead to an additional/ impurity state, depending on the concentration. Mo^{5+} is expected to bring special features, such as redox, catalytic, and electrochemical functions, which is yet to be exploited fully. These studies may be extended by carefully tuning the surface thickness of MoO_2-$MoO_{2.5}$-MoO_3 along with catalytic reactions, which is likely to help in many direct applications. Essentially, stabilization aspects of Mo^{5+} at surface and interfaces would help to synthesize materials towards many applications in optoelectronics, redox chemistry.

Carbon dioxide is a greenhouse gas and needs to be converted into one of the useful feedstock, such as, carbon monoxide, methanol. However present existing catalysts with their complexity and cost limits the employability in the industries. In searching for an active, selective and low cost catalyst, transition metal carbides, especially molybdenum carbide has shown special attention due to similar electronic structure like Pt group metals. However, there is no consensus about the role of carbide/oxycarbide in the activity for CO_2 hydrogenation to CO and understanding the mechanism, catalyst surface structure under in-situ reaction conditions. In order to understand that, **chapter 5** demonstrates the reduction of

CO_2 with H_2 as reducing agent, via reverse water gas shift reaction (RWGS), by using a potential and low cost in-situ generated Mo_2C catalyst. Oxycarbide formation observed under in-situ reaction conditions underscore its role as an intermediate and likely enhances the reaction rate. CO_2-TPD results show the surface has rich basic sites, which helps in the adsorption of Lewis acidic CO_2. Metallic character of carbide confirmed by valence band spectrum makes the activation of reactant molecules easier. It is observed that Mo_2C is able to dissociate both C=O, H-H bonds and acts as dual functional catalyst. In addition that activity studies measured in a fixed bed reactor with powder Mo_2C catalyst show that Mo_2C catalyst with CO_2:H_2 ratio of 1:3 is highly active (58 % conversion) and selective towards carbon monoxide (62 %) at 723 K and at 1 atm pressure. In contrast to the energy intensive CO_2 conversion to methanol at very high pressures (100-400 bars), present work at atmospheric pressure on low cost Mo_2C is lucrative from the industrial point of view. Synergy observed between basicity and redox nature of Mo_2C around 700 K correlates very well with high catalytic activity observed at the same temperature range. It is also to be highlighted that the work function of the catalyst under in-situ reaction condition changes by 0.5 eV and it insist the electron transfer and strong gas-solid interaction. In contrast to the semiconducting nature of majority of oxide-based catalysts, metallic nature of Mo_2C surface with high electron density at Fermi level is an interesting and important aspect. More studies viz,. controlled synthesis of different metal doped Mo_2C and different in-situ technique studies are required to improve the product selectivity and understand the catalyst reaction mechanism.

Above discussion underscores that NAPPES enable to directly address basic concepts of heterogeneous catalysis such as gas-solid interaction, work function changes. Electronic structure evolution of solid surfaces as a function of reaction conditions is possible. This would help to identify the “real active phase” of catalyst under working conditions. This integrated approach has given the field of catalysis a new impetus at a time when energy efficiency and green chemistry are major societal goals. In this direction, with further advance developments in the pipeline, it is possible to understand the molecular level mechanism with many fine details, which is expected to help better and active materials for many applications. Many demanding reactions, such as nitrogen/methane activation could be explored in detail.